

Università degli Studi di Torino  
FACOLTÀ DI SCIENZE MATEMATICHE FISICHE E NATURALI  
Corso di Laurea Magistrale in Fisica

Tesi di Laurea Magistrale in Fisica



# Muon momentum scale measurements in the CMS experiment

**Relatore**

Prof. Ernesto Migliore

**Controrelatore**

Prof. Stefano Giovanni Spataro

**Candidato**

Simone Pagliari

Anno accademico 2012-2013

*Men and women are not content to comfort themselves  
with tales of gods and giants, or to confine their  
thoughts to the daily affairs of life ...*

# Contents

<b>Introduction</b>	<b>iv</b>
<b>Introduzione</b>	<b>1</b>
<b>1 CMS and LHC</b>	<b>1</b>
1.1 The Large Hadron Collider . . . . .	1
1.2 The Compact Muon Solenoid . . . . .	6
1.2.1 Coordinate reference frame . . . . .	8
1.2.2 The inner tracking system . . . . .	8
1.2.3 The Electromagnetic CALorimeter . . . . .	11
1.2.4 The Hadronic CALorimeter . . . . .	12
1.2.5 The superconducting solenoid . . . . .	12
1.2.6 The muon system . . . . .	13
1.2.7 The trigger system . . . . .	15
<b>2 Muon Recostruction in CMS</b>	<b>17</b>
2.1 Muons track reconstruction . . . . .	18
2.2 Alignment . . . . .	21
2.3 Weak modes . . . . .	26
2.4 Resonance reconstruction in the tracker . . . . .	28
<b>3 Muon Calibration with the MuSclFit Algorithm</b>	<b>34</b>
3.1 The MuSclFit likelihood . . . . .	36
3.2 Building of the signal probability . . . . .	37
3.2.1 The signal function . . . . .	37
3.2.2 The parametrization of the momentum scale correction	40
3.2.3 The parametrization of the momentum resolution . .	44
3.3 Building of background probability . . . . .	48
3.3.1 Parametrization of the background . . . . .	49
3.4 Fit strategy . . . . .	52
<b>4 Results of the Muon Calibration</b>	<b>53</b>
4.1 Local effects of the corrections . . . . .	57
4.1.1 Calibration for samples at $\sqrt{s} = 7$ TeV . . . . .	57

---

4.1.2	Calibration for samples at $\sqrt{s} = 8$ TeV . . . . .	63
4.2	Extra smearing on simulated muons . . . . .	67
4.2.1	Smearing on the sample at $\sqrt{s} = 7$ TeV . . . . .	68
4.2.2	Smearing the sample at $\sqrt{s} = 8$ TeV . . . . .	68
4.3	Global effects of the corrections . . . . .	70
4.3.1	Results at $\sqrt{s} = 7$ TeV . . . . .	70
4.3.2	Results at $\sqrt{s} = 8$ TeV . . . . .	72
4.4	Weak modes in the barrel . . . . .	76
4.5	Resolution on the curvature of the muons . . . . .	81
4.6	Detailed validation of the corrections . . . . .	83
	<b>Conclusions</b>	<b>89</b>
	<b>Appendix A Fit strategy</b>	<b>90</b>
	<b>Appendix B Additional lineshapes</b>	<b>92</b>
B.1	Building of the signal function of $Z$ in kinematic intervals of the muons . . . . .	92
B.2	Building of the signal function for $J/\Psi$ and $Y(1S)$ . . . . .	96
	<b>Bibliography</b>	<b>100</b>
	<b>Acknowledgements</b>	<b>102</b>

# Introduction

The Standard Model of Particle Physics is a relativistic quantum field theory that describes the particles observed in nature and their interactions, except for gravitation and, up to now, is one of the best tested physics theories of modern Physics. The main motivation to build the Large Hadron Collider (LHC) is to investigate the hidden sectors of the Standard Model of particle physics. On 14 March 2013 the existence of the Higgs boson in the mass region of about  $125 - 126 \text{ GeV}/c^2$  has been confirmed by the ATLAS and the CMS collaborations. However, it remains an open question, whether it is the Higgs boson of the Standard Model of particle physics, or possibly the lightest of several bosons predicted in some theories that go beyond the Standard Model. These sectors of physics are available only at a high energy scale and therefore the LHC was designed to provide proton-proton collisions at a center of mass energy of 14 TeV. The collider started operating at  $\sqrt{s} = 7 \text{ TeV}$  in 2011 and  $\sqrt{s} = 8 \text{ TeV}$  in 2012. Before its stop in December 2012 the integrated luminosity reached in CMS was about  $23 \text{ fb}^{-1}$ . The high luminosity and the high energy of the colliding protons lead to challenging demands to the detector, such as the precise measurement of the momentum and energy of the particles. The work presented in this thesis has been carried out within the Torino CMS group. It is devoted to the study of a method to calibrate the momentum scale of high energy muons measured in the CMS experiment. In Chapter 1 the LHC accelerator is introduced and a description of the characteristics of the CMS experiment is presented, such as the experimental setup and the properties of the detectors. Chapter 2 contains an overview on the methods used to reconstruct a track of a particle in CMS, an introduction on the alignment algorithms and their goals, and a brief description of the problematics encountered in reconstructing the resonance of a massive boson in the inner part of the detector: the Tracker. In Chapter 3 an algorithm used to calibrate the momentum of the muons, the MuSclFit algorithm, is presented, and the results of the application of such algorithm in the reconstruction of the Z boson are studied in Chapter 4. In this work will be used the natural units, i.e.  $\hbar = c = 1$ .

# Introduzione

Il Modello Standard della fisica delle particelle è una teoria di campo quantistica e relativistica che descrive le particelle osservate in natura e le loro interazioni, fatta eccezione per la gravità e, attualmente, è una delle teorie della fisica moderna più sottoposte ad indagine sperimentale. Il Large Hadron Collider (LHC) è stato costruito principalmente per indagare il Modello Standard e le questioni rimaste aperte legate ad esso. Il 14 marzo 2013 l'esistenza del bosone di Higgs nella una regione di massa di circa  $125 - 126 \text{ GeV}/c^2$  è stata confermata dagli esperimenti CMS e ATLAS. Tuttavia rimane da capire se il bosone di Higgs osservato è quello del Modello Standard oppure rappresenta l'elemento più leggero di una serie di bosoni predetti da alcune teorie che vanno oltre il Modello Standard. Questi settori della fisica possono essere esplorati solo nell'ambito di esperimenti ad alta energia. Di conseguenza LHC fu progettato per produrre collisioni protone-protone con energia nel centro di massa di 14 TeV. Il collisore è partito operando a  $\sqrt{s} = 7 \text{ TeV}$  nel 2011 ed è stato portato ad  $\sqrt{s} = 8 \text{ TeV}$  nel 2012. Prima del suo arresto in vista di un futuro upgrade nel dicembre 2012 la luminosità integrata raggiunta in CMS è stata di circa  $23 \text{ fb}^{-1}$ . L'alta luminosità e l'alta energia delle collisioni tra protoni portano a richieste molto esigenti per un rivelatore, come la misurazione precisa dell'impulso e dell'energia delle particelle.

Il lavoro presentato in questa tesi è stato effettuato nell'ambito del gruppo CMS di Torino. E' mirato allo studio di un metodo per calibrare la scala dell'impulso dei muoni ad alta energia misurati nell'esperimento CMS.

Nel Capitolo 1 viene introdotto l'acceleratore LHC e descritto brevemente l'esperimento CMS. Il capitolo 2 contiene una introduzione sui metodi usati per ricostruire la traccia di una particella in CMS, una introduzione agli algoritmi di allineamento, e una breve illustrazione delle problematiche incontrate nel ricostruire la risonanza di un bosone massivo nella parte interna del rivelatore: il Tracker. Nel capitolo 3 è presentato l'algoritmo MuSclFit, un algoritmo usato per calibrare il momento dei muoni, e i risultati dell'applicazione di questo algoritmo nella ricostruzione del bosone Z sono studiati nel capitolo 4.

# Chapter 1

## CMS and LHC

### 1.1 The Large Hadron Collider

The Large Hadron Collider (LHC) is the most powerful particle accelerator ever built. It consists of a 27 km ring of superconducting magnets with a number of accelerating structures to boost the energy of the particles along the way. The ring realized by the European Organization for Nuclear Research (CERN), and is installed on the borderline between France and Switzerland, 50-170 m underground. It is the latest addition of the CERN complex of accelerators (see Figure 1.1), each accelerator boosts the speed of a beam of particles, before injecting it into the next one in the sequence. The LHC is designed to collide protons, as well as lead ions, at an energy and rate never reached before, in order to address some of the most fundamental questions of physics. The main design characteristics of the machine are listed in Table 1.1. The beams travel in opposite directions in separate cavities kept at ultrahigh vacuum, the *beam pipes*. The bending power needed to keep the beam circulating is the limiting factor to the achievable centre of mass energy. At the design energy of 14 TeV in order to keep the proton beams in their orbit is necessary a magnetic field of more than 8 T. This intensity of magnetic field is only achievable with the use of superconducting electromagnets. The electromagnets are built from coils of special electric cable that operates in a superconducting state, efficiently conducting electricity without resistance or loss of energy. This requires chilling the magnets to  $-271.3^{\circ}$  C with the use of liquid helium. The boosts are given by 400 MHz superconducting radio-frequency cavities with a voltage ranging between 8 and 16 MV. Despite the design center of mass energy of the proton proton collisions was 14 TeV, in the first run period in 2010 were reached only 3.5 TeV energy per beam, corresponding to a centre of mass energy of 7 TeV. Only in 2012 the energy in the center of mass was raised to 8 TeV. The beams collide in four points along the ring, in correspondance of four experiments: CMS, ALICE, ATLAS and LHCb.

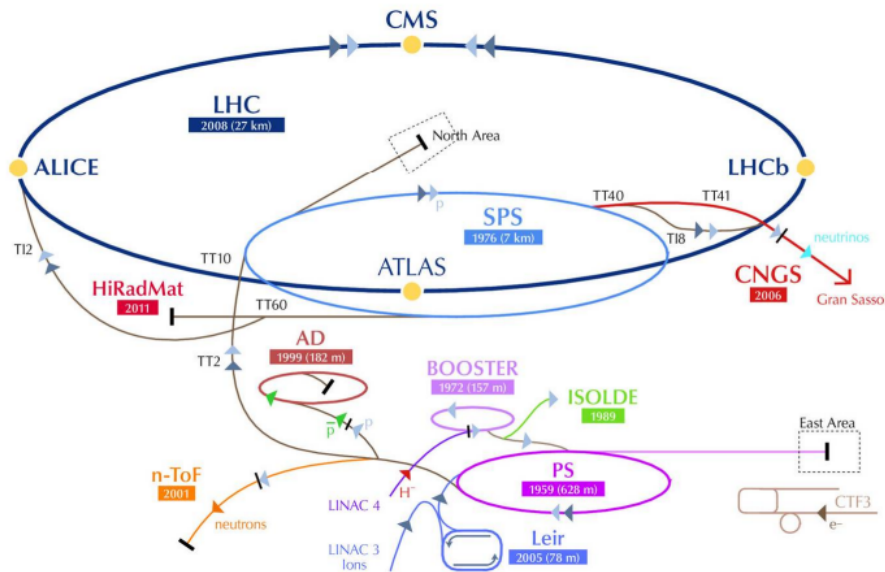


Figure 1.1: CERN complex of accelerators.

Each one is specialised to study a particular area of particle physics.

- CMS (Compact Muon Solenoid) is a multi-purpose designed to investigate a wide range of physics phenomena. Currently the main physics program of CMS includes the measurement of the properties of the Higgs boson, the search for supersymmetric and dark matter particles, the study of possible mechanism that generate the matter-antimatter imbalance observed in the universe, and the search for the existence of extra dimensions predicted by many theories. It has a cylindrical geometry around the beam pipe. The charged particles are bended by a superconducting solenoid that provide a quite uniform magnetic field of 3.8 T in the inner region.
- ATLAS (A large Toroidal Lhc ApparatuS) as well as CMS is a multi-purpose detector. It is built with a cylindrical geometry around the beam pipe. Here the particles are bended by two magnetic field, one generated by a small superconducting solenoid in the inner part of the detector, and the other generated by a three sets of toroids placed in the outer part of the detector.
- LHCb (Large Hadron Collider beauty experiment) is designed to study the decays of B mesons, in order to investigate the CP violation. LHCb physicists measure important CP violation properties looking for new subatomic mechanisms for the matter-antimatter imbalance.



LHC design characteristics		
Parameter	pp	Pb-Pb
Circumference [km]		26.659
Beam radius at interaction point [ $\mu\text{m}$ ]		15
Dipole peak field [T]		8.3
Centre-of-mass energy [TeV]	14	1148
Instantaneous luminosity [ $\text{cm}^{-2} \text{s}^{-1}$ ]	$10^{34}$	$2 \cdot 10^{27}$
Luminosity lifetime [h]	10	4.2
Number of particles per bunch	$1.1 \cdot 10^{11}$	$\approx 8 \cdot 10^7$
Number of bunches	2808	608
Bunch length	53	75
Time between collisions [ns]	24.95	$124.75 \cdot 10^3$
Bunch crossing rate [MHz]	40.08	0.008

**Table 1.1:** Large Hadron Collider design parameters for  $p$ - $p$  and  $Pb$ - $Pb$ .

- ALICE (A Large Ion Collider Experiment) is a heavy-ion dedicated detector, it is designed to study the ultra-high energy regime of ion-ion collisions. It has been conceived to study the physics of strongly interacting matter at extreme energy densities, where the formation of the quark-gluon plasma is expected. The existence of such a phase and its properties are key issues in QCD for the understanding of confinement and of chiral-symmetry restoration.

Furthermore two other experiments along the ring are active, they are different from the others because in correspondence of these experiments is not organized a collision between the beams circulating in the LHC.

- TOTEM (TOTal Elastic and diffractive cross section Measurement), a detector that consists in eight vacuum chambers containing GEM detectors and cathode strip chambers, placed in pairs in four different points near the CMS detector. It monitors accurately the LHC luminosity, by detecting particles very close to the beam line.
- LHCf (where "f" stands for forward) is an experiment that consists in two identical detectors placed on both sides of the ATLAS experiment, it uses forward particles created inside the LHC as a source to simulate ultra-high energy cosmic rays in laboratory conditions.

Two of the main experiments, ATLAS and CMS, are designed for a high luminosity regime, in order to catch the rare events of their physics programs. Therefore the rate of the collisions is, as well as the energy of the

centre of mass of the collisions, an important parameter for LHC. The luminosity  $\mathcal{L}$  of a collider machine is defined by the ratio of the rate  $R$  of a process and its cross section  $\sigma$ :

$$\mathcal{L} = \frac{R}{\sigma}$$

$\mathcal{L}$  can be also expressed as:

$$\mathcal{L} = \frac{fN_1N_2n_b}{4\sigma_x\sigma_y} F \quad (1.1)$$

where  $n_b$  the number proton bunches per beam,  $f$  is the revolution frequency,  $F$  is the geometric luminosity reduction factor ( $\approx 0.8 - 0.9$ ) due to the crossing angle between the two beams at the interaction point,  $N_1$  and  $N_2$  the number of protons in the bunches,  $\sigma_x$  and  $\sigma_y$  are the rms transverse beam sizes in the directions perpendicular to the beam. The instantaneous luminosity obtained in the 2011 and 2012 runs are substantially below the design values. Every experiment keep track of both *delivered* and *recorded* luminosity. Consider as example the case of CMS: the delivered luminosity refers to the luminosity delivered to the CMS by the LHC. The recorded luminosity includes only the luminosity actually logged by CMS. Ideally, the amount of luminosity recorded should be the same as the amount delivered, but in some cases the CMS detector is unable to take data, either because its data acquisition chain is busy or because one or more of its detector subsystems is temporarily unavailable. The integrated luminosity delivered to CMS by LHC during runs in 2010 ( $\sqrt{s} = 7$  TeV), 2011 ( $\sqrt{s} = 7$  TeV) and 2012 ( $\sqrt{s} = 8$  TeV) are respectively  $44.2 \text{ pb}^{-1}$ ,  $6.1 \text{ fb}^{-1}$ ,  $23.3 \text{ fb}^{-1}$ , see Figure 1.2. A comparison between the luminosity delivered to and recorded by CMS in 2012 is shown in Figure 1.3, the difference between the recorded and delivered integrated luminosity is about 7%.

Currently the machine is in shut down for at least two years to technically prepare for running at  $\sqrt{s} = 14$  TeV. During this time the various detectors installed at LHC may upgrade their subdetectors systems to improve their performance in view of the higher-energy and higher-luminosity runs.

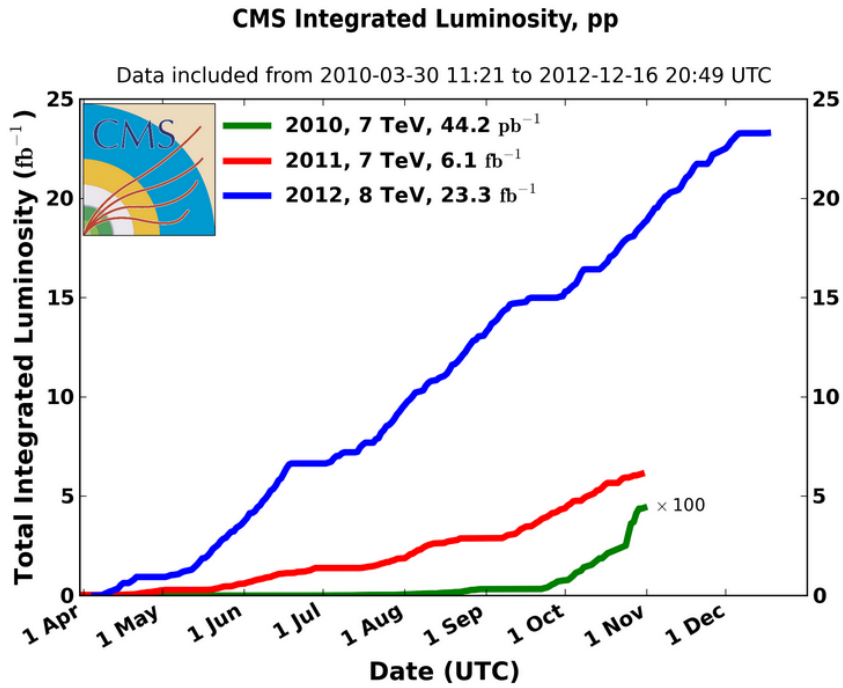


Figure 1.2: Luminosity delivered by LHC to CMS in 2010, 2011 and 2012 runs.

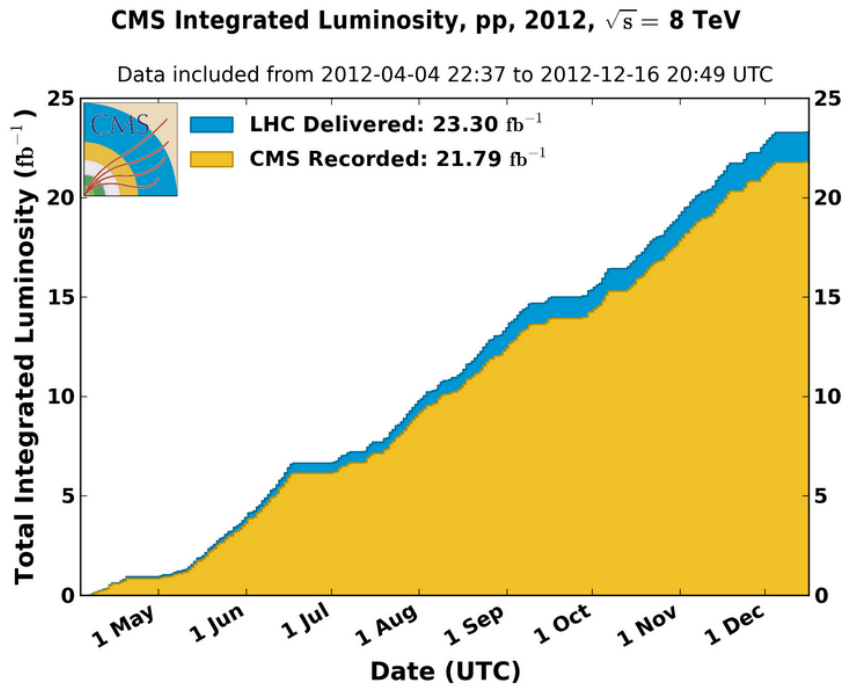


Figure 1.3: Luminosity delivered to and recorded by CMS in 2012 runs.

## 1.2 The Compact Muon Solenoid



**Figure 1.4:** *View of the CMS experiment during its assembling.*

The CMS (Compact Muon Solenoid) is a multi-purpose detector, currently the goals of its physics program are: the study of the Higgs boson, the precise measurements of the Standard Model properties, the search for physics Beyond the Standard Model (BSM), for example particles predicted by supersymmetric theoretical models, extra dimensions and dark-matter candidates. Considering the LHC center-of-mass energy, the discovery potential of CMS is very high since it will be possible to detect new particles up to masses of 3-5 TeV. To achieve the goals of its physics program the CMS Collaboration designed a very compact detector characterized by a strong magnetic field generated by a 3.8 T superconducting solenoid, an extremely precise tracking system for the measurements of the momentum of the tracks both in the inner part (the Tracker) and in the outer part (the muon system) of the detector, an excellent electromagnetic calorimeter, and a hermetic hadronic calorimeter system capable of delivering good performance in missing transverse energy reconstruction. A schematization of the detector is shown in Figure 1.5, its overall length is 21.6 m, its diameter 14.6 m and its total weight about 12500 tons. In what follows is presented a general description of CMS and its parts.

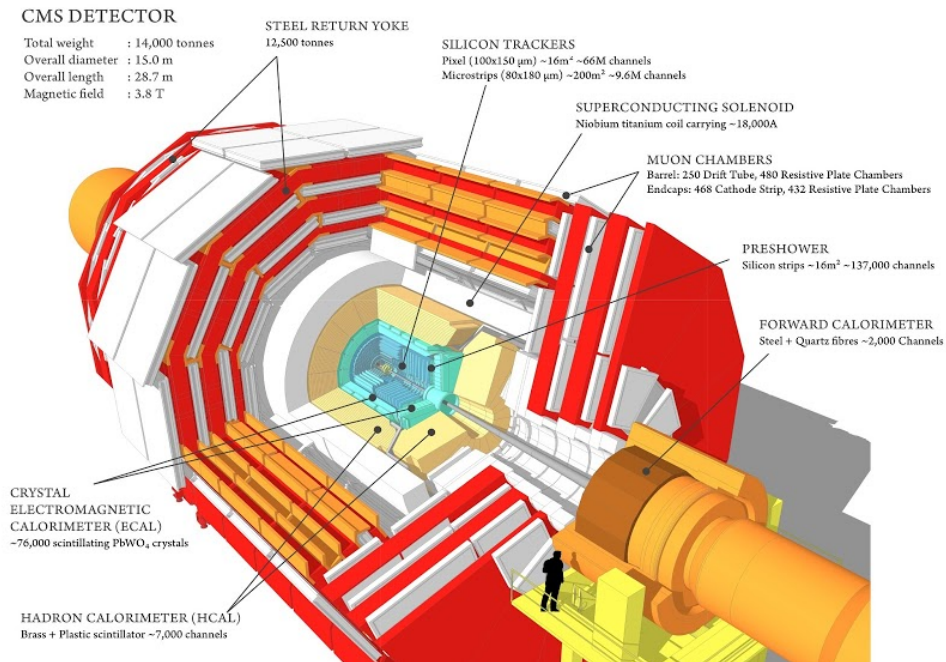


**Figure 1.5:** Schematization of the CMS experiment and its parts.

### 1.2.1 Coordinate reference frame

The global coordinate system in CMS is defined as follows. The origin is centered at the nominal collision point inside the experiment. The  $z$ -axis points along the beam axis, the  $y$ -axis points upwards and the  $x$ -axis points inwards to the center of the collider ring. Figure 1.6 shows the situation. The azimuthal angle  $\varphi$  is measured from the  $x$ -axis in the  $x$ - $y$

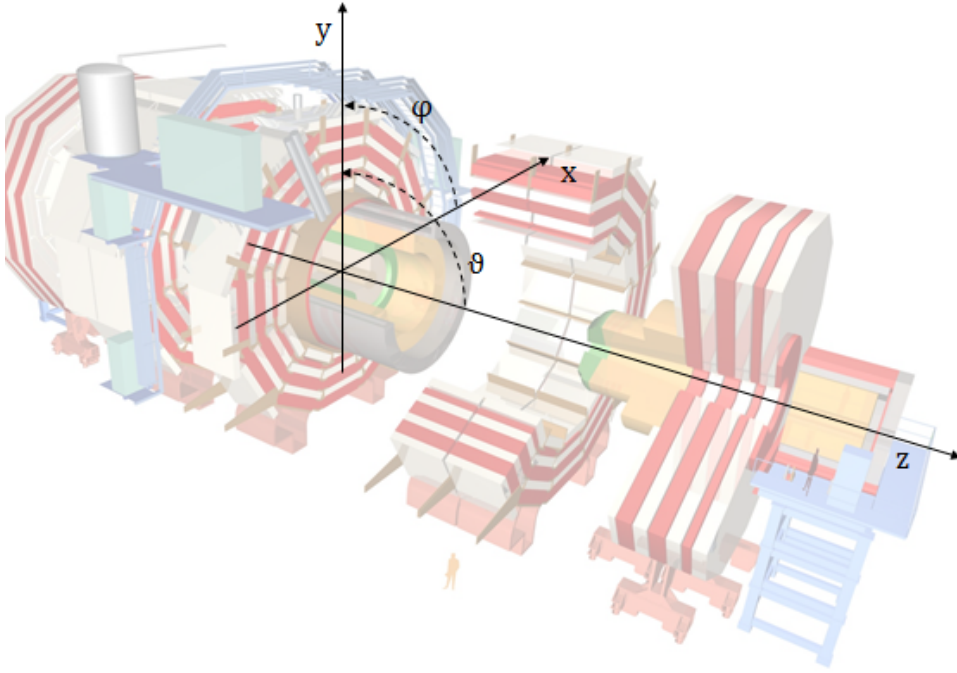


**Figure 1.6:** Global cartesian coordinate system as defined in CMS.

plane and the polar angle  $\theta$  is measured from the  $z$ -axis. Here, if  $p_x$  and  $p_y$  are the components of the momentum of a particle along the  $x$ -axis and  $y$ -axis, the quantity  $p_T \equiv \sqrt{p_x^2 + p_y^2}$  is called *transverse momentum*. Instead of  $\theta$  it is often used the geometrical variable called *pseudorapidity*, defined as:

$$\eta \equiv -\ln \left[ \tan \left( \frac{\theta}{2} \right) \right]$$

### 1.2.2 The inner tracking system

The part of the detector closest to the collision point is the Tracker. It consists in a cylinder of 5.4 m of length and 2.4 m of diameter that contains several layers of silicon sensors and is used to reconstruct charged particle tracks and primary and secondary interaction vertices. Inside the tracker is present a magnetic field of about 3.8 T that bends charged particles

allowing the measurement of their momentum. The tracker extends in the region  $\eta < 2.5$ ,  $r < 120$  cm,  $|z| < 270$  cm and is completely based on semiconductor detectors made of silicon and covering a surface of about 200 m<sup>2</sup>. The tracker is designed to fulfill few basic properties:

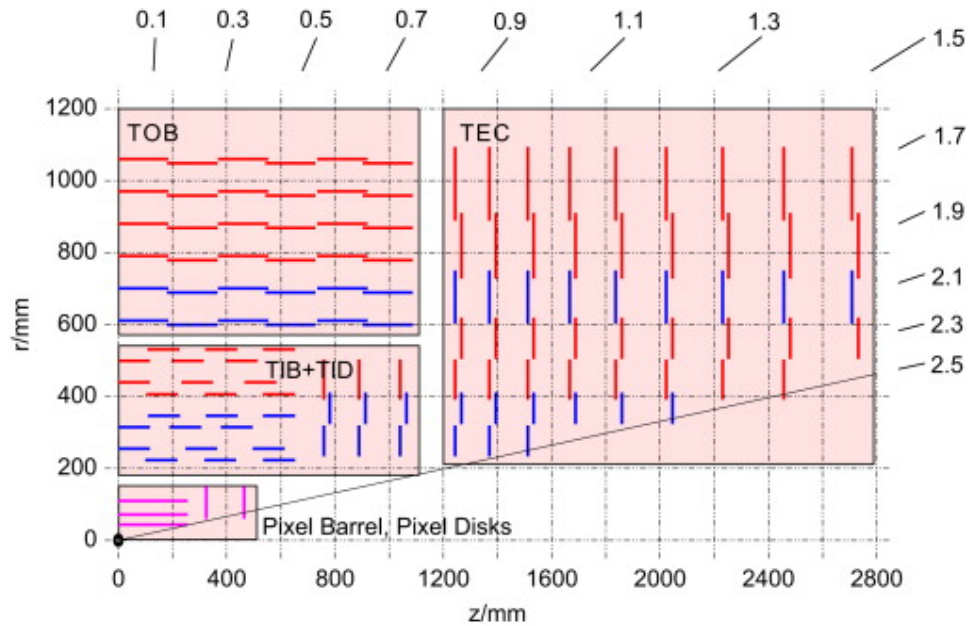


**Figure 1.7:** Longitudinal section of a quarter of the inner tracking system.

- promptness in the response: mandatory, since collision events occur every 25 ns and in each of them up to tens of tracks are produced.
- low cell occupancy: obtained by high granularity detectors, mainly those closest to the interaction point because they have to cope with higher particle fluxes, and a fast primary charge collection.
- large hit redundancy: allows many measured points per track in order to guarantee a high tracking efficiency and a low rate of fake tracks<sup>i</sup> (1% or less). The CMS Tracker geometry has been designed so as to provide typically 13 distinct high resolution measurement planes for stiff tracks up to  $|\eta| \approx 2.0$ , gradually falling to a minimum of 8 planes at  $\eta \approx 2.5$ .

In the central rapidity region the detectors are arranged in a barrel geometry, while at higher values of rapidity they are deployed as disks, organised into end-caps (see Figure 1.7). Two types of detectors are used in the

<sup>i</sup>reconstructed tracks not corresponding to any real track.

Tracker: silicon pixel detectors and silicon strip detectors. They identify two regions of the Tracker, the pixel Tracker and the strip Tracker.

- **The pixel Tracker:** is the part of the detector closest to the interaction vertex. It consists of three 53.3 cm long barrel layers (BPIX) placed at radii of 4, 7 and 11 cm, and two endcap disks (FPIX) on each side of the barrel section extending from 6 to 15 cm in radius, and placed at  $z = \pm 35.5$  cm and  $z = \pm 48.5$  cm (see Figure 1.8). In order to achieve

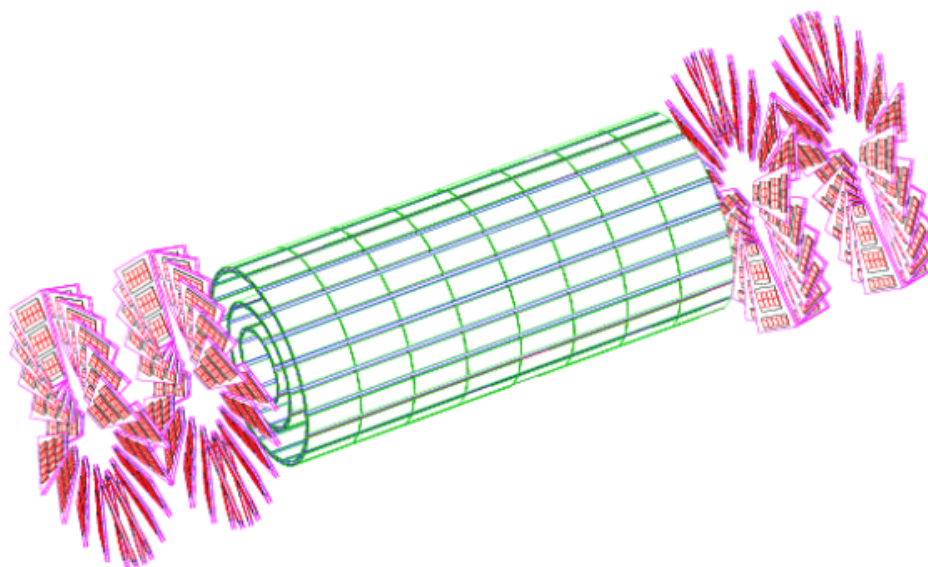


**Figure 1.8:** 3D schematization of the pixel Tracker.

a fine 3D vertex reconstruction, it is composed of approximately 66 millions pixel cells, with size  $100 \times 150 \mu\text{m}^2$ , that allow a precise measurement of the hits both along  $r\phi$  and  $z$  directions. The sensor are read-out analogically and a spatial resolution of  $\sim 10 \mu\text{m}$  for the  $r\phi$  coordinate and of  $\sim 20 \mu\text{m}$  for the  $z$  is achieved interpolating the charge induced in nearby pixels. The short distance of the pixel detectors from the interaction point imposes special requirements on radiation hardness and will probably require the substitution of the pixel detector during the lifetime of the experiment.

- **The strip Tracker:** it is placed in the outer part of the Tracker, the basic difference with the pixel Tracker is that here is used a silicon strip technology for the detectors. Silicon strip sensors provide information on the position of the hit only along one direction. In the global reference frame this direction is along  $r\phi$ . The strip Tracker can be divided into six subdetectors. In the barrel region the inner part of the strip Tracker is the Tracker Inner Barrel (TIB). It consists



in four layers from  $r = 20$  cm to  $r = 60$  cm. The first two layers are made with double sided modules, composed by two detectors mounted back to back. Their strips are tilted by 100 mrad in order to provide a measurement in the  $z$  coordinate too. The single point resolution of the TIB modules is from 23 to 34  $\mu\text{m}$  (varying with  $r$ ) along  $r\phi$  and, only for the double sided modules, 230  $\mu\text{m}$  along  $z$ ; In the outer part of the barrel region there are six layers of the Tracker Outer Barrel (TOB), which cover a range  $60 < r < 120$  cm. In this case the resolution on the single hit along  $r\phi$  vary from 32 to 54  $\mu\text{m}$ . As in the TIB also the first two layers of the TOB provide a measurement along  $z$  with the use of double sided modules, the single point resolution along  $z$  is 530  $\mu\text{m}$ . In the endcaps both for the forward and the backward region of the tracker there are three layers of Tracker Inner Disks (TID) and nine layers of Tracker End Cap (TEC), covering an interval in pseudorapidity of  $1.6 < |\eta| < 2.4$ .

### 1.2.3 The Electromagnetic CALorimeter

The Electromagnetic Calorimeter (ECAL) has the task to measure the energy of the photons and electrons coming from the collision. Electrons and photons interact with the material of the calorimeter until they lose all their energy in a shower of particles. The energy of the shower is measured by the calorimeter with high precision. ECAL is composed of 75848 finely segmented lead tungstate ( $\text{PbWO}_4$ ) crystals positioned at  $r = 1.29$  m. Lead tungstate is a fast, radiation-hard scintillator characterized by a small Molière radius (21.9 mm) and a short radiation length (8.9 mm), that allows a good shower containment in the limited space available for the detector. These crystals are also characterized by a very short scintillation decay time which allows to be used at a crossing rate of 40 MHz. The calorimeter is divided into two parts, one in the barrel region that covers the rapidity region  $|\eta| < 1.48$ , and the other in the endcap region, covering a rapidity region up to  $|\eta| = 3$ . A pre-shower detector is installed in front of the endcaps, it is used to distinguish between showers started from neutral pions and photons or charged pions and electrons. Silicon Avalanche Photodiodes (APDs) and Vacuum Phototriodes (VPTs) are used to collect the scintillation light in the barrel and in the endcaps respectively. A schematic view of the ECAL is shown in Figure ??

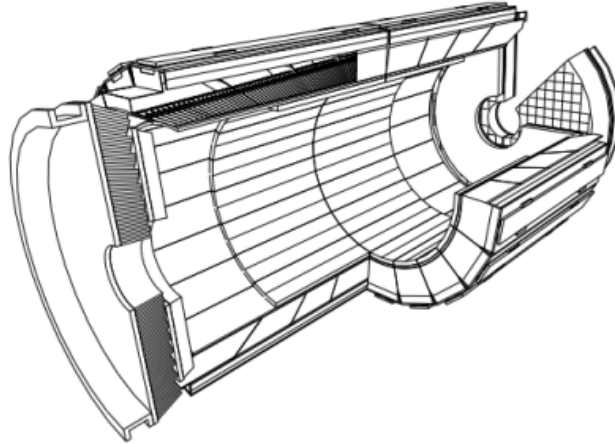


**Figure 1.9:** Schematic 3D view of the ECAL.

#### 1.2.4 The Hadronic CALorimeter

The goal of the hadron calorimeter (HCAL) is to measure the direction and energy of jets, the total transverse energy and the imbalance in the transverse energy, in order to detect the presence of high energy neutrinos. High hermeticity is required for this purpose, hence the HCAL is divided into four regions which provide a full angular coverage up to  $|\eta| = 5$ . The barrel hadronic calorimeter (HB) surrounds the electromagnetic calorimeter and covers the pseudorapidity region  $|\eta| < 1.3$ , while two endcap hadron calorimeters (HE) cover up to  $|\eta| = 3.0$ . They are sampling calorimeters, whose active elements are plastic scintillators interleaved with brass absorber plates and read out by wavelength-shifting fibres. Moreover two forward hadronic calorimeters (HF) cover the region up to  $|\eta| = 5.0$ , they are positioned at a distance of about 11 m from the interaction point and are needed for identification and reconstruction of the very forward jets. Both barrel and endcap are read-out in towers with a size of  $\Delta\eta \times \Delta\phi = 0.087 \times 0.087$ . In the barrel, a full shower containment is not possible within the magnet volume, and an additional layer of scintillators is placed outside the magnet, the hadron outer (HO). The projective depth in terms of nuclear absorption length goes from  $5.15\lambda_0$  at  $\eta = 0$  to  $9.1\lambda_0$  at  $|\eta| = 1.3$ , and is  $10.5\lambda_0$  in the endcap.

#### 1.2.5 The superconducting solenoid

The CMS magnet is the central device around which the experiment is built, with his 14 m of diameter and 12000 tonnes of weight is the largest superconducting magnet ever built. The intensity of its field of about 3.8 T is reachable only with a superconducting technology, therefore the

magnet is constantly kept at  $-268.5^\circ$  by liquid helium flows. A strong magnetic field combined with the high-precision position measurements in the tracker and muon detectors allows the measurement of the momenta of extremely high-energy particles. An high precision in the knowledge of the intensity of the magnetic field in the whole detector is mandatory for any physics analyses. Two methods for mapping the magnetic field are a fieldmapper made of sensors, and the cosmic rays. Measurements of the magnetic field inside the solenoid is done with precision of 0.07%. While outside the solenoid the precision decreases to 3% in the steel of the three central barrel wheels, and to about 8% in the steel of the two outermost barrel wheels. Figure 1.10 shows a map of the intensity of the magnetic field in a longitudinal section of CMS.

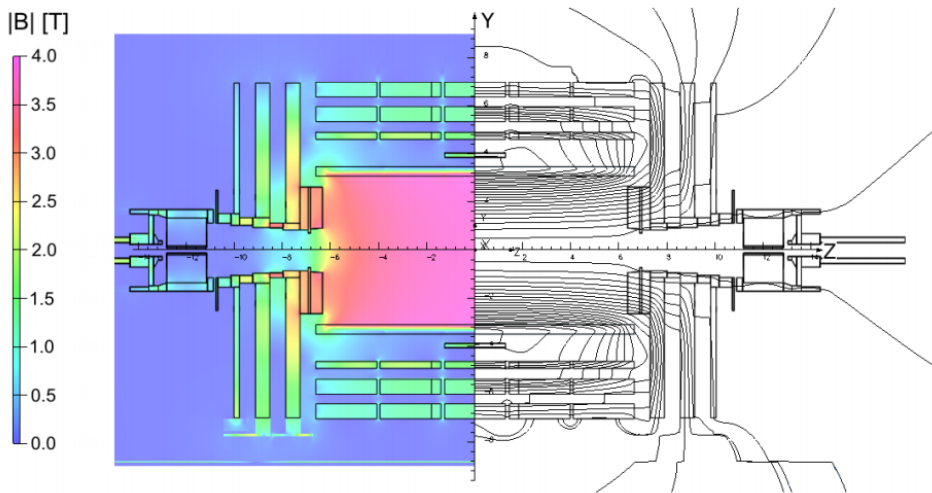


**Figure 1.10:** Value of  $|B|$  (left) and field lines (right) predicted on a longitudinal section of the CMS detector, for the underground model at a central magnetic flux density of 3.8 T. Each field line represents a magnetic flux increment of 6 Wb.

### 1.2.6 The muon system

The muon spectrometer has the purpose to provide a robust trigger and an accurate measurement of the momentum and charge of the muons, the only charged particles which are not absorbed by the calorimeters. The minimum value of the muon transverse momentum required to reach the system is  $\sim 5$  GeV. The muon spectrometer covers the pseudorapidity region  $|\eta| < 2.4$  and is divided into barrel and endcaps, both regions are organized in four measuring stations, embedded in the iron of the magnet return yoke, and use different technologies for the detectors. A schematization of the positions of the detectors in the muon system is

shown in Figure 1.11.

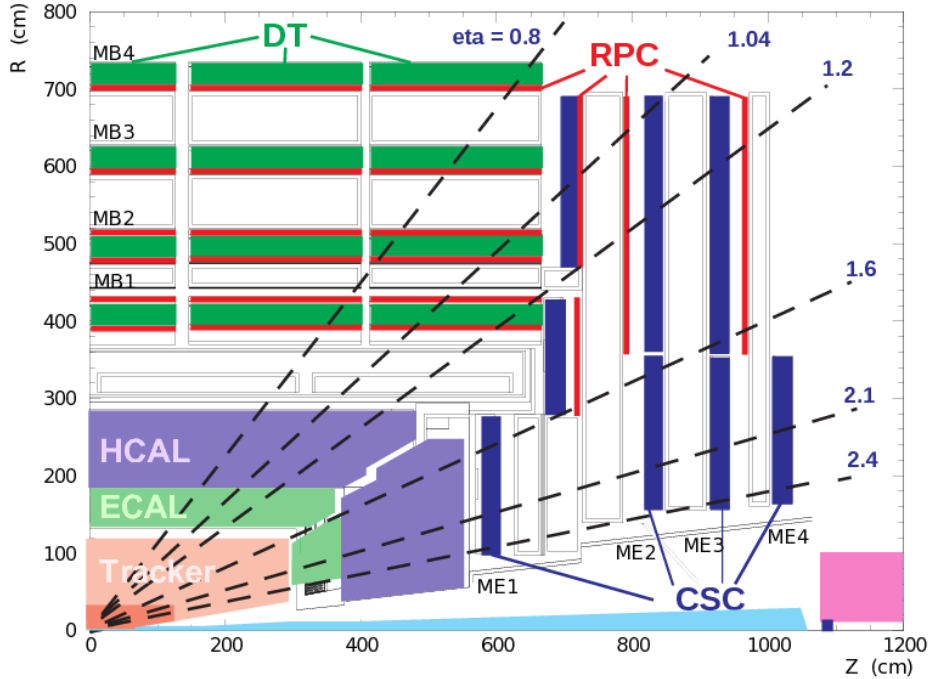


Figure 1.11: Longitudinal section of a quarter of CMS.

- **Drift tube (DT) stations** are used in the barrel region ( $|\eta| < 1.2$ ). The basic detector element is a drift tube cell, its section is represented in Figure 1.12. The cathodes define the boundary of the cells

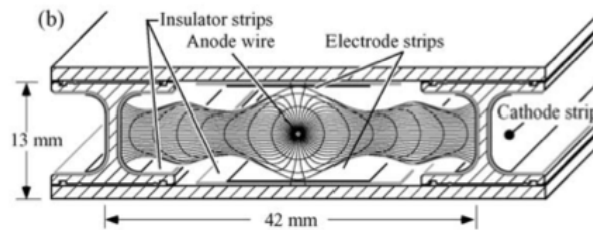


Figure 1.12: Section of a drift tube used in the barrel region of the muon system.

and serve as cathodes, the anode is a  $50 \mu\text{m}$  stainless steel wire placed in the centre of the cell. The distance of the track from the wire is measured by the drift time of the electrons produced by ionisation. The gas is a mixture of Ar (85%) and  $\text{CO}_2$  (15%), which provides good quenching properties and a saturated drift velocity, of about  $5.4 \text{ cm}/\mu\text{s}$ . Therefore the maximum drift time is about 390

ns, i.e. 15 bunch crossings. A single cell has an efficiency of about 99.8% and a resolution of  $\sim 180 \mu\text{m}$ . In the muon system are present a total of 195000 drift tubes.

- **Cathode Strip Chambers (CSC)** are used in the endcap regions ( $0.9 < |\eta| < 2.4$ ) where the magnetic field is very intense and inhomogeneous and where the charged particle rate is high. . CSCs are multiwire proportional chambers, they have a maximum dimension of 3.5 m to 1.5 m and are filled with a mixture of 30% Ar, 50% CO<sub>2</sub> and 20% CF<sub>4</sub>. The measurements of the coordinate  $\varphi$  of the track is done by CSCs with a resolution of  $50 \mu\text{m}$ . Simultaneously, the wire signals are read out, directly, and used to measure the radial coordinate with a coarse precision of approximately 0.5 cm. By combining multiple layers of chambers is possible to reach an high time resolution so that the correct bunch crossing can be assigned with over 99% efficiency.
- **Resistive Plate Chambers (RPC)** are present both in the barrel and in the endcaps regions. The RPCs have a limited spatial resolution, but an excellent time resolution ( $\sim 3 \text{ ns}$ ). This feature makes the RPCs capable of triggering events with muons with high efficiency. They are operated with a gas mixture of 95% C<sub>2</sub> H<sub>2</sub> F<sub>4</sub> and 5% C<sub>4</sub> H<sub>10</sub>.

### 1.2.7 The trigger system

The bunch crossing frequency at CMS interaction point is 40 MHz, but technical difficulties in handling, storing and processing extremely large amounts of data impose a limit of about 100 Hz on the rate of events that can be written to permanent storage. The goal of the trigger is to perform an on-line reduction of the data by a factor of  $10^7$ . The trigger must therefore be able to select events on the basis of their physics content, in an extremely short time, given that the bunch crossing time is 25 ns. But 25 ns is a time interval too small even to read out all raw data from the detector. The strategy used in CMS is to adopt a multi-level trigger design, where each step of the selection uses only part of the available data. In this way higher trigger levels have to process fewer events and have more time available, so they can analyze the events in full details using more refined algorithms. The CMS trigger is structured in two physical levels: the Level-1 (L1) Trigger and the High Level Trigger (HLT).

- **Level-1 Trigger:** it consists of custom-designed and largely programmable electronics. It reduces the rate of selected events from 40 MHz to 100 kHz. The full data are stored in pipelines of processing elements for a maximum time of  $3.2 \mu\text{s}$  while waiting for the

---

trigger decision. If an event is accepted the data are moved to the HLT. The reconstruction algorithms of the tracker do not allow an enough fast reconstruction of the event, hence only the readout from the calorimeter and the muon system is employed.

- **High Level Trigger:** is a software system (implemented in a single processor farm) which reduces the output rate from 100 kHz to 100 Hz. The strategy here is to perform a regional reconstruction of the event, only objects in an interesting region are reconstructed, for example in the proximity of a jet. The HLT has access to the high-resolution data stored in pipelined memories by the L1 as well as the information from the silicon tracker: it can therefore perform complex calculations, such as track reconstruction.

## Chapter 2

# Muon Reconstruction in CMS

In CMS the reconstruction of muon tracks is achieved using both the inner (the silicon tracker) and the outer part (muon spectrometer) of the detector. Muons with enough energy (i.e. larger than 3.5 GeV) can pass through the calorimeters and the solenoid and leave a signal in the muon system. The reconstruction of a muon starts with the *local reconstruction*, that is a method that combines few hits, calculate the path of the muon and propagates the information to a fit of the whole track. Both in the muon system and in the tracker starting from a series of hits a track or, if only two hits are registered, a segment is reconstructed. In pp collisions, tracks are firstly reconstructed independently in the silicon tracker and in the muon spectrometer. To identify a track as a muon track a matching between a track, or a segment, reconstructed in the muon system and a track reconstructed in the tracker is performed. A cross-check for the identification of a track as a muon track can be performed by checking the energy loss in the electromagnetic (ECAL) and the hadronic calorimeter (HCAL). In what follows is presented an overview on the muon track reconstruction method used in CMS.

## 2.1 Muons track reconstruction

In CMS different types of reconstruction of a muon track are available:

- **Global Muon reconstruction:** starting from a track reconstructed with the hits in the muon chambers (standalone muon) an algorithm matches it with a compatible track in the silicon tracker, then a fit is performed considering hits in both the inner tracker and the muon system. At high transverse momentum ( $p_T > 200$  GeV) the global muon reconstruction improves the resolution of the reconstructed track compared with the tracker muon reconstruction
- **Tracker Muon reconstruction:** in this approach is considered as muon candidate every track with  $p_T > 0.5$  GeV and  $p > 2.5$  GeV. The track is fitted using just the inner tracker hits information and a map of the material budget in the detector. The reconstructed track will be promoted to a tracker muon track if it matches at least one segment reconstructed in the muon system. At low momentum ( $p < 5$  GeV) this approach is more efficient compared to a global muon reconstruction, as the former needs just the reconstruction of at least one segment in the muon chambers, the latter at least two.

Most of the muons with enough energy coming from collisions are reconstructed as Global Muons or Tracker Muons or, very often, as both. However in the reconstruction could happen that both approaches fail and only hits in the muon system are registered. In these cases it is convenient to define a third category:

- **Standalone Muon reconstruction:** in this case a fit is performed using just the informations collected in the muon system. Thanks to a high reconstruction efficiency of the tracker, standalone muons represent only about 1% of all muons from collisions reconstructed in the detector.

The results of these three algorithms are merged into a single collection of muon candidates, each one containing information from the standalone, tracker, and, when available, the global fit. The expected resolution for muons in the very central ( $0 < |\eta| < 0.2$ ) and in the forward ( $1.8 < |\eta| < 2.0$ ) region of the tracker is shown in Figure 2.1. Here it is important to notice how a global reconstruction approach improves the resolution on the muon momentum at high  $p$ .

Candidates found both by the Tracker Muon and the Global Muon reconstruction that share the same tracker track are merged into a single candidate. In a similar way standalone muon tracks not included in a global muon are merged with a tracker muon if they share at least a muon segment. The combination of different reconstruction methods leads to an



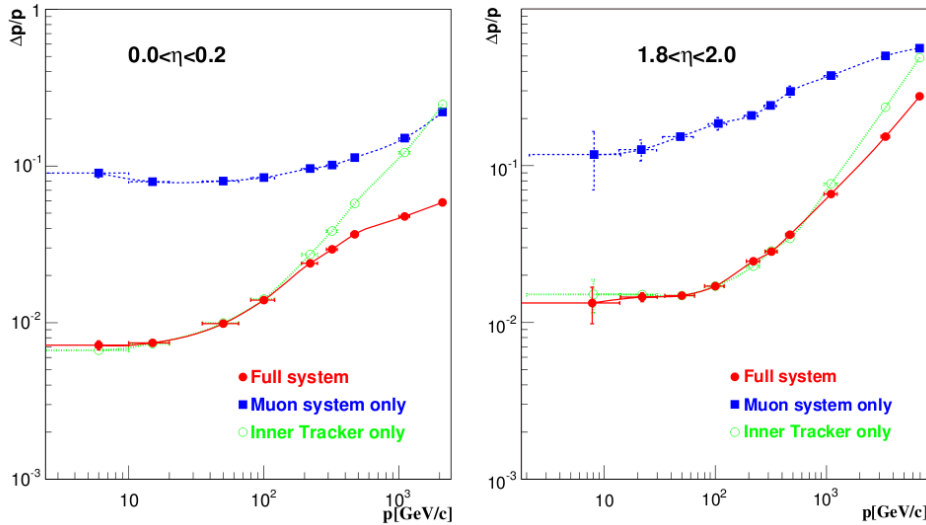


**Figure 2.1:** Expected resolution on muon momentum for global muon reconstruction (red), tracker muon reconstruction (green) and standalone muon reconstruction (blue). [1].

efficient and robust muon reconstruction. A physics analysis can achieve the desired balance between identification, efficiency and purity by applying a selection based on the muon identification variables (e.g.  $p_T$  or  $p$ ). In this thesis only muons with the track reconstructed in the tracker will be used.

In CMS many algorithms are available for the reconstruction of a charged particle track. In what follows is presented an overview on only two of them, the first is used in the online reconstruction of tracks performed by the HLT Trigger, the second is used internally in some alignment algorithms.

- **Kalman Filter:** represents a fast, efficient and versatile algorithm for the track fitting. It can take into account the multiple scattering effect of the particle and its energy loss. The Kalman filter is based on the progressive update of the trajectory of the particle from one hit to the next. This strategy makes the algorithm very fast and optimal for the online reconstruction of the tracks performed by the High Level Trigger.
- **Global Fit Algorithm:** Every time a measurement (hit on a sensor) is added to the set, the whole trajectory of the particle is refitted, this strategy increases the computing-time necessary to fit the track with respect to the Kalman filter. A global fit strategy is used in some alignment algorithms, such as *Millipede II* (see Section 2.2).

---

It has been demonstrated with simulations that in CMS the accuracy and the efficiency of track reconstruction with a global fit and with the Kalman filter are equivalent, then the one used in the offline reconstruction of the tracks is the latter. Since a track in the tracker is reconstructed combining hits in the silicon sensors, the resolution on the momentum of the track is significantly affected by the precision on the knowledge of the spatial position of every sensor. In what follows is presented an overview of the procedure to determine with high precision the spatial position of silicon sensors in the tracker.

## 2.2 Alignment

The procedure to determine the position of the silicon sensible elements inside the CMS detector is called *alignment*. After the detector assembly, the positions of the silicon sensors of the CMS tracker are known with a precision of  $O(100 \mu\text{m})$ . The uncertainty on the position of the sensors in the tracker can be represented at different levels: the hierarchy of levels for the pixel detector is represented in Figure 2.2a, and for the strip detector the hierarchy up to the module level in Figure 2.2b. Each element

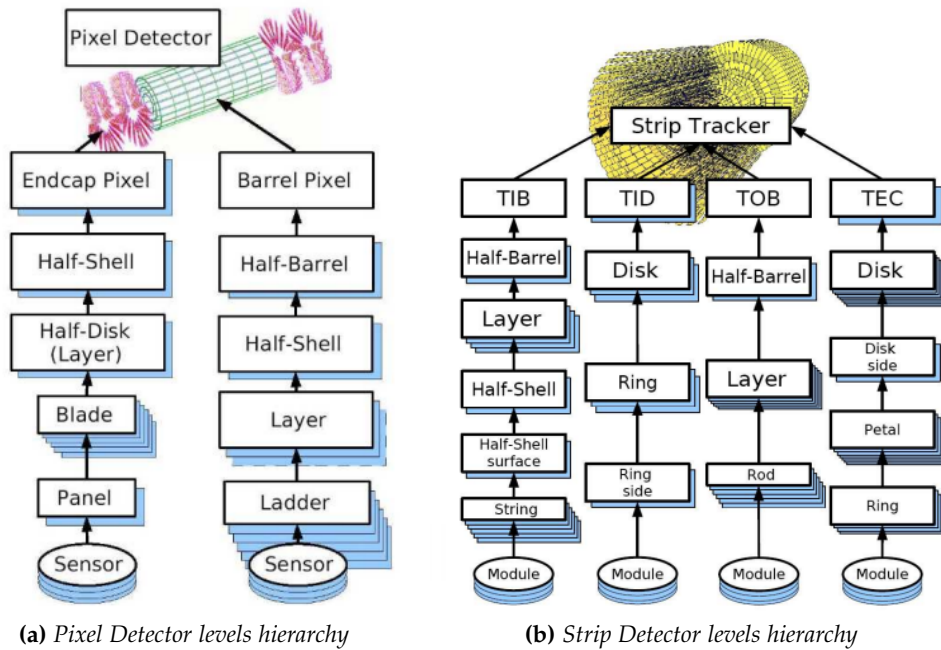


**Figure 2.2:** Hierarchy of the mechanical structures of the CMS tracker for the Pixel Detector and the Strip Detector.

of the hierarchy is allowed to *move* along all its six degrees of freedom and the movement of the parent structure is correctly propagated down to the daughters and vice versa. In the Strip Tracker there are two types of modules: those with a single silicon sensor and those with two silicon sensors mounted on. Therefore in modules with two silicon sensors the hierarchy at the module level split up again in two sensors. In the design both sensors are exactly on the same plane. However in a real situation small angles between their surfaces could exist. Referring to Figure 2.3, if with  $\alpha$  is denoted the angle between the surfaces, also called *kink angle*, typical values for  $\alpha$  are around 1 mrad. In CMS to every element of the hierarchy level represented (sensors excluded) in Figure 2.2 are assigned six geometrical parameters corresponding to rotations and translations.

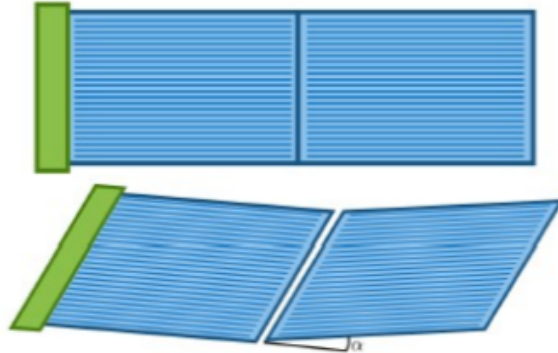


**Figure 2.3:** Angle between surfaces of two silicon sensors mounted on a module (kink).

Moreover for every module composed by two silicon sensors an additional parameter takes into account the kink angle  $\alpha$ . To every silicon sensor the assigned geometrical parameters divided in three categories:

- **Shift parameters:**  $(u, v, w)$  represent the translations of the module in three space directions. In these coordinates the silicon surface of the sensor is taken as a reference frame. Usually  $u$  is the coordinate in which the measurement of the hit has the highest precision,  $v$  the lowest precision and the coordinate  $w$  represents the direction normal to the module surface, where no measurement information exists. For a silicon strip sensor in the barrel region of the tracker, referring to the global reference frame in cylindrical coordinates  $(r\phi, z, r)$ ,  $u$  is along  $r\phi$ ,  $v$  is along  $z$  and  $w$  is in the  $r$  direction. A sketch of these parameters is shown in Figure 2.4. On the other

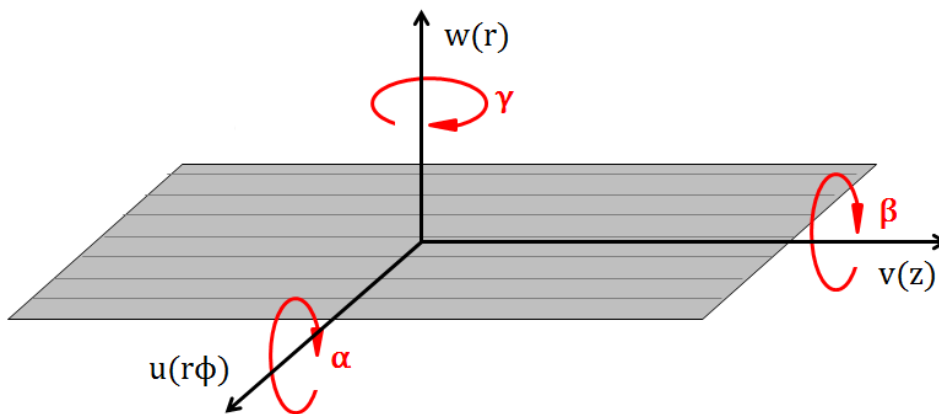


**Figure 2.4:** Alignment shift and rotation parameters defined in the local reference frame of a silicon strip sensor in the barrel region of the tracker

hand for a sensor in the endcap region  $u$ ,  $v$  and  $w$  are defined re-

spectively along  $r\varphi$ ,  $r$  and  $z$ . For a pixel sensor, the relation between the local and the global reference frame coordinates is by convention the same as a strip sensor.

- **Rotation parameters:**  $(\alpha, \beta, \gamma)$ : the first is the rotation around  $u$  direction, the second around  $v$  and the third around  $w$ . For a silicon strip sensor in the barrel region of the tracker the rotation parameters are shown in Figure 2.4.
- **Bow parameters:** called  $\omega_{20}$ ,  $\omega_{02}$  and  $\omega_{11}$ . As is shown in Figure 2.5 the formers are respectively the bow in  $u$  and  $v$  directions, the latter is the mixed term. BowS are second order shape corrections and can be parametrized via second order polynomials.

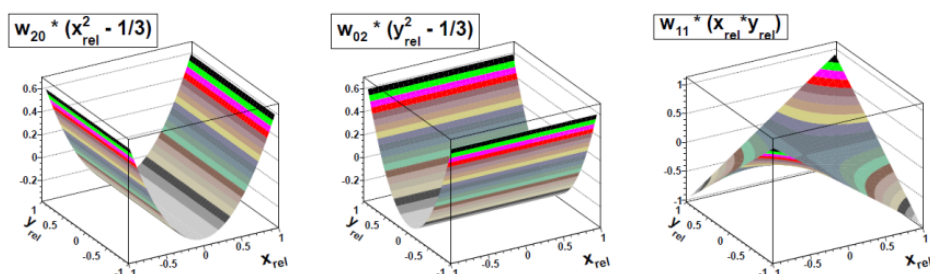


**Figure 2.5:** Bow parameters parametrizing three possible deformation of the silicon sensor surface.

The collection of the parameters of all the sensors of the tracker is a set of more than 100 000 parameters and is called *geometry* of the tracker. Clearly the quality of the reconstruction of a track inside the tracker depends on the considered geometry, the finer is the knowledge of the geometry, the more realistic is the reconstruction of the track. The knowledge of the geometry of the detector can be improved up to a few  $\mu\text{m}$  via an offline procedure called *track-based alignment*. The input to this procedure are simply the tracks reconstructed by the detector itself. The track-based alignment can be performed with different types of tracks:

- **Cosmic tracks:** muons coming from the high atmosphere can pass through tens of meters of dense material before being absorbed, hence although CMS is situated about 100 m underground they can reach the detector modules and leave a signal.
- **Collision tracks:** come from any particle produced in the pp collision that leave signals in the detectors.

- **Beam-halo tracks:** generated from the interaction of the beam particles with residual gas nuclei on the beam pipe in the proximity of the detector.

The basic idea of the track-based alignment procedure is to determine the position and the deformation of every silicon sensor in the tracker by fitting a track and comparing the result of the best fit with the position of the hits. When a track is fully reconstructed, two types of informations are available: the fitted trajectory and the measured hits. Consider a track with  $N$  measured hits, for every hit is built the so called *residual*:

$$\vec{r}_k = \vec{r}_k^{fit} - \vec{r}_k^{hit} \quad \text{for } k = 1, \dots, N \quad (2.1)$$

where  $\vec{r}_k^{hit}$  is the measured hit on the silicon sensor, and  $\vec{r}_k^{fit}$  is the hit on the sensor predicted by the fit of the track. The order of magnitude of  $\vec{r}_k$  is about  $10 \div 100 \mu\text{m}$  for the strip sensors and few  $\mu\text{m}$  for the pixel sensors. The goal of the track-based alignment procedure is to reduce the bias and uncertainty of the fitted parameters of the tracks by correcting the positions of the detector components. This typically strategy requires a collection of millions of tracks. By denoting with  $j$  a track in the collection, a global  $\chi^2$  also called *objective function* could be written as:

$$\chi^2 = \sum_j \sum_k \vec{r}_{j,k}^T V \vec{r}_{j,k} \quad \text{for } k = 1, \dots, N, \quad j = 1, \dots, M \quad (2.2)$$

where  $V$  is a covariance matrix built with the track parameters. Minimizing  $\chi^2$  means minimizing the residuals associated with the hits of the tracks. Residuals are strictly correlated to the position of the sensors and there is always new set of geometrical parameters for the sensors that makes  $\vec{r}_k \approx 0$ . This strategy reduces the bias and uncertainty of the fitted track parameters and improve the  $\chi^2$  of the track fit. Since the track-based alignment is performed offline, it is almost free from computing time limits. The algorithm currently used in CMS is the *Millipede II algorithm* [2] and is based on a global fit of the track.

When the detector was designed, the parameters describing the position of every silicon sensor was defined. The geometry represented by the collection of these parameters is called *design geometry*. Because of the fact that the detector assembly cannot be performed with infinite precision, a set of mechanical tolerances for the assembly of every component is defined. When the detector is assembled information about the relative position of the sensors within the supporting structures and of the large-level structures (such as TIB, TOB, etc.) within the Tracker is available from an optical survey analysis made prior to or during the Tracker integration. This includes Coordinate Measuring Machine (CMM) data and photogrammetry. These first survey procedures lead to the definition of a new geometry

---

called *survey geometry*. According to the precision of the measurements of the first surveys the survey geometry differs from the true geometry by about  $O(100\mu m)$ <sup>i</sup>.

Given a set of tracks of charged particles, the track-based alignment algorithm leads to the determination of a new geometry for the tracker, called *aligned geometry*. If the algorithm is applied in a proper way the aligned geometry describes the positions of the modules more realistically with respect to the initial survey geometry. Quantitatively the aligned and the true geometries differ from each other by about few  $\mu m$ . Despite the fact that the track-based alignment algorithm is very reliable there are still cases in which the aligned geometry can differ significantly<sup>ii</sup> from the true geometry. These cases are treated in the following section.

---

<sup>i</sup>This expression has to be intended in the following way: for every sensor or mechanical element of the detector its position as described in the initial-survey geometry differs from its true position by about  $O(100\mu m)$ .

<sup>ii</sup>The order of magnitude of these differences is not few  $\mu m$  but  $O(10\mu m)$  or even  $O(100\mu m)$

## 2.3 Weak modes

In some cases a track based alignment process minimizes the global  $\chi^2$  without finding the true positions of the sensors. A schematization of the behaviour of the track-based alignment algorithm is shown in Figure 2.6. The figure has the only purpose to show the behaviour of the track-based alignment algorithm, the represented magnitude of the translations with respect to the dimension of the sensors is not realistic. Both Figures 2.6a

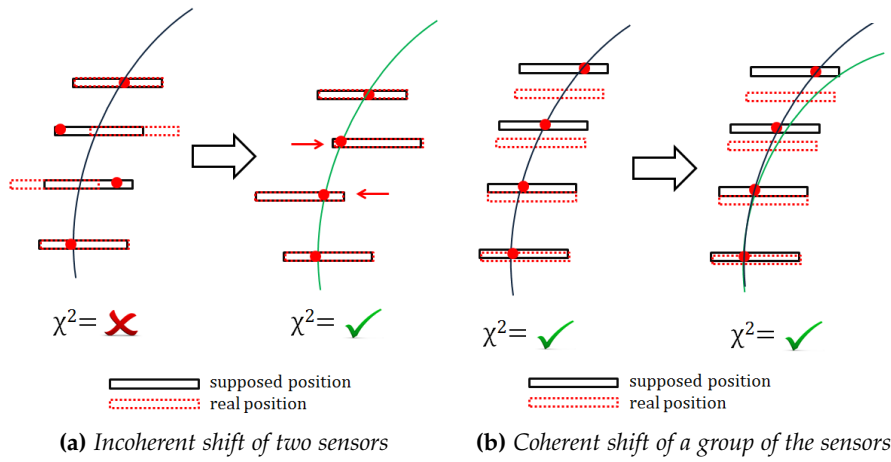


**Figure 2.6:** Behaviour of the alignment algorithm in case of incoherent and coherent translations of groups of sensors. In every figure the left part represents the pre-alignment situation, and the right part represents the positions of the modules, modified according to the global  $\chi^2$  minimization performed in track based alignment. The blue line refers to the fitted track, the green line refers to the true track. Both tracks are from charged particles and their curvature is induced by a magnetic field perpendicular to the figure.

and 2.6b compare the true positions of silicon sensors with the positions of the module assumed in the track fit. Assume that the alignment algorithm is taking as reference geometry for the determination of the residuals the survey geometry, the supposed positions of the sensors are then the positions described by the parameters of the survey geometry. Consider the true and supposed positions of the sensors in Figure 2.6a. When the difference between the true and the supposed position of a certain sensor is not coherent with the difference between the true and the supposed position of another sensor, the algorithm, in the process of  $\chi^2$  minimization, is able to find new positions of the sensors that matches the true ones. On the other hand in case that the difference between the true and the supposed position is coherent among a group of modules, as shown in Figure 2.6b, the  $\chi^2$  of the track is not significantly improved by translating the sensors. In this situation the positions of the sensors are not modified by the algo-



rithm. The relevant thing for a physics analysis in a reconstructed track is the set of parameters of the track. Consider for example the  $p_T$  of the track, refer to Figure 2.6a, the  $p_T$  of the fitted track before applying the alignment algorithm is very similar to the true one<sup>iii</sup>. What surely changes after the alignment process is the uncertainty on the  $p_T$  measurement, because the  $\chi^2$  minimization reduces the uncertainty on the determination of the track parameters. Consider now the case (Figure 2.6b) when the alignment algorithm has not updated the positions of sensors and consequently both the  $p_T$  associated to the track and the uncertainty on its determination are left unchanged. However is still present a significant difference between the fitted  $p_T$  (blue line) and the true  $p_T$  (green line).

The example presented above represents the case in which the sensors are translated, the same conclusions can be obtained by considering rotations or deformations of the sensors. The coherent translations, rotations or deformations of groups of sensors that modify the parameters of the tracks, are called *weak modes*. Weak modes do not degrade the fit of a track and its  $\chi^2$ . Hence an hypothetical procedure that has the purpose to assign realistic parameters to the track must not be based on the fit of tracks with the same topology. Another important aspect is that weak modes could be present in the geometry used to reconstruct real data and in the one used to reconstruct simulated data. Often in this thesis work data and simulation are compared. Since the simulation is a software in principle the true geometry used could be known. However to make the simulation realistic an uncertainty on the position of every sensor (or detector mechanical element) is introduced. This uncertainty has the same order of magnitude of the uncertainty on the positions of the sensors in a post track-based alignment geometry. Then the track-based alignment process determines an aligned geometry for the simulation too. Consequently despite weak modes are not intentionally introduced in the simulation they can be present anyway. This makes the simulation, as well as collected data, eligible to be processed by procedures that have the purpose to reassign realistic parameters to the tracks.

---

<sup>iii</sup>In fact in the picture they are so similar that appear superimposed and in the right part of the figure only the green line is visible.

## 2.4 Resonance reconstruction in the tracker

A possible approach that can reassign the true parameters to the tracks is an approach based on the reconstruction of dimuon resonances. The goal of this thesis is to find realistic parameters of the tracks with the use of the MuSclFit algorithm. MuSclFit is an algorithm based on the reconstruction of resonances. The basic idea of the following analysis is, starting from the aligned geometry, to reconstruct a resonance and measure its characteristics in the tracker. The measurement can be then compared with what is known of that specific resonance from previous experiments in order to detect possible systematic biases in the reconstruction. It is important to choose well known resonances, and especially those whose decaying products are well reconstructed in CMS. Hence muon-decaying resonances play a fundamental role as muons at the energy scale of GeV, for their characteristics of penetrating meters of dense material before being stopped, are in most of cases reconstructed with high efficiency and a clean signal. Furthermore it is mandatory to reconstruct adequately the chosen resonance, hence it is important to have good statistics and low background for the collection of the decaying products. In the energy regime of LHC there are some resonances that can be used to investigate the weak modes of the detector, examples are:  $J/\Psi$ ,  $\Psi'$ ,  $Y(1S)$ ,  $Y(2S)$ ,  $Y(3S)$ ,  $Z$ . The candidate chosen for the analysis in this work is the  $Z$  boson. Some of its characteristics can be found in Table 2.1.

Considering the luminosity reached in CMS in 2012,  $\approx 21 \text{ fb}^{-1}$ , and that

Characteristics of $Z$	
Charge	0
Spin	1
Mass	$91.1876 \pm 0.0021 \text{ GeV}$
Width	$2.4952 \pm 0.0023 \text{ GeV}$
$BR(\mu^+ \mu^-)$	$3.366 \pm 0.007 \%$
$BR(\text{invisible})$	$20.00 \pm 0.06 \%$
$BR(\text{hadrons})$	$69.91 \pm 0.06 \%$

**Table 2.1:** Properties of  $Z$  boson from the Particle Data Group [3].

the predicted cross section  $\sigma(pp \rightarrow ZX) \times BR(Z \rightarrow \mu\mu)$  at  $\sqrt{s} = 7 \text{ TeV}$  and  $\sqrt{s} = 8 \text{ TeV}$  is respectively  $0.972 \pm 0.042 \text{ nb}$  and  $1.13 \pm 0.04 \text{ nb}$  (NNLO calculation), the branching ratio of  $Z$  boson in muons of about 3% is reasonable for having enough statistics and perform an analysis based on it. Let's denote with *physics objects* all the tracks, particles, jets and groups of them reconstructed in CMS. Consider now two samples of muon pairs

from a selection described in Table 2.2, one collected in data taking and the other simulated. In order to detect the possible presence of weak modes in

<b>Muon selection for Z</b>	
$p_T$	$> 20 \text{ GeV}$
$ \eta $	$< 2.4$
$N_{Hits} \text{ Tracker}$	$\geq 10$

**Table 2.2:** Selection criteria for the muons in the samples that will be considered in the MuSclFit analysis.

the considered samples it is convenient to reconstruct the invariant mass of the muon pair in a region near the expected value of the Z mass, for example in the interval [71, 111] GeV, and then extract a value for the mass of the Z resonance by performing a fit on these distributions. Here three factors contribute to the shape of the distributions of the invariant mass of the dimuons:

- **The signal:** every dimuon event in which the hard scattering process is related to the exchange of  $Z/\gamma^*$ .
- **The background:** represented both by dimuon events non related to the exchange of  $Z/\gamma^*$  in hard scattering processes and combinatorial events.
- **The resolution of the detector:** muons are reconstructed in a detector that has a finite resolution. The effect on the tracks of the finite resolution of the detector is to smear the measured parameters of the tracks around their true values. The hypothesis for the fit of these distributions is that this spread follows a distribution parametrized by a Crystal Ball function (Equation 2.4) around the true value of the parameter.

The fit should take into account these contributions. The choice in this case is to fit with an exponential function that parametrizes the background added to a convolution between a Breit-Wigner function and a Crystal Ball function. Equation 2.3 shows the fit function  $f(m, \omega)$  as a function of the dimuon invariant mass  $m$  and of a set of unknown parameters  $\omega$ .

$$f(m, \omega) = f_{sig} \cdot \left( \frac{(\Gamma/2)^2}{(m - M_Z)^2 + (\Gamma/2)^2} \otimes CB \right) + (1 - f_{sig}) \cdot e^\lambda \quad (2.3)$$

Here  $CB = CB(m, \sigma, \alpha, \mu = 0, n)$  is a Crystall Ball function defined:

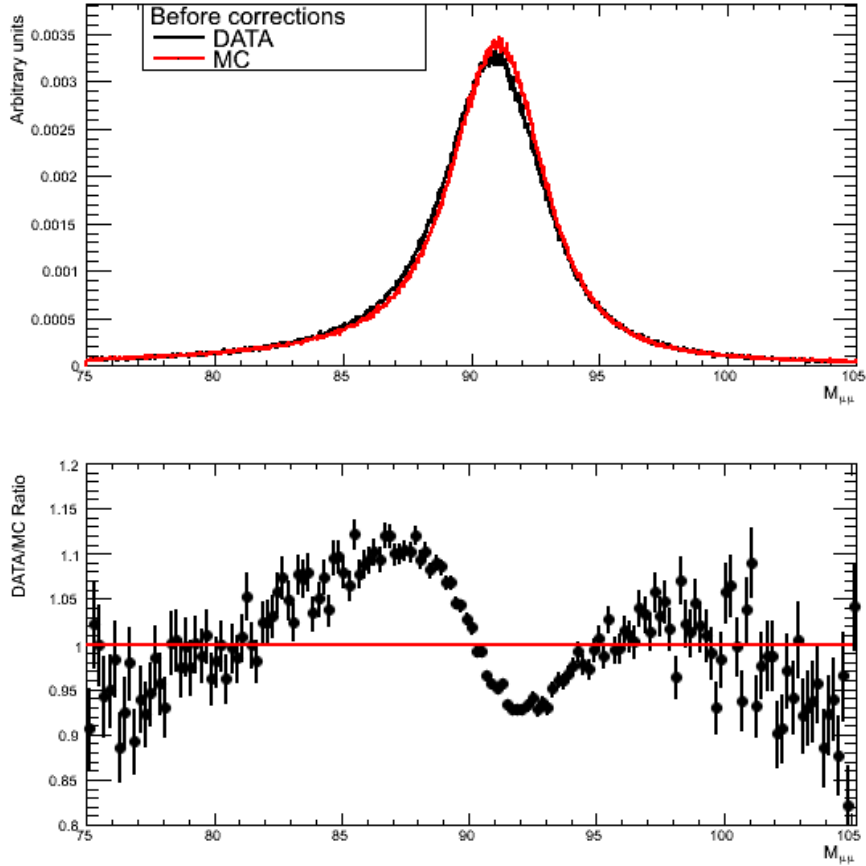
$$CB(m) = \begin{cases} e^{-\left(\frac{m^2}{2\sigma^2}\right)} & \text{for } \frac{m}{\sigma} > -\alpha \\ \left(\frac{n}{|\alpha|}\right)^n e^{-\left(\frac{|\alpha|^2}{2}\right)} \cdot \left(\frac{n}{|\alpha|} - |\alpha| - \frac{m}{\sigma}\right)^{-n} & \text{for } \frac{m}{\sigma} \leq -\alpha \end{cases} \quad (2.4)$$

The reason for using a Crystal Ball function instead of a gaussian function is that the signal contribution is not adequately parametrized by the Breit-Wigner function in the left-tail part of the distribution ( $m < M_Z$ ). The Crystal Ball function provides two free parameters ( $\alpha$  and  $n$ ) that can parametrize the shape of the left tail of the distribution. Therefore while the gaussian core of the Crystall Ball still gives a reliable parametrization of the resolution of the detector, no biases are introduced in the determination of  $M_Z$  by incorrect parameterization of the left tail of the distribution. In Figure 2.7 dimuons from pp collisions at  $\sqrt{s} = 7$  TeV from data collection during 2011 and from a full detector simulation are considered. Since different samples have in principle different background, the plots refer to a situation in which the background is subtracted. The subtraction of the background has been performed neglecting the fit statistical error on  $f_{sig}$  and  $\lambda$  since they are at least two order of magnitude smaller than their values. By comparing data and simulation it is possible to appreciate a difference between the shape of the dimuon invariant mass distributions. More precisely the peak value and the width of the distributions are not equal. The lower part of Figure 2.7 emphasises these differences with the ratio between data and simulation. The results of the fit for the data and the simulation are shown in Table 2.3. The difference between the fitted

Global results for aligned geometry		
Sample	Mass [GeV]	Sigma [GeV]
data	$91.109 \pm 0.004$	$1.378 \pm 0.005$
simulation	$91.240 \pm 0.002$	$1.388 \pm 0.003$

**Table 2.3:** Fit results for the full sample at  $\sqrt{s} = 7$  TeV.

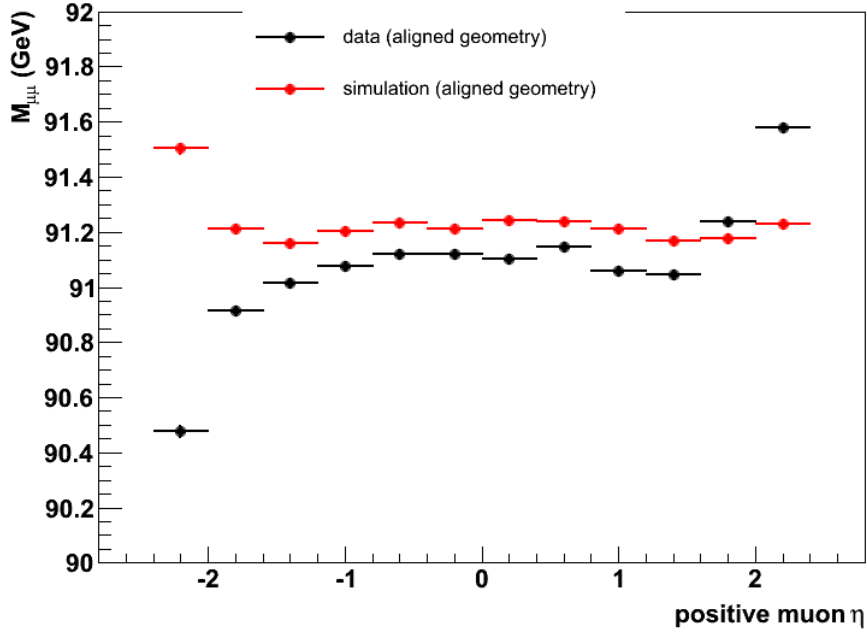
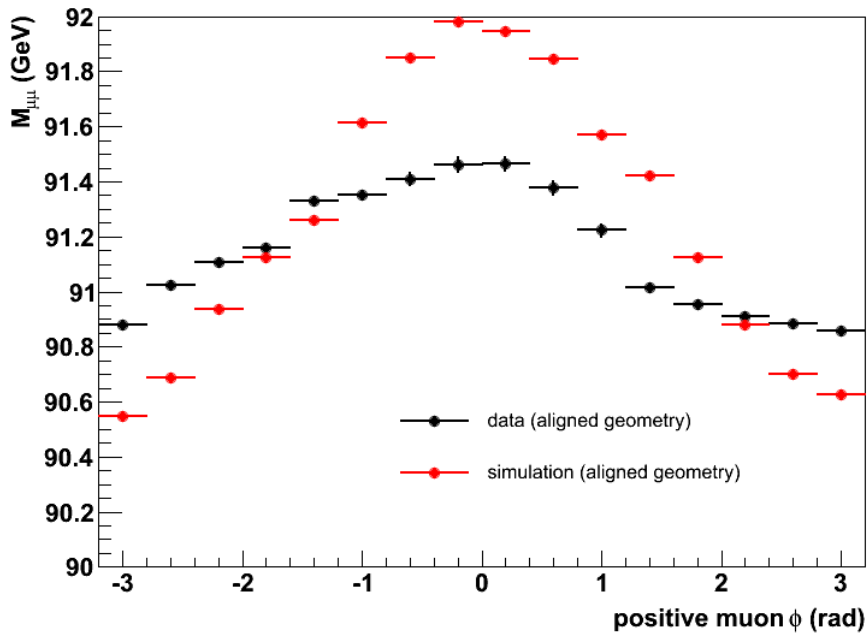
mass of data and simulation is about 1‰ and the resolution is about 10 MeV lower in the data. By comparing these values of  $M_Z$  with the nominal value it appears that the differences between them are of about 1‰ both in data and in the simulation. Anyway these differences are enough significant that can be the result of a muon reconstruction in presence of weak modes, both in the data and simulation aligned geometry. The distributions considered are built by taking into account every dimuon in the examined samples. Hence the values determined by the fits result from a compensation of biases in the tracks parameters determination in different geometrical regions of the tracker. It means that in some regions of the tracker these biases could be higher. In order to determine the magnitude of these biases it is convenient to reconstruct the  $Z$  resonance in different kinematic regions of the muons, for example in different  $\varphi$  or  $\eta$  separately for positive and negative muons. Using the collection of muons in the



**Figure 2.7:** Top: dimuon invariant mass reconstructed in the region  $[75, 105]$  GeV for both data (black) and simulation (red) at  $\sqrt{s} = 7$  TeV, both histograms have the same normalization, the error bars are proportional to the square root of number of events in each bin. Bottom: ratio between the plots of data and simulation, errors, from the plots at the top of the figure, are correctly propagated here.

data and in the simulation selected with the cuts described in Table 2.2 it is possible to build the distribution of the dimuon invariant mass and extract  $M_Z$  by performing a fit in different kinematical regions of the muon of a specific charge. Each fit is performed with the function defined in Equation 2.3, and the value of  $M_Z$  in every  $\eta$ -bin or  $\varphi$ -bin is plotted as in Figure 2.8. It clearly appears the presence of inhomogeneities between the fitted value of  $M_Z$  in different kinematical regions of the muon even inside a single sample. These inhomogeneities can be caused by residual weak modes in the aligned geometry, the magnitude of these biases is up to 1% of  $M_Z$ . In order to fully exploit the reconstruction potential and precision of the CMS detector they must be taken into account in the physics analy-

ses. The goal of this thesis is to reassign a new momentum to the muons by taking into account these biases, with the purpose to make more homogeneous the response of the tracker to the reconstruction of the muons and consequently of the resonances.

(a)  $M_Z$  vs  $\eta_+$ (b)  $M_Z$  vs  $\phi_+$ 

**Figure 2.8:** Value of the Z mass reconstructed from the dimuon invariant mass in different kinematic regions (positive muon). The error bar in each bin is smaller than the marker, and refers to the statistical error of the fit.

## Chapter 3

# Muon Calibration with the MuSclFit Algorithm

The MuSclFit package (acronym of Momentum Scale Fit) allows to perform analysis and calibration (intended as computing momentum scale corrections) of muons reconstructed in CMS. It consists in a series of C++ and python classes that can handle and modify the four-vectors of particles. The analysis in this thesis makes use of muons from a resonance decay, hence the input for MuSclFit will be muon pairs. The basic idea of the algorithm is to parameterize possible biases in the resonance reconstruction (see Chapter 2, Section 2.3) as a function of some kinematic variables, such as  $\varphi$ ,  $\eta$ ,  $p_T$ , by performing a multi-parameter likelihood fit, and then recover these biases by applying corrections that depend on the parameters found. During the data-taking of CMS, the algorithms used to identify and reconstruct physics objects continuously evolved. Moreover updates are very often made on the configuration of the trigger and the hardware components<sup>i</sup>. At the same time alignment studies determine new improved aligned geometries periodically. This continuous evolution on the data processing environment in CMS is present during the whole data collecting activity. Hence it is necessary, for each sample of reconstructed physics objects, to keep track of the environment used to process the data. A particular configuration of the data processing environment is denoted as *CMSSW release*. The priority of physics analyses is not to use samples processed within the latest CMSSW release but to know the configuration of processing environment in which the samples have been processed. Hence in CMS there are many CMSSW releases used by physics analyses and the MuSclFit algorithm, in order to produce suitable corrections for the muons reconstructed in each release must be robust and

---

<sup>i</sup>Configuration of the hardware components could be for example the list of electric channels inside the silicon modules, the threshold on the electrical noise etc.



flexible.

In this thesis results obtained with two CMSSW releases will be presented: CMSSW 4\_2\_X and CMSSW 5\_3\_X.

Conventionally in the label 4\_2\_X the number on the left indicates the most important changes in the data processing environment, such as a substantial improvement of the reconstruction algorithm with respect to the previous versions etc., and going from the left to the right the numbers denote progressively less important changes<sup>ii</sup>. The samples considered in this thesis are four, two are samples of muons from collision data and two are sample of simulated muons. Some of their characteristics are reported in the Table 3.1. The kinematical cuts on the tracks of the muons in every sample are the same listed in Table 2.2.

<b>Samples for muon calibration</b>				
Sample	CMSSW release	year	$\sqrt{s}$ [TeV]	$N$ of dimuons
data	4_2_X	2011	7	1870667
simulation	4_2_X	2011	7	3779949
data	5_3_X	2012	8	7282227
simulation	5_3_X	2012	8	2946698

**Table 3.1:** Details of the samples considered in this thesis.

<sup>ii</sup>The last number is indicated with X because denotes very minor changes in the data processing environment which do not affect the quality of reconstructed muons in the samples considered in this analysis

### 3.1 The MuSclFit likelihood

In this section the approach used in the MuSclFit algorithm is presented. It is a statistical approach that uses the measured mass of dimuons ( $m_{obs}$ ) as statistical observable. In this approach a probability is assigned to each event  $k$  according to  $m_{obs,k}$  and to the expected distribution of the dimuon invariant mass in the region [71, 111] GeV. Then a likelihood depending on these probabilities is built.

Let's start with the case where in the samples are present only dimuons from the resonance. If  $N_{ev}$  denotes the number of dimuons in the sample considered, the likelihood variable is simply:

$$\ln L = \sum_{k=1}^{N_{ev}} \ln [P_{sig}] \quad (3.1)$$

where  $P_{sig}$  represents the probability for the event  $k$  to be a signal event. The functional form of  $\ln L$  chosen is:

$$\ln L = \sum_{k=1}^{N_{ev}} \ln [f_{sig} P_{sig} + (1 - f_{sig}) P_{bgd}] \quad (3.2)$$

where the fraction of the signal  $f_{sig}$  is an unknown parameter. Here also the probability that an event is a background event  $P_{bgd}$  is present, and, similarly to  $P_{sig}$ , its parametrization is not trivial. While the functional form of likelihood in Equation 3.2 is independent on which resonance is chosen for the analysis, the explicit parametrizations of  $P_{sig}$  and  $P_{bgd}$  are not. In this work the resonance considered is  $Z$ , and the main topic of the following sections is to find a suitable functional form for its signal probability and background.

## 3.2 Building of the signal probability

For a detector with a perfect response, that is when the resolution can be neglected,  $P_{sig}$  is given by:

$$P_{sig}(m_{obs}, m_0) = \int dm \delta(m - m_{obs}) \sigma(m, m_0) = \sigma(m_{obs}, m_0) \quad (3.3)$$

Here  $\sigma(m, m_0)$  (also called *signal function* or *lineshape*) represents the theoretical distribution of the dimuon invariant mass in the proximity of the resonance  $m_0$ ;  $m_{obs}$  is the observed invariant mass of the dimuon, which depends on the kinematic variables of the muons and, in the form of a function of a set of unknown parameters, contains the parametrization for the scale of momentum of muons.

In order to extend the signal probability to a realistic case and to be able to compare the expected and the reconstructed distributions, an hypothesis for the detector effects on the tracks reconstruction should be made. A reasonable choice is to suppose that the effect of the detector on the dimuon reconstruction is that the parameters of the track are distributed around their true value according to a gaussian distribution. The standard deviation of this gaussian distribution is not a single value rather is a function of kinematic variables, such as  $\eta$ ,  $p_T$ , and it depends on unknown parameters that will be determined also by the likelihood maximization. With this prescription Equation 3.3 becomes a convolution between the gaussian resolution of the detector and  $\sigma(m, m_0)$ .

$$P_{sig}(m_{obs}, m_0) \propto \int dm \frac{\sigma(m, m_0)}{s} e^{-\frac{1}{2} \left( \frac{m - m_{obs}}{s} \right)^2} \quad (3.4)$$

Here  $s$  is the expected mass resolution function, which depends on the kinematics of the muons and, in the form of a function of a set of unknown parameters, holds the parametrization of the resolution of the muons in the tracker. Similarly  $m_{obs}$  holds the parametrization of the momentum scale of the muons in the tracker and depends on the kinematics of the muon and on a set of unknown parameters. The fit procedure change the values of the unknown parameters in order to find the maximum value for  $\ln L$ , this is the maximum likelihood method. In what follows a suitable parametrization for the functions  $m_{obs}$ ,  $s$  and  $\sigma(m, m_0)$  is investigated.

### 3.2.1 The signal function

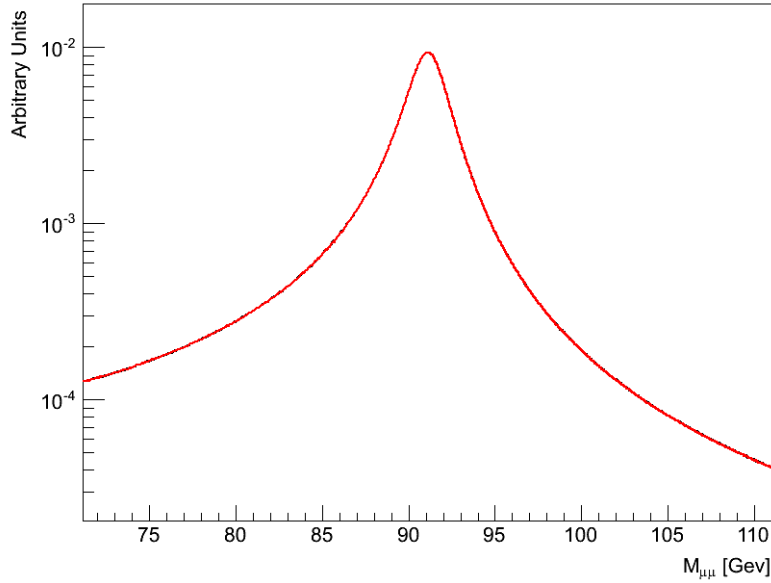
The signal function  $\sigma(m, m_0)$  represents the theoretical distribution of the dimuon invariant mass  $m$  in the proximity of the considered resonance  $m_0$  as it is predicted by the Standard Model. Since in this work the resonance considered is the Z boson, the distribution of  $m$  is defined in the proximity of  $m_0 = 91.188$  GeV. The production of Z boson in pp collisions

at  $\sqrt{s} = 7$  or  $\sqrt{s} = 8$  TeV is described in terms of partons interactions in the hard scattering process, and its decay into muons can be treated within the standard model with QCD, QED and electroweak corrections.

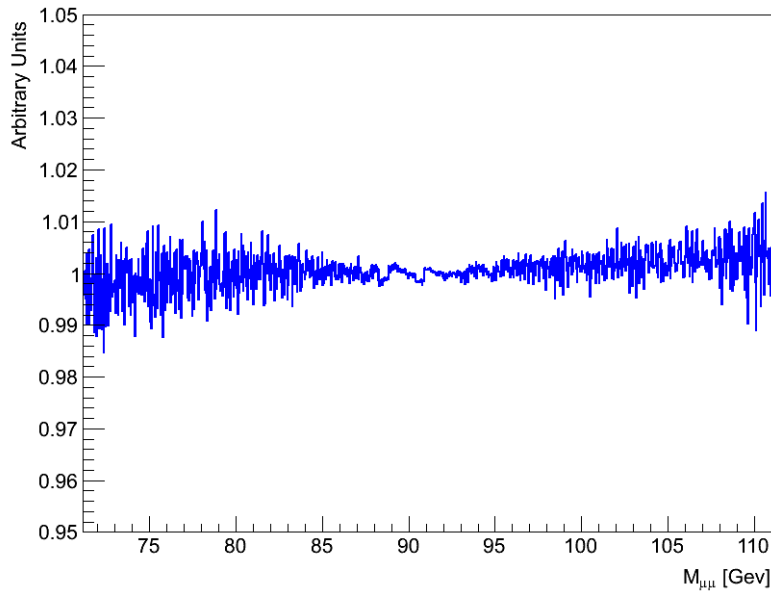
For this analysis an accurate prediction for the  $Z$  resonance decaying into muons has been calculated taking into account NLO Feynman diagrams for QED and electroweak corrections, both for  $\sqrt{s} = 7$  and  $\sqrt{s} = 8$  TeV and with a systematic uncertainty under 1%<sup>iii</sup>. The kinematic cuts on final state muons follow those applied on the reconstructed objects, and are  $|\eta| < 2.4$  and  $p_T > 18$  GeV. For the purpose of calibration an interval of invariant mass needs to be chosen: a too narrow interval near the peak value of the resonance, i.e.  $\pm 5$  GeV, will prevent the correct reconstruction in those kinematic regions where the bias in the reconstructed dimuon mass is larger, on the other hand if the interval is too large, for example  $\pm 40$  GeV, the fit would be affected by the tails of the distribution where a non-optimal parametrization can induce significant biases in the determination of the peak. As reference for the choice of a suitable interval, one can observe in Figure 2.8 that sometimes the peak value is  $1 \div 2$  GeV away from the nominal value. Keeping in mind that the resonance, which has natural half-width of about 1.25 GeV, is extra-smeared by the resolution of the detector, that is again  $1 \div 2$  GeV, and that a proper way to do the fit is to consider few standard deviations from the peak, we choose for the interval of the fit the window  $[71, 111]$  GeV. Figure 3.1a shows a superposition of the dimuon invariant mass distribution in the range  $[71, 111]$  GeV for  $\sqrt{s} = 7$  TeV and  $\sqrt{s} = 8$  TeV, and of their ratio (Figure 3.1b): the difference between the curves at  $\sqrt{s} = 7$  TeV and  $\sqrt{s} = 8$  TeV is very small, and in fact the use of two lineshapes, one for the 2011 samples at  $\sqrt{s} = 7$  TeV and the other for the 2012 samples at  $\sqrt{s} = 8$  TeV, is pretty equivalent to the use of only one of them.

The information contained in the theoretical lineshape is fed to MuSclFit in a particular and efficient way. Equation 3.4 represents a convolution between the theoretical lineshape and a gaussian with a standard deviation  $\sigma$  function of the kinematics of the muons. During the fit process  $\sigma$  change its value many times, and, if every time a convolution between the gaussian associated to that  $\sigma$  and the theoretical lineshape should be performed, the computing time for the maximization of the whole likelihood greatly increases, especially if the convolution, that is computed numerically, is made with an high precision. The smart choice to keep the computing time for the fit process reasonable and, at the same time, to have an high precision numerical convolution is to provide the fit tabulated values of the convolution. The choice made for this analysis is to produce convolutions of the theoretical lineshape with gaussians with

<sup>iii</sup>Calculations have been performed and systematic uncertainties were computed by Prof. Stefan Dittmaier (University of Freiburg), [4].



(a) Theoretical lineshapes for  $Z \rightarrow \mu\mu$  at  $\sqrt{s} = 7$  TeV (red plot) and  $\sqrt{s} = 8$  TeV (black plot).



(b) Ratio of the  $\sqrt{s} = 8$  TeV lineshape to the  $\sqrt{s} = 7$  TeV lineshape.

**Figure 3.1:** Theoretical distribution of dimuon invariant mass in the region [71, 111] GeV for both  $\sqrt{s} = 7$  and  $\sqrt{s} = 8$  TeV pp collisions. [ref. S. Dittmaier]

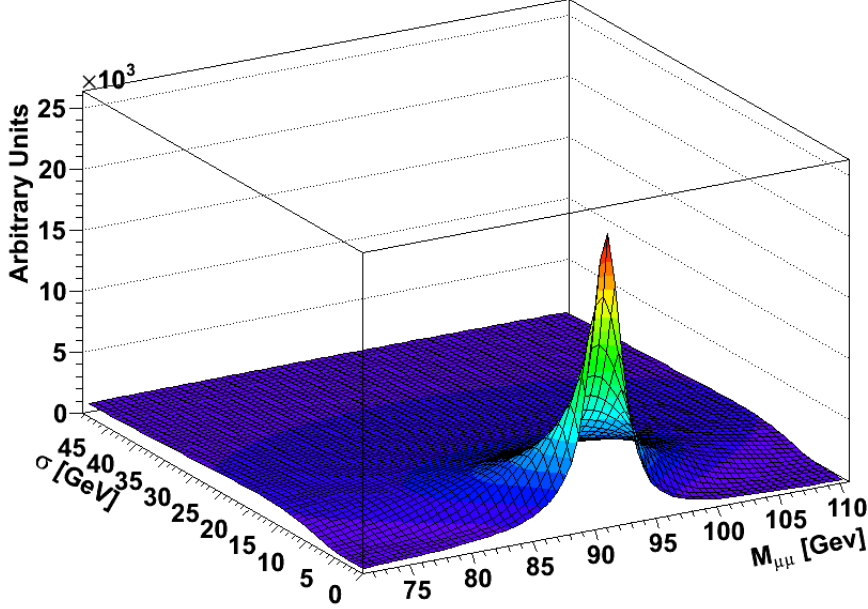


**Figure 3.2:** Two dimensional distribution of the convolution of the theoretical lineshape with 1000 gaussian functions of variable standard deviation ranging from 0 GeV to 50 GeV.

1000 different values for  $\sigma$ , from 0 GeV to  $\sigma = 50$  GeV. The value of 50 GeV for the resolution is not typical of an analysis that uses the tracker, but the MuSclFit algorithm has been developed for the calibration of objects reconstructed in every part of the detector. Standalone muons reconstructed in the muon system could have resolutions of tens of GeV, and other analyses with MuSclFit that use these types of muons can use on the tabulated values for the convolution computed in this analysis. All these informations can be easily stored in a two-dimensional histogram (a TH2 in ROOT). For the variable  $m$  1000 bins are chosen, such that every bin is 40 MeV wide; with all above prescriptions the TH2 that is the direct input for the fit process has a total of  $10^6$  bins. Figure 3.2 shows this histogram.

### 3.2.2 The parametrization of the momentum scale correction

The observed reconstructed mass of the muon pair  $m_{obs}$  is a function of the muons kinematics and contains the parametrization of the scale of the kinematic variables of the muons such as  $\eta$ ,  $\phi$ ,  $p_T$ ,  $Q$ . It is known from studies with simulated muons that the scale correction of the  $p_T$  is

at least one order of magnitude more important than the corrections of the other kinematical variables. Therefore the choice for this thesis is to introduce a scale correction only for the  $p_T$  of the muon. The bias on the reconstructed value of the mass shown in Figure 2.8 as a function of the variables  $\eta$  and  $\varphi$  is then parameterized through a correction of the  $p_T$  scale of the muons. Actually the scale correction is computed as a function of the *signed curvature*, defined as  $\kappa \equiv Q/p_T$ , where  $Q$  is the charge of the muon, so the curvature can assume positive or negative values. The reason for this choice has to be searched in the possible physical interpretation of the weak modes, i.e. the global deformations on the geometry of the tracker not corrected by the track based alignment. By building a simplified model of the path of a charged particle in vacuum in presence of a uniform magnetic field  $\vec{B}$  (see Figure 3.3) it is possible to see how the sagitta is related to the curvature by considering the following equations. Let  $\rho$  be the radius of curvature of the track in the magnetic field, if  $B$  is expressed in T,  $p_T$  in GeV and  $\rho$  in m it is:

$$r = \frac{p_T}{0.3 B} \quad (3.5)$$

and for  $\rho \gg L$  the sagitta:

$$s = \rho - \rho \cos(\theta/2) \approx \rho \left[ 1 - \left( 1 - \frac{\theta^2}{8} \right) \right] = \rho \frac{\theta^2}{8} = \frac{0.3BL^2}{8p_T}$$

Assuming that the primary effect of a global deformation is to introduce

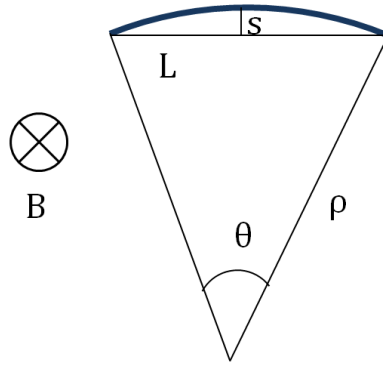


**Figure 3.3:** Trajectory of a charged particle in a magnetic field perpendicular to the direction of motion

a bias in the measurement of the sagitta of the track, it turns out why it is better to apply the correction to the curvature rather than to the  $p_T$ : a bias on the value of the sagitta is directly proportional to a bias on the curvature:

$$\Delta s \propto \Delta \kappa.$$

Hence the correction parameters used for the curvature are proportional to the effect of deformation on the tracker and, in principle, independent on the  $p_T$  of the track.

The correction on the curvature of the track is written as an ansatz function applied to the measured curvature  $\kappa$ . The ansatz function is denoted with  $F(\vec{\alpha}, \vec{x})$  and depends on kinematic variables  $\vec{x}$  and on a vector of parameters  $\vec{\alpha}$  to be determined by the fit. In principle  $\vec{x}$  should include all the kinematic variables affecting the curvature of the muon, that are the five helix track parameters, together with other environmental variables like the instantaneous luminosity, the track isolation, the number of hits of the track, the  $\chi^2/ndof$  associated with the reconstruction of the track, the type of track etc. However due to the fact that the number of tracks available for this analysis is limited,  $\vec{x}$  is just composed by  $\kappa$ ,  $\eta$  and  $\phi$  of the muon. The corrected curvature and the corresponding  $p_T$  of the track are:

$$\begin{aligned}\kappa^{corr} &= F(\vec{\alpha}, \vec{x}) \kappa \\ p_T^{corr} &= Q/\kappa^{corr}\end{aligned}\tag{3.6}$$

It is now possible to build the function  $m$  simply as the invariant mass of a dimuon pair. Using the basis  $(p_T, \varphi, \cot\vartheta)$  the four-momentum of the muon can be expressed in the following way:

$$p^\mu = \left( \sqrt{p_T^2 (1 + \cot^2 \vartheta) + m_\mu^2}, p_T \cos \varphi, p_T \sin \varphi, p_T \cot \vartheta \right)$$

and then the invariant mass of the dimuon with the  $p_T$  corrected according to Equation 3.6 is:

$$\begin{aligned}m &= \sqrt{p_{T-}^{2corr} (1 + \cot^2 \vartheta_-) + m_{\mu 1}^2} \sqrt{p_{T+}^{2corr} (1 + \cot^2 \vartheta_+) + m_{\mu 2}^2} + \\ & p_{T-}^{corr} p_{T+}^{corr} (\cos(\varphi_- - \varphi_+) + \cot \vartheta_- \cot \vartheta_+)\end{aligned}\tag{3.7}$$

A smart choice for  $F(\vec{\alpha}, \vec{x})$  will result in a fit with robust and physically acceptable parameters. As the correction is applied on the curvature, the functional form of  $F(\vec{\alpha}, \vec{x})$  is, in principle, not depending on which resonance is chosen for the calibration. The scale correction function used in this analysis is continuous in  $\eta$  and parametrized in five bins in  $\eta$ . The reason has to be searched in the detector structure, as the CMS tracker is composed by different substructures. Hence for example muons reconstructed in the barrel could present different biases with respect to those reconstructed in the endcap. Considering the structure of the tracker as shown in Figure 3.4, a convenient choice for the five  $\eta$  bins of the scale function is  $[-2.4, -2.1]$ ,  $[-2.1, -1.5]$ ,  $[-1.5, 1.5]$ ,  $[1.5, 2.1]$ ,  $[2.1, 2.4]$ . These



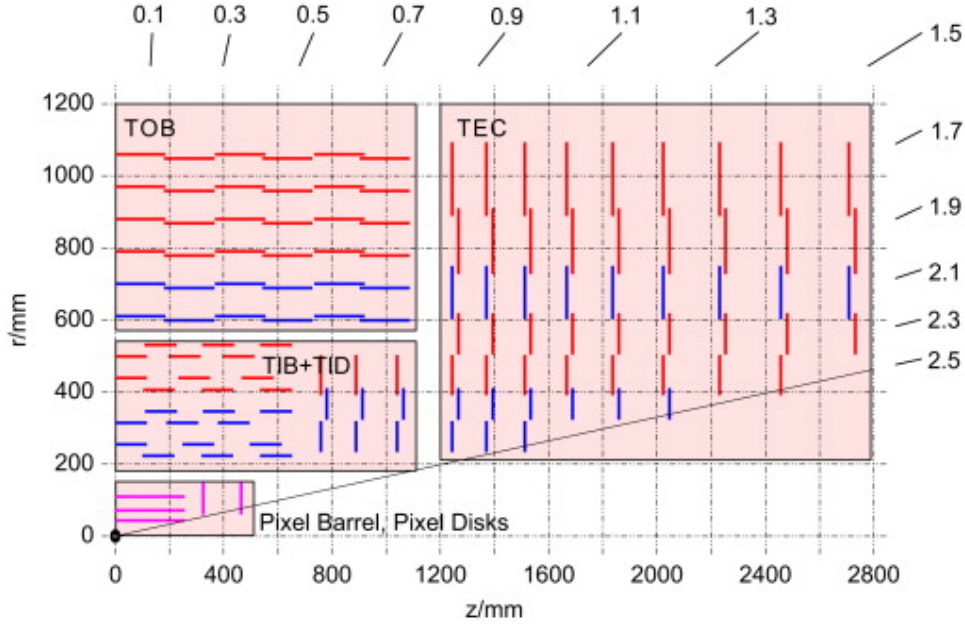


Figure 3.4: Longitudinal view of one quarter of the structure of the silicon tracker

bins will be referred to as Very Backward (VBWD), Backward (BWD), Barrel (BAR), Forward (FWD) and Very Forward (VFWD) bin. The scale correction function used is defined as:

$$F(\vec{\alpha}, \vec{x}) = (1 + p_0) \left( 1 - \frac{C_j(\eta, \varphi)}{\kappa} - \frac{\delta}{2\kappa} \right) \quad (3.8)$$

where  $p_0$  and  $\delta$  are constant in  $\eta$  and  $C_j(\eta, \varphi)$  is the  $\eta$ -binned term:

$$\begin{aligned} C_1(\eta, \varphi) &= a_{1,1} \sin(\varphi + \varphi_{1,1}) + a_{2,1} \sin(2\varphi + \varphi_{2,1}) + b_1(\eta - \eta_{0,1}) + b_{0,1} && \text{VBWD} \\ C_2(\eta, \varphi) &= a_{1,2} \sin(\varphi + \varphi_{1,2}) + b_2(\eta - \eta_{0,2}) + b_{0,2} && \text{BWD} \\ C_3(\eta, \varphi) &= a_{1,3} \sin(\varphi + \varphi_{1,3}) + b_3(\eta - \eta_{0,3}) + b_{0,3} && \text{BAR} \\ C_4(\eta, \varphi) &= a_{1,4} \sin(\varphi + \varphi_{1,4}) + b_4(\eta - \eta_{0,4}) + b_{0,4} && \text{FWD} \\ C_5(\eta, \varphi) &= a_{1,1} \sin(\varphi + \varphi_{1,1}) + a_{2,1} \sin(2\varphi + \varphi_{2,1}) + b_5(\eta - \eta_{0,1}) + b_{0,1} && \text{VFWD} \end{aligned}$$

here  $b_{0,3}$  is fixed to 0 and  $\eta_{0,j}$  with  $j = 1, 2, 3, 4, 5$  represents the boundaries in  $\eta$  and are respectively equal to  $-2.4, -2.1, -1.5, 1.5, 2.1$ . The continuity

of the scale function on these boundaries leads to four constraints:

$$\begin{aligned}
b_1(\eta - \eta_{0,1}) + b_{0,1} &= b_2(\eta - \eta_{0,2}) + b_{0,2} & \text{in } \eta = -2.1 \\
b_2(\eta - \eta_{0,2}) + b_{0,2} &= b_3(\eta - \eta_{0,3}) + b_{0,3} & \text{in } \eta = -1.5 \\
b_3(\eta - \eta_{0,3}) + b_{0,3} &= b_4(\eta - \eta_{0,4}) + b_{0,4} & \text{in } \eta = 1.5 \\
b_4(\eta - \eta_{0,4}) + b_{0,4} &= b_5(\eta - \eta_{0,5}) + b_{0,5} & \text{in } \eta = 2.1
\end{aligned}$$

According to the convention used for the names, the vector of unknown parameters  $\vec{a}$  has 21 elements:

$$\vec{a} = (p_0, \delta, \mathbf{a}_1, \mathbf{a}_2, \boldsymbol{\varphi}_1, \boldsymbol{\varphi}_2, \mathbf{b})$$

where the geometrical meaning of the parameters is:

$$\begin{aligned}
\mathbf{a}_1 &= (a_{1,1}, a_{1,2}, a_{1,3}, a_{1,4}, a_{1,5}) & 1^{st} \text{ harmonic amplitude} \\
\mathbf{a}_2 &= (a_{2,1}, a_{2,2}) & 2^{nd} \text{ harmonic amplitude} \\
\boldsymbol{\varphi}_1 &= (\varphi_{1,1}, \varphi_{1,2}, \varphi_{1,3}, \varphi_{1,4}, \varphi_{1,5}) & 1^{st} \text{ harmonic phase} \\
\boldsymbol{\varphi}_2 &= (\varphi_{2,1}, \varphi_{2,2}) & 2^{nd} \text{ harmonic phase} \\
\mathbf{b} &= (b_1, b_2, b_3, b_4, b_5) & \eta \text{ slope}
\end{aligned}$$

According to Equation 3.6 the corrected curvature of muons is finally given by:

$$\kappa' = (1 + p_0) \left( \kappa - C_j(\eta, \varphi) - \frac{\delta}{2} \right) \quad (3.9)$$

and the invariant mass  $m$  is built with it. The functional form of Equation 3.9 leads to a possible physical interpretation for its parameters. For example  $p_0$  could parametrize an incorrect description of the intensity of the magnetic field in the barrel, or an incorrect estimation of the energy loss of the muon in the tracker<sup>iv</sup>, and  $\delta$  parametrize any bias in the measurement of the curvature dependent on the charge of the muon. Moreover the physical interpretation of the  $\mathbf{a}_1, \mathbf{a}_2, \boldsymbol{\varphi}_1, \boldsymbol{\varphi}_2$  parameters will be discussed in Chapter 4.

### 3.2.3 The parametrization of the momentum resolution

The  $s$  function represents the parametrization of the mass resolution of the detector and is strictly connected to the scale function through Equation 3.4. As explained before, Equation 3.4 contains the hypothesis that the effect

<sup>iv</sup>The typical energy loss of a muon with  $p_T > 20$  GeV in the tracker is about 40 MeV.

of the passage through matter of the particle and the reconstruction of the track starting from the hits on the silicon modules is to change the track parameters, for example the  $p_T$ , around its true value with a gaussian smearing. Therefore the effect on a reconstructed resonance manifests itself as a gaussian widening of the invariant mass distribution. It is the task of the likelihood to estimate the extent of this gaussian widening in different regions of the tracker where the muon is reconstructed. The resolution on the reconstructed mass in a general case can be written as:

$$s = \sqrt{\left(\frac{\partial m}{\partial \kappa}\right)^2 \sigma_\kappa^2 + \left(\frac{\partial m}{\partial \varphi}\right)^2 \sigma_\varphi^2 + \left(\frac{\partial m}{\partial \cot \vartheta}\right)^2 \sigma_{\cot \vartheta}^2} \quad (3.10)$$

here  $\sigma_\kappa$ ,  $\sigma_\varphi$ ,  $\sigma_{\cot \vartheta}$  depends in principle on every variable associated with the muon reconstruction  $\vec{x}$ , and on sets of unknown parameters  $\vec{\beta}$ ,  $\vec{\gamma}$ ,  $\vec{\delta}$  that the fit has the task to determine:

$$\begin{aligned} \sigma_\kappa / \kappa &= G(\vec{\beta}, \vec{x}) \\ \sigma_\varphi &= G(\vec{\gamma}, \vec{x}) \\ \sigma_{\cot \vartheta} &= G(\vec{\delta}, \vec{x}) \end{aligned} \quad (3.11)$$

Previous studies with simulated muons showed that the uncertainty on the determination of  $\eta$  and  $\varphi$  is at least one order of magnitude smaller with respect to the uncertainty on the determination of the  $p_T$ . Since the number of tracks in the samples considered is limited, in this analysis  $G(\vec{\gamma}, \vec{x})$  and  $G(\vec{\delta}, \vec{x})$  are neglected, and the kinematic variables  $\vec{x}$  used to parametrized the smearing (resolution) are  $p_T$  and  $\eta$  of the muon. In what follows  $G(\vec{\beta}, \vec{x})$  will be called resolution function and, for what concerns the resolution, the fit is left with just one set of unknown parameters to estimate:  $\vec{\beta}$ .

Similarly to the scale function,  $G(\vec{\beta}, \vec{x})$  is an ansatz function. An hypothesis on its functional form is made, and by checking the convergence of the fit and the effect on the calibration it is possible to either reject or accept it as a good hypothesis. The choice of the functional form can be studied using the muons in sample of simulated events. In the generated muons it is available, beside the reconstructed curvature ( $\kappa_{reco}$ ) of the muons, the true one ( $\kappa_{gen}$ ), that is not affected by the reconstruction in the detector. In this thesis  $\kappa_{gen}$  is the true curvature of the muon after the emission of the final state radiation i.e. QED FSR. This information is obviously not present in the samples containing real muons. In the hypothesis of gaussian resolution of the detector an histogram with the variable  $(\kappa_{reco} - \kappa_{gen}) / \kappa_{gen}$  will result in a gaussian distribution peaked in 0. Figure 3.5 shows an example of the distribution of this variable and a fit with a gaussian function. By fitting these distributions in  $\eta$  bins with a gaussian, it is possible estimate the variable  $\sigma_\kappa / \kappa$  for the reconstructed events in that bin of  $\eta$ . The results

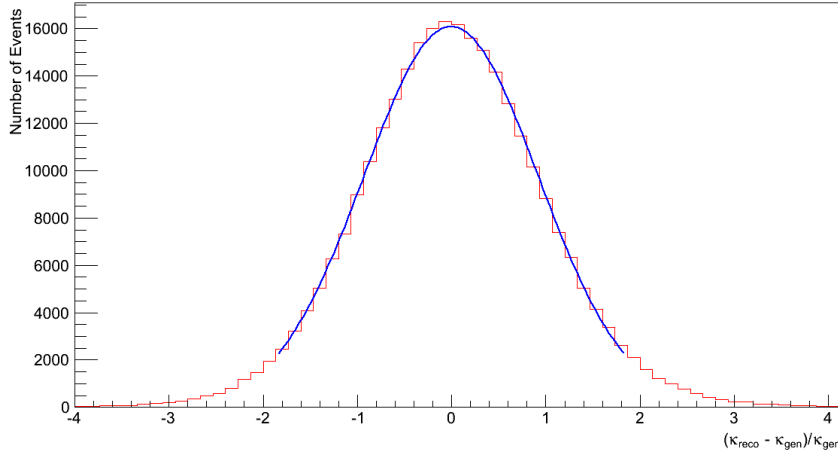


**Figure 3.5:** Example of one distribution of  $(\kappa_{reco} - \kappa_{gen})/\kappa_{gen}$  fitted with a gaussian function

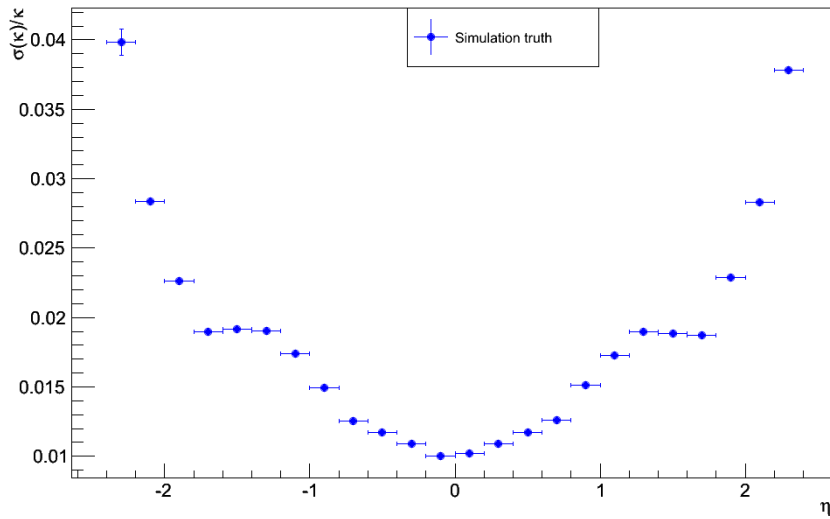


**Figure 3.6:** Distribution of the fitted values of  $\sigma_{\kappa}/\kappa$  in function of  $\eta$ .

of this procedure for 24 bins in  $\eta$  is shown in Figure 3.6. The plot gives some guidance on the decision of the functional form of the resolution function  $G(\vec{\beta}, \vec{x})$ . Taking into account the generated information, a good hypothesis for the functional form of  $G$  for the calibration with muons from  $Z$  is Equation 3.12.

$$G(\vec{\beta}, \vec{x}) = q_0 p_t \oplus q_j \quad \text{in } \eta\text{-bin } j \quad (3.12)$$

This parametrization is a piecewise function composed by constant functions, as no condition about its continuity is imposed. The choice of 12 bins in  $\eta$  has been found optimal for taking into account the structure of the tracker and the amount of tracks in the sample considered. The  $\eta$  bins chosen for this analysis are (from  $j = 1$  to  $j = 12$ ):

$$\begin{array}{cccc} [-2.4, -2.0], & [-2.0, -1.8], & [-1.8, -1.6], & [-1.6, -1.2], \\ [-1.2, -0.8], & [-0.8, 0], & [0, 0.8], & [0.8, 1.2], \\ [1.2, 1.6], & [1.6, 1.8], & [1.8, 2.0], & [2.0, 2.4] \end{array}$$

The total number of free parameters introduced by the resolution function is 13, then, considering 22 parameters of the scale function, with this configuration the fit has to determine 35 free parameters.

### 3.3 Building of background probability

In MuSclFit the background in its general meaning can denote different kinds of phenomena, such as fake electronics signals, cosmic or beam halo particles passing through the detector, or particles produced in processes not interesting for the specific analysis. Here the background is not represented by fake electronics signals rather than muons produced in processes not interesting for the purpose of this analysis. In an event of proton collision at the typical energies of LHC, thousands of particles are produced but only a small amount of them are muons with the required kinematical characteristics (see Table 3.1). A positive and a negative muon, if present and coming from the same vertex, are then associated to the same parent particle. In principle any process in QED, Electroweak and QCD that can lead to dimuon in the selected window of invariant mass could have produced the pair of muons.

At the typical  $M_{\mu\mu}$  region of  $Z$  the events produced by other sources than  $Z$  are a small percentage. These could be for example:

- *Dibosons* : two  $W$  mediate the interaction instead of the  $Z$ , for example:  $q\bar{q} \rightarrow WW \rightarrow \nu_{\mu}\bar{\nu}_{\mu}\mu^+\mu^-$ .
- $t\bar{t}$  : can decay in *leptons* or *leptons + jets*.

At low invariant mass (i.e. about 5 GeV) the situation is different. Consider the reconstruction of  $M_{\mu\mu}$  in a region where nearby resonances are present, for example the  $Y(2S)$  region; here, other than QCD processes, the contribution to the spectrum from the nearby resonances, such as  $Y(1S)$  and  $Y(3S)$ , is important and can be of the order of magnitude of the signal.

Beside the presence of muons not produced in the desired process, in the sample can be recorded pairs of muons not originating from the same parent particle, the so called combinatorial background events. These kind of events occur when muons from different parent particles are associated to the same vertex by the reconstruction algorithm (not necessarily a computational defect of the algorithm rather than the proximity of the vertexes much smaller than the resolution of the detector). They occur more frequently in low invariant mass, that for the LHC collision energies is below 10 GeV, and very rare in the region  $M_{\mu\mu} \approx 90 \text{ GeV}$  that is the one interesting in this analysis.

Goal of the selection on the muons is to restrict the kinematical regions in order to make the muon pair more likely produced by the desired resonance rather than another process. In this analysis the selection applied on muons is optimal for the reconstruction of  $Z$  resonance.

In MuSclFit the probability for an event to be a background event is represented in Equation 3.2 by  $P_{bgd}$ . Given the fact that the free parameters

to be determined by the fit are already 13 from the resolution and 21 from the scale function it is not convenient to determine more parameters in the fit itself. When a parameter is added to the set of the free parameters the computing time required for the fit increases. In order to not introduce more degrees of freedom in the fit, the background will be treated in a different way with respect to the scale and resolution function. The idea is to find a suitable parameterization for the background externally to MuSclFit, and provide the fit with tabulated values of the parameters. In what follows is presented a description of this strategy.

### 3.3.1 Parametrization of the background

Since the background is strongly dependent on the kinematic of the muons any suitable parametrization for it should take into account the situation in which the muon is reconstructed. The choice for this work is to reconstruct the invariant mass distribution in  $\eta$  bins of the muons. In Table 3.2 are listed the 16 kinematic bins in which the background is parameterized. To quantitatively appreciate the different backgrounds it is possible

Background kinematic bins		
Bin ID	$\eta_-$ interval	$\eta_+$ interval
1	$[-2.4, -1.5]$	$[-2.4, -1.5]$
2	$[-2.4, -1.5]$	$[-1.5, 0.0]$
3	$[-2.4, -1.5]$	$[0.0, 1.5]$
4	$[-2.4, -1.5]$	$[1.5, 2.4]$
5	$[-1.5, 0.0]$	$[-2.4, -1.5]$
6	$[-1.5, 0.0]$	$[-1.5, 0.0]$
7	$[-1.5, 0.0]$	$[0.0, 1.5]$
8	$[-1.5, 0.0]$	$[1.5, 2.4]$
9	$[0.0, 1.5]$	$[-2.4, -1.5]$
10	$[0.0, 1.5]$	$[-1.5, 0.0]$
11	$[0.0, 1.5]$	$[0.0, 1.5]$
12	$[0.0, 1.5]$	$[1.5, 2.4]$
13	$[1.5, 2.4]$	$[-2.4, -1.5]$
14	$[1.5, 2.4]$	$[-1.5, 0.0]$
15	$[1.5, 2.4]$	$[0.0, 1.5]$
16	$[1.5, 2.4]$	$[1.5, 2.4]$

**Table 3.2:** Kinematic intervals used for the parametrization of the background:  $\eta_-$  and  $\eta_+$  are referred to negative and positive muons respectively.

to plot the dimuon invariant mass distribution in two kinematic regions and perform a fit on it with an adequate function. In what follows the

sample used is a sample of  $\sqrt{s} = 7$  TeV data in 4\_2\_X. The fits for regions with Bin ID = 1 both muons in the backward Endcap and Bin ID = 6 both muons in the Barrel, are performed with the functional form described in Equation 2.3. The results are shown in Figure 3.7, the interesting parameters here are the exponential constant, denoted as  $expC$ , and the fraction of signal with respect to the background, denoted as  $fSig$ . Note that in the case the muons go both in the barrel, the exponential constant is 40% lower, and the signal fraction 1% higher with respect to the other case. This represents the main evidence of the fact that the parametrization of the background should be differentiated in function of the kinematics of the muons.

Taking into account these considerations it is now possible to build the  $P_{bgd}$  probability: it depends on a set of parameters  $\vec{\epsilon}$  made by exponential constants in different kinematical bins. Referring to Table 3.2, if with the index  $i$  is denoted a specific bin with Bin ID =  $i$  then the probability for an event of measured invariant mass  $m_{obs}$  to be a background event is:

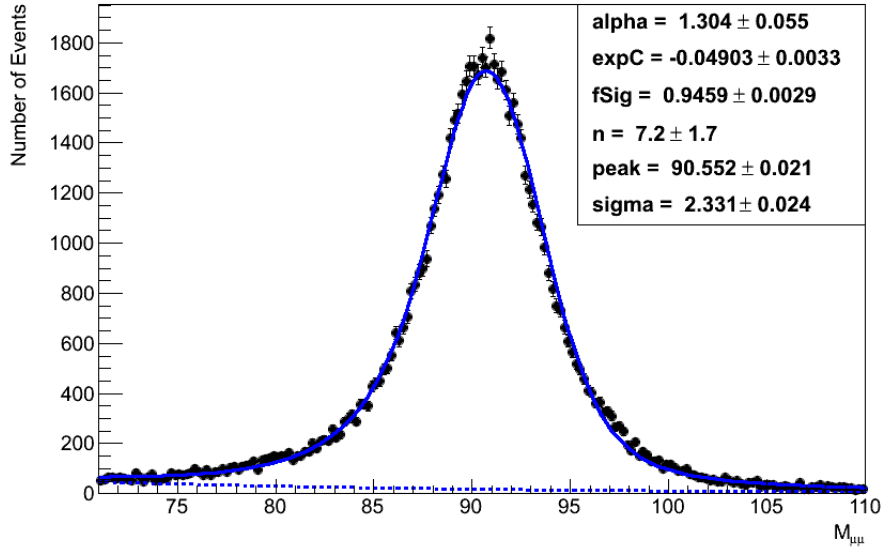
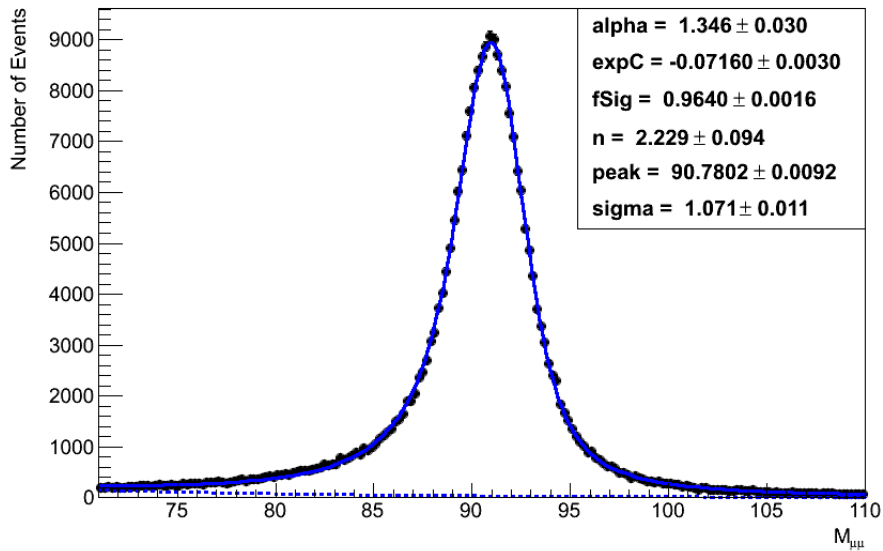
$$P_{bgd}(m_{obs}, \vec{\epsilon}) \propto e^{\epsilon_i m_{obs}} \quad (3.13)$$

Finally the probability to observe a dimuon with a reconstructed invariant mass  $m_{obs}$ , coming either from signal or from background can be written as:

$$P_{evt} = f_{sig,i} \cdot P_{sig}(m_{obs}, \vec{\alpha}, \vec{\beta}) + (1 - f_{sig,i}) \cdot P_{bgd}(m_{obs}, \vec{\epsilon}) \quad (3.14)$$

where  $f_{sig,i}$  denotes the signal fraction in the kinematical bin  $i$  of the muons. Considering Equation 3.14 it is now possible to say that in this analysis the likelihood maximization in MuSclFit is performed with 34 free parameters, 21 of the scale function and 13 of the resolution parametrization.



(a) Fit for  $M_{\mu\mu}$  distribution for Bin ID = 1.(b) Fit for  $M_{\mu\mu}$  distribution for Bin ID = 6.

**Figure 3.7:** Examples of the fit of signal (solid blue line) and background (dashed blue line) for  $M_{\mu\mu}$  distribution of a data sample in two bins (2011, CMSSW Release 4\_2\_X).

### 3.4 Fit strategy

Given the large number of free parameters to be determined by MuSclFit it is very important to define a good performing fit strategy. It could happen that the parameters converge towards non physically acceptable values or in the worst case the fit does not converge.

Taking into account that the corrections applied to the curvature are strictly correlated with the global deformations of the detector geometry, any parameter has a physical meaning. In order to make the fit strategy in MuSclFit more robust, a specific sequence for the fitting process is defined. The basic idea is to avoid the simultaneous fit of all the parameters. Since sets of parameters fitted in different steps are considered independent from each other, a non simultaneous fit of all the parameters represents an approximation but reduces significantly the computing time for the fit. The choice for this analysis is to perform the fit in different steps,

$$\text{Resolution} \implies \text{Scale} (p_0 \text{ fixed}) \implies \text{Scale} (p_0 \text{ fixed}) \implies \text{Resolution} \implies p_0$$

At first the 13 parameters of the resolution function are fitted, to estimate the resolution of the tracker before any correction on the scale of the momentum of muons is applied. This step, combined with the last one, is very important in evaluating the effect of the momentum correction on the resolution of muons and can detect a possible bad parametrization of the scale function. Indeed, if the scale function correctly takes into account the weak modes in the geometry of the tracker, in principle the resolution should not be degraded by the correction on the momentum of muons. The fit of the 21 parameters of the scale function is performed in two steps, the first finds the best value for the parameters and the second, starting from these values, refine them in case they were still too imprecise. Moreover the second step in the fit of the scale function helps in understanding if the fit is converging towards defined values of the parameters. The parameters of these two steps can be merged into a single set, see Appendix A for details. Then a fit on the resolution is performed again, allowing to know if the corrections on muons contributed to improve or degrade the resolution of the reconstructed muon. In the last step only the  $p_0$  parameter of the scale correction is fitted. In the following chapter the results of the muon calibration with MuSclFit are presented for some samples.

## Chapter 4

# Results of the Muon Calibration

In this chapter a detailed study on the performance of MuSclFit is presented. By reconstructing the  $Z$  before and after the calibration it is possible to quantify the impact of the correction computed by MuSclFit. The sets of the scale correction parameters found for the samples in 4\_2\_X and 5\_3\_X are listed in Table 4.1 and Table 4.2. The effects of the MuSclFit corrections are studied first by reconstructing the  $Z$  boson in different kinematical regions of the muons, then by comparing data and simulation samples processed with the same CMSSW release. In the last section of this chapter a study of the resolution on the curvature of the muons will be illustrated considering a sample of simulated muons. The effects on the resolution of the MuSclFit correction will be studied for the sample of simulated muons in 5\_3\_X. For this sample the list of the 26 parameters is reported in Table 4.3.

List of MuSclFit correction scale parameters for data samples at $\sqrt{s} = 7$ TeV		
Parameter	Data 4_2_X	Simulation 4_2_X
$p_0$	$-0.00121 \pm 0.00001$	$0.00017 \pm 0.00001$
$a_{1,1}$	$0.0014496 \pm 4.6 \cdot 10^{-6}$	$0.0011158 \pm 6.3 \cdot 10^{-6}$
$\varphi_{1,1}$	$1.0037 \pm 0.0029$	$-0.0083 \pm 0.0054$
$a_{2,1}$	$0.0005323 \pm 5.0 \cdot 10^{-6}$	$0.0009131 \pm 6.8 \cdot 10^{-6}$
$\varphi_{2,1}$	$1.3251 \pm 0.0077$	$-2.0000 \pm 0.0072$
$b_1$	$-0.00025 \pm 0.00018$	$7.5 \cdot 10^{-6} \pm 3 \cdot 10^{-7}$
$a_{1,2}$	$0.0003897 \pm 3.0 \cdot 10^{-6}$	$0.0002103 \pm 2.5 \cdot 10^{-6}$
$\varphi_{1,2}$	$0.9717 \pm 0.0086$	$-0.9432 \pm 0.012$
$b_2$	$-0.0004281 \pm 6.4 \cdot 10^{-6}$	$0.0001756 \pm 6.9 \cdot 10^{-6}$
$a_{1,3}$	$0.0001477 \pm 1.3 \cdot 10^{-6}$	$0.00018569 \pm 7 \cdot 10^{-7}$
$\varphi_{1,3}$	$-1.522 \pm 0.012$	$-1.774 \pm 0.0038$
$b_3$	$-1.98 \cdot 10^{-5} \pm 2.6 \cdot 10^{-6}$	$2.25 \cdot 10^{-6} \pm 9.1 \cdot 10^{-7}$
$a_{1,4}$	$7.48 \cdot 10^{-5} \pm 2.1 \cdot 10^{-6}$	$0.0003732 \pm 2.9 \cdot 10^{-6}$
$\varphi_{1,4}$	$1.293 \pm 0.021$	$-1.2390 \pm 0.0076$
$b_4$	$-0.0005414 \pm 4.7 \cdot 10^{-6}$	$8.10 \cdot 10^{-6} \pm 7.4 \cdot 10^{-7}$
$a_{1,5}$	$0.0009579 \pm 3.8 \cdot 10^{-6}$	$0.0008652 \pm 6.7 \cdot 10^{-6}$
$\varphi_{1,5}$	$1.5846 \pm 0.0049$	$-1.4006 \pm 0.0078$
$a_{2,5}$	$0.0005257 \pm 7.0 \cdot 10^{-6}$	$0.0008256 \pm 7.0 \cdot 10^{-6}$
$\varphi_{2,5}$	$-0.3300 \pm 0.011$	$2.7090 \pm 0.0080$
$b_5$	$-0.000757 \pm 1.7 \cdot 10^{-5}$	$-6.38 \cdot 10^{-5} \pm 3.4 \cdot 10^{-6}$
$\delta$	$4.85 \cdot 10^{-5} \pm 3.8 \cdot 10^{-6}$	$4.25 \cdot 10^{-5} \pm 4.2 \cdot 10^{-6}$

**Table 4.1:** Scale calibration parameters for samples at  $\sqrt{s} = 7$  TeV. By referring to Equation 3.8 the parameters  $\mathbf{a}_1$ ,  $\mathbf{a}_2$ ,  $\mathbf{b}$  and  $\delta$  are expressed in  $\text{GeV}^{-1}$ , the other parameters are dimensionless. The errors on the parameters represent the statistical error of the fit.

List of MuSclFit correction scale parameters for samples at $\sqrt{s} = 8$ TeV		
Parameter	Data 5_3_X	simulation 5_3_X
$p_0$	$-0.00077 \pm 0.00001$	$0.00038 \pm 0.00001$
$a_{1,1}$	$0.00054814 \pm 4.9 \cdot 10^{-7}$	$0.00027280 \pm 4.9 \cdot 10^{-7}$
$\varphi_{1,1}$	$1.1074 \pm 0.0020$	$0.1418 \pm 0.0026$
$a_{2,1}$	$0.00042828 \pm 4.6 \cdot 10^{-7}$	$0.00023103 \pm 4.6 \cdot 10^{-7}$
$\varphi_{2,1}$	$1.7703 \pm 0.0018$	$-1.7105 \pm 0.0022$
$b_1$	$-0.0001200 \pm 1.0 \cdot 10^{-6}$	$-3.0 \cdot 10^{-6} \pm 1.3 \cdot 10^{-6}$
$a_{1,2}$	$9.273 \cdot 10^{-5} \pm 2.4 \cdot 10^{-7}$	$1.413 \cdot 10^{-5} \pm 1.2 \cdot 10^{-7}$
$\varphi_{1,2}$	$0.5290 \pm 0.0021$	$-1.0402 \pm 0.0025$
$b_2$	$-0.00021218 \pm 6.6 \cdot 10^{-7}$	$3.730 \cdot 10^{-5} \pm 8.4 \cdot 10^{-7}$
$a_{1,3}$	$0.00020835 \pm 3.1 \cdot 10^{-7}$	$6.647 \cdot 10^{-5} \pm 2.5 \cdot 10^{-7}$
$\varphi_{1,3}$	$-1.3865 \pm 0.0016$	$-1.6473 \pm 0.0022$
$b_3$	$2.559 \cdot 10^{-5} \pm 5.1 \cdot 10^{-7}$	$-1.30 \cdot 10^{-6} \pm 6.2 \cdot 10^{-7}$
$a_{1,4}$	$1.646 \cdot 10^{-6} \pm 3.4e - 08$	$3.421 \cdot 10^{-5} \pm 1.9 \cdot 10^{-7}$
$\varphi_{1,4}$	$-0.6650 \pm 0.0021$	$-1.6841 \pm 0.0023$
$b_4$	$-0.00014906 \pm 6.7 \cdot 10^{-7}$	$1.31 \cdot 10^{-6} \pm 8.4 \cdot 10^{-7}$
$a_{1,5}$	$0.00038728 \pm 4.5 \cdot 10^{-7}$	$0.00018439 \pm 4.2 \cdot 10^{-7}$
$\varphi_{1,5}$	$2.3260 \pm 0.0014$	$-0.9479 \pm 0.0025$
$a_{2,5}$	$0.00023995 \pm 3.7 \cdot 10^{-7}$	$0.00012101 \pm 3.5 \cdot 10^{-7}$
$\varphi_{2,5}$	$-1.1663 \pm 0.0020$	$0.3860 \pm 0.0027$
$b_5$	$-0.0001845 \pm 1.0 \cdot 10^{-6}$	$-1.7 \cdot 10^{-6} \pm 1.3 \cdot 10^{-6}$
$\delta$	$4.3961 \cdot 10^{-5} \pm 9.8e - 08$	$4.661 \cdot 10^{-5} \pm 1.2 \cdot 10^{-7}$

**Table 4.2:** Scale calibration parameters for samples at  $\sqrt{s} = 7$  TeV. By referring to Equation 3.8 the parameters  $\mathbf{a}_1$ ,  $\mathbf{a}_2$ ,  $\mathbf{b}$  and  $\delta$  are expressed in  $\text{GeV}^{-1}$ , the other parameters are dimensionless. The errors on the parameters represent the statistical error of the fit.

---

**List of MuSclFit correction resolution parameters for simulation sample at  $\sqrt{s} = 8$  TeV**

---

Parameter	Before correction	After correction
$q_0$	$0.000210 \pm 1.2 \cdot 10^{-5}$	$0.000189 \pm 1.3 \cdot 10^{-5}$
$q_1$	$0.02554 \pm 0.00047$	$0.02501 \pm 0.00044$
$q_2$	$0.01491 \pm 0.00051$	$0.01552 \pm 0.00049$
$q_3$	$0.01094 \pm 0.00072$	$0.01161 \pm 0.00049$
$q_4$	$0.01167 \pm 0.00046$	$0.01212 \pm 0.00053$
$q_5$	$0.00787 \pm 0.00064$	$0.00851 \pm 0.00062$
$q_6$	$0.00304 \pm 0.00074$	$0.00372 \pm 0.00075$
$q_7$	$0.00324 \pm 0.00072$	$0.00389 \pm 0.00073$
$q_8$	$0.00818 \pm 0.00064$	$0.00885 \pm 0.00062$
$q_9$	$0.01082 \pm 0.00058$	$0.01124 \pm 0.00055$
$q_{10}$	$0.01113 \pm 0.00069$	$0.01185 \pm 0.00065$
$q_{11}$	$0.01528 \pm 0.00057$	$0.01572 \pm 0.00054$
$q_{12}$	$0.02631 \pm 0.00047$	$0.02686 \pm 0.00044$

---

**Table 4.3:** Scale calibration parameters for the simulation sample at  $\sqrt{s} = 8$  TeV. By referring to Equation 3.12  $q_0$  is expressed in  $\text{GeV}^{-1}$ , the other parameters are dimensionless. The errors on the parameters represent the statistical error of the fit.

## 4.1 Local effects of the corrections

In what follows a study of the effects of the MuSclFit correction in different kinematic regions of the muons is presented. The choice of the different intervals in which the  $Z$  boson is reconstructed is based on considerations about the number of events in each kinematic interval. The bins in which the reconstruction of the resonance is performed are listed below:

- $\eta_-$  : intervals in  $\eta$  for the negative muons are defined, while no restrictions are present in any other kinematic variable both for the negative and the positive muon. From  $\eta_- = -2.4$  to  $\eta_- = 2.4$  a total of 12 bins of the same width are defined, hence every bin covers 0.4 units in  $\eta$ .
- $\varphi_-$  : intervals in  $\varphi$  for the negative muons are defined, while no restrictions are present in any kinematic variable both for the negative and the positive muon. From  $\varphi_- = -\pi$  to  $\varphi_- = \pi$  a total of 16 bins of the same width are defined, hence every bin covers  $\pi/16$  units in  $\varphi$ .
- $\eta$  and  $\varphi$  : intervals in  $\eta$  and  $\varphi$  for the positive muons are defined, while no restrictions are present in any other kinematic variable both for the negative and the positive muon. Twenty bins are defined in  $\eta$  from  $\eta = -2.4$  to  $\eta = 2.4$  and 16 in  $\varphi$  from  $\varphi = -\pi$  to  $\varphi = \pi$ , and the total number of bins is 320.

The same kind of study is performed in bins of the positive muon too.

### 4.1.1 Calibration for samples at $\sqrt{s} = 7$ TeV

In what follows the results of the MuSclFit correction on muons for the samples of data and simulation at  $\sqrt{s} = 7$  TeV processed in CMSSW release 4\_2\_X are presented. In order to appreciate the changes introduced by the MuSclFit correction in the  $Z$  reconstruction in different kinematic bins, in every plot the situation before and after the corrections are compared. From now on the function used to perform the fits is the one described in Equation 2.3. The plots for the sample of data are represented in Figure 4.1. Here the improvement made by the correction is extremely significant. The response of the detector to the reconstruction of the  $Z$  peak has been made quite uniform in every kinematic bin examined. In particular in Figure 4.1b, while before the corrections the difference between the reconstruction of  $M_Z$  in the first and last  $\eta$  bins was about 1.1 GeV, after the corrections it is reduced to 0.2 GeV. The same happens for the projections along the  $\varphi$  angle of each muon. Moreover it is important to notice that is visible a modulation of  $M_Z$ , both in function of  $\varphi_-$  and  $\varphi_+$ . The sample

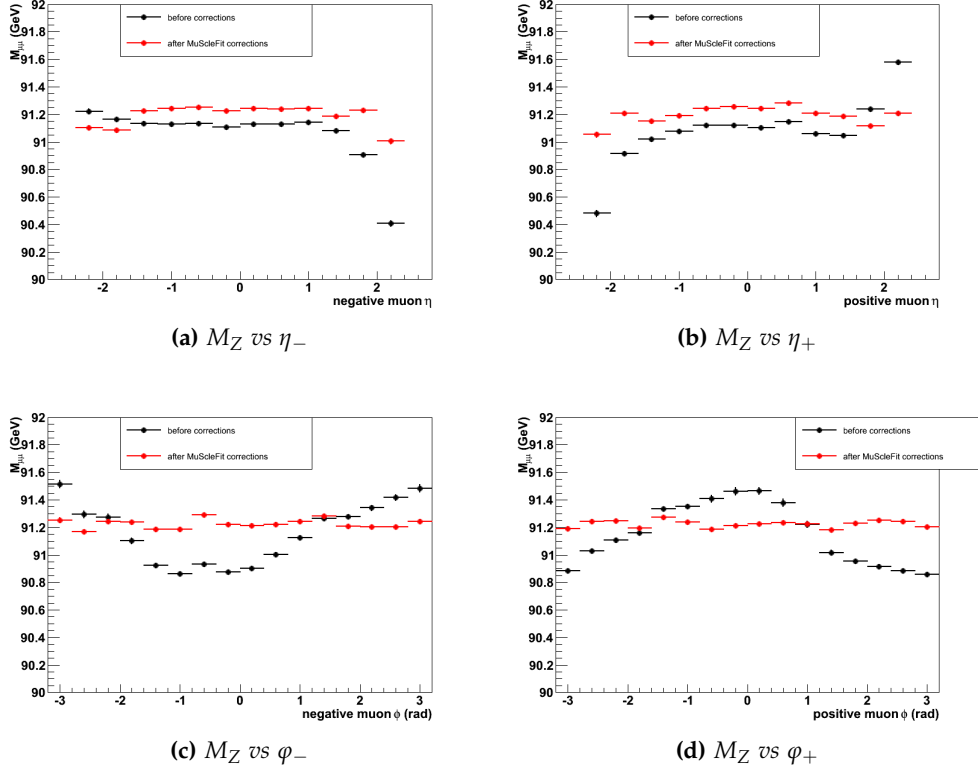


**Figure 4.1:** Mass of the Z reconstructed from the dimuon invariant mass in different regions of the tracker before (black) and after (red) the corrections for a data sample at  $\sqrt{s} = 7 \text{ TeV}$

of data at  $\sqrt{s} = 7 \text{ TeV}$  is not the only one in which this modulation is visible, and possible sources that can generate such modulation are examined in Section 4.4. Another way to check the behaviour of the corrections is to show how  $M_Z$  is reconstructed in  $(\eta, \varphi)$  maps (see Figure 4.2). In this kind of representation the nominal value of the mass, i.e.  $m_0$ , corresponds to the green color. A red bin indicates that the reconstructed mass has an higher value with respect to  $m_0$ , conversely the blue bins are associated with a lower value. Although these maps cannot provide quantitative informations about the value of  $M_Z$  in each bin, they are a good tool to evaluate qualitatively the behaviour of the correction. Also in this case the correction has significantly flattened the reconstructed value of  $M_Z$ , e.g. Figure 4.2b is much more uniform in color with respect to 4.2a. A closer inspection of the map before the correction shows that the modulation in  $M_Z$  when reconstructed only along  $\eta_+$  (see Figure 4.1d) comes from the region  $|\eta_+| < 1.5$ . The reason is that in the samples considered the most populated bin is the central one, and when every value of  $\eta$  is considered,



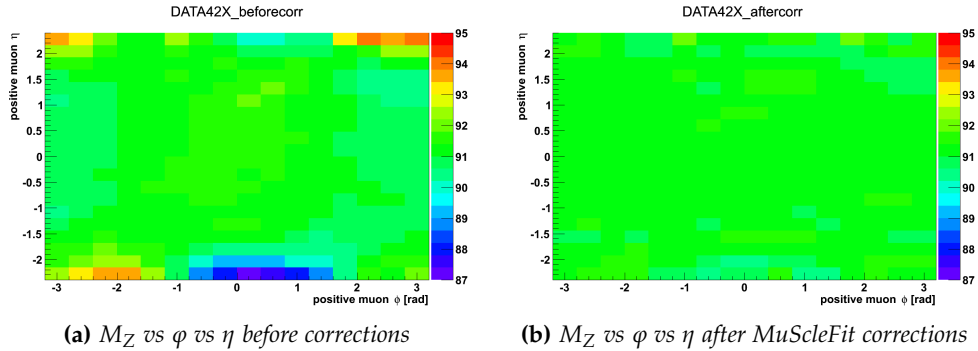


**Figure 4.2:** Mass of the Z reconstructed from the dimuon invariant mass in different regions of the tracker before and after the corrections

such as in Figure 4.1d, its weight is much sizable with respect to the other  $\eta$ -bins, and its modulations in the reconstructed  $M_Z$  prevails. In order to verify the last assertion the number of events per  $\eta$ -bin is plotted in Figure 4.3a: here the first and last  $\eta$ -bins have the events of the central bins. For

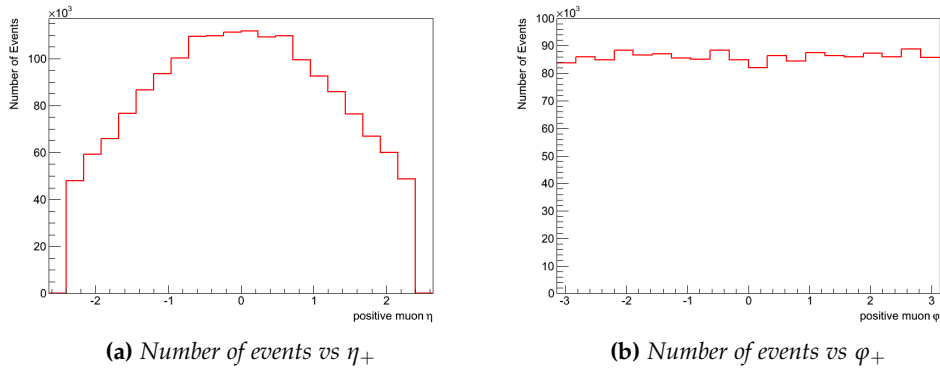


**Figure 4.3:** Distribution of events as a function of  $\eta_+$  or  $\varphi_+$  for the sample in data at  $\sqrt{s} = 7$  TeV.

completeness the distribution of events in the  $\varphi_+$  variable is shown too (Figure 4.3b), and, as expected is, within the statistical precision, uniform. Another observable that is possible to examine is the resolution on the reconstructed Z. In principle the resolution could be significantly affected by the correction on muons. In what follows  $\sigma$  is the standard deviation of the gaussian core of the Crystal Ball of the fitting function and it represents the estimated resolution on the reconstruction of Z. To extract the resolution in different kinematic regions,  $\sigma$  is plotted against  $\eta_+$  in Figure 4.4. The effect of the MuSclFit correction on the resolution is beneficial everywhere, in the barrel region the correction decreases the parameter  $\sigma$

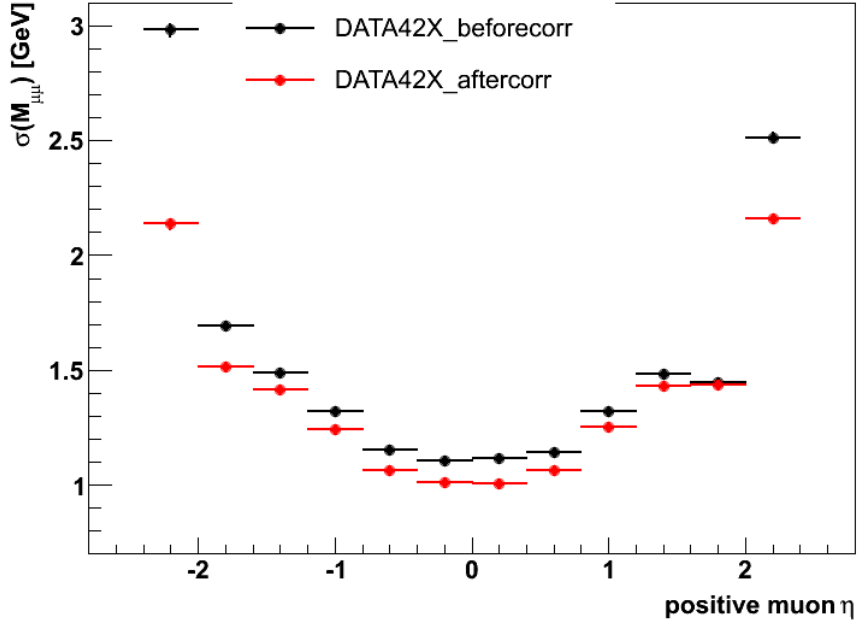


**Figure 4.4:** Resolution on the mass of the Z as a function of  $\eta_+$  for the sample in data at  $\sqrt{s} = 7$  TeV.

of about 0.1 GeV and even more in the endcap region decreases up to 0.3 GeV.

The results obtained by correcting muons in the sample at  $\sqrt{s} = 7$  TeV of simulated muons (CMSSW release 4\_2\_X) are shown in Figures 4.5, 4.6 and 4.7. In general the same considerations done for the sample in data at  $\sqrt{s} = 7$  TeV apply here. After the correction the bias on the reconstruction of  $M_Z$  is significantly recovered in every kinematic region examined, and the fitted resolution on the Z reconstruction is improved. The modulation observed in function of  $\varphi_-$  and  $\varphi_+$  is recovered by the correction.

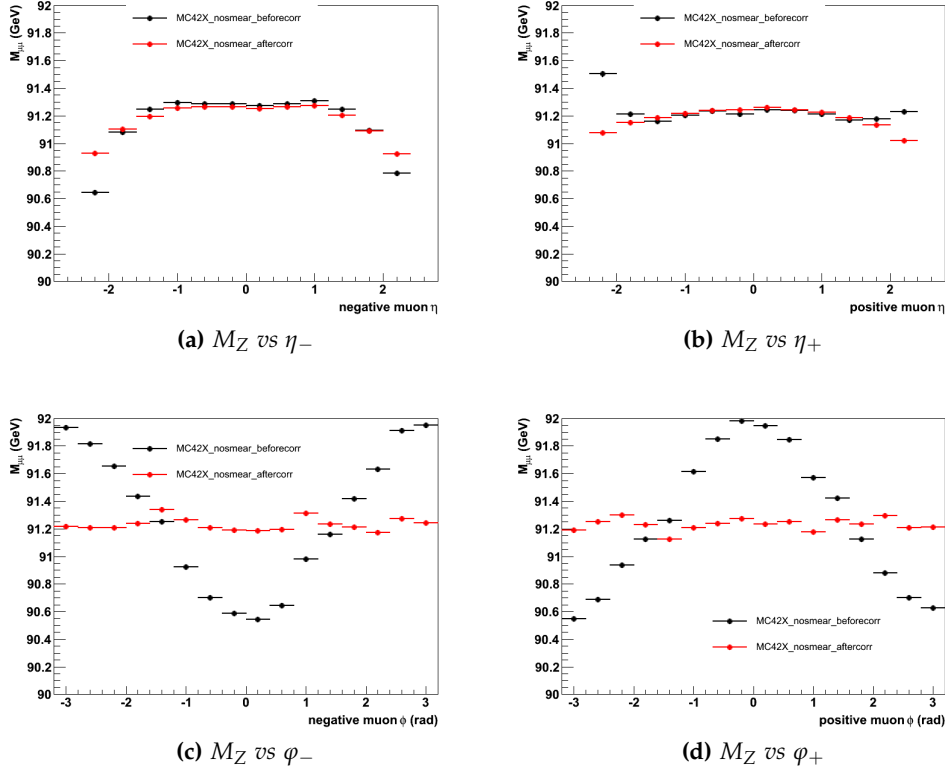


**Figure 4.5:** Mass of the Z reconstructed from the dimuon invariant mass in different regions of the tracker before (black) and after (red) the corrections for a sample of simulated muons at  $\sqrt{s} = 7$  TeV.

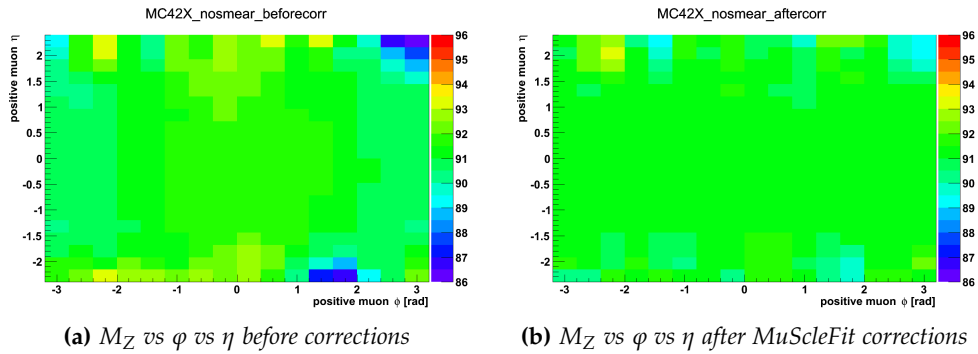


**Figure 4.6:** Mass of the Z reconstructed from the dimuon invariant mass in different regions of the tracker before and after the corrections for the sample of simulated muons at  $\sqrt{s} = 7$  TeV.

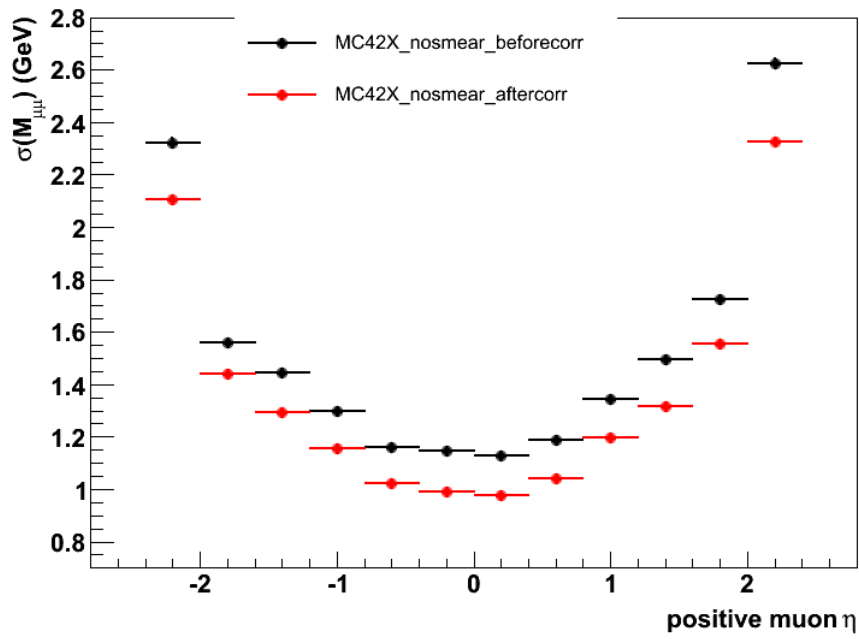


**Figure 4.7:** Resolution on the mass of the Z as a function of  $\eta_+$  for the sample of simulated muons at  $\sqrt{s} = 7$  TeV.

### 4.1.2 Calibration for samples at $\sqrt{s} = 8$ TeV

In the following the results of the correction for the samples of data and simulation at  $\sqrt{s} = 8$  TeV are presented, with both samples processed in CMSSW release 5\_3\_X. The results for these samples are very similar to those previously described: after the correction the reconstruction of  $M_Z$  is made quite uniform in every considered kinematic bin and the resolution is improved. Also here the modulation of  $M_Z$  in function of  $\varphi_-$  and  $\varphi_+$  is significantly recovered. Although the general behaviour of the

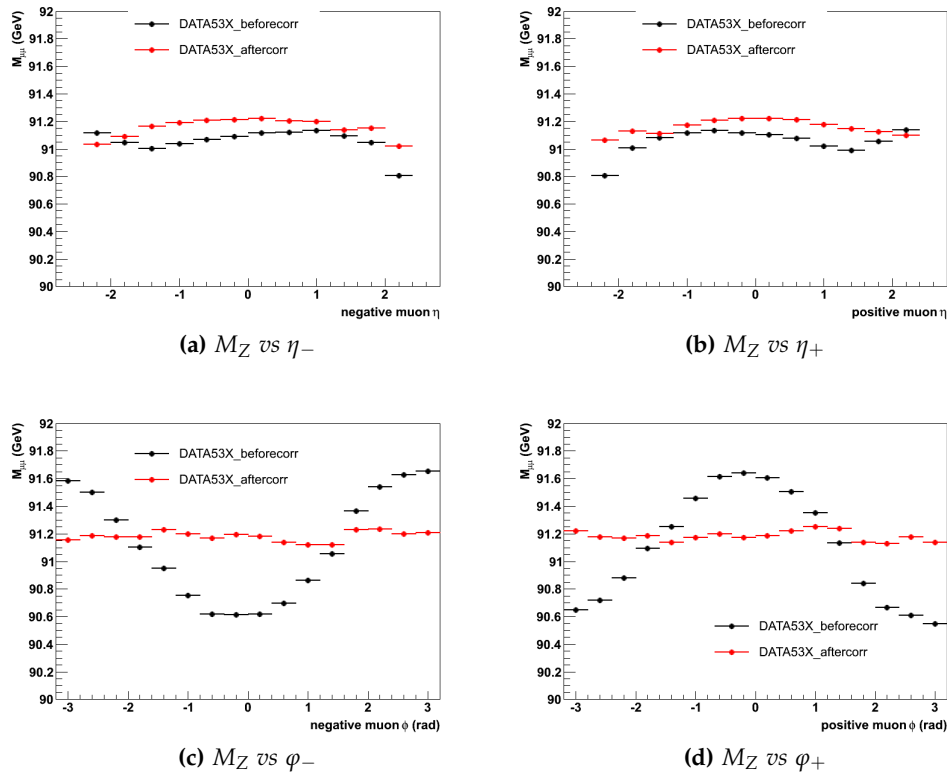


**Figure 4.8:** Mass of the Z reconstructed from the dimuon invariant mass in different regions of the tracker before (black) and after (red) the corrections for the sample in data at  $\sqrt{s} = 8$  TeV.

correction is the same as described for the samples at  $\sqrt{s} = 7$  TeV, there are still few differences that can be highlighted. Consider the case before the correction in Figure 4.8a and Figure 4.8b, it is possible to notice that in general the bias in  $M_Z$  is slightly reduced with respect to the same plots of the samples at  $\sqrt{s} = 7$  TeV. The CMSSW release 5\_3\_X represents a newer data processing environment with respect to the 4\_2\_X. Between the two releases passed few months in which the alignment and calibration strate-

gies and algorithms were continuously improved. It is clear then why the biases in the samples in 5\_3\_X are less prominent with respect to those in 4\_2\_X.

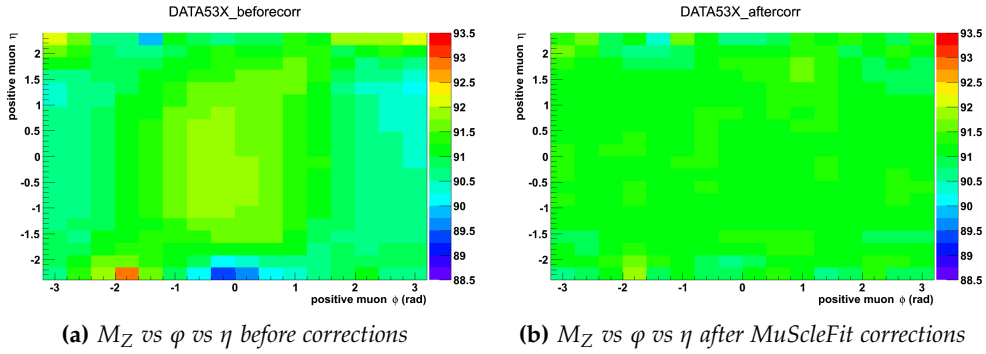


**Figure 4.9:** Mass of the Z reconstructed from the dimuon invariant mass in different regions of the tracker before and after the corrections for the sample in data at  $\sqrt{s} = 8$  TeV.

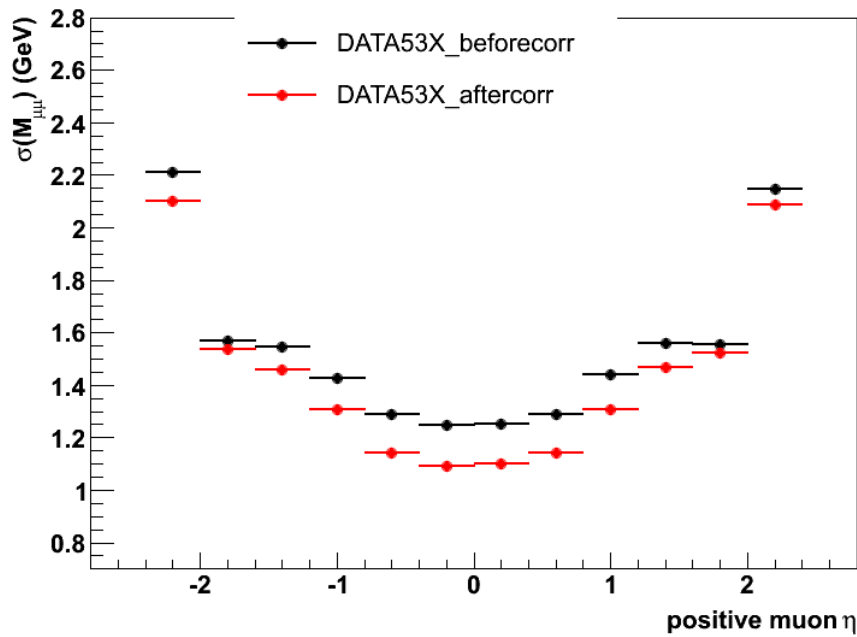


**Figure 4.10:** Resolution on the mass of the Z as a function of  $\eta_+$  for the sample in data at  $\sqrt{s} = 8$  TeV.

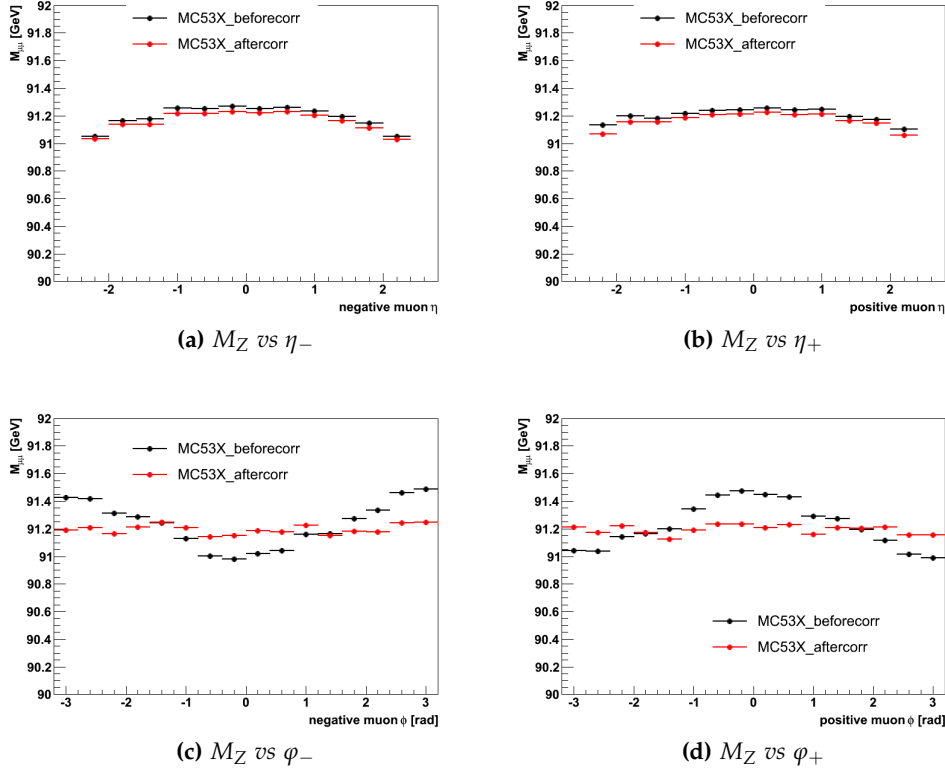


**Figure 4.11:** Mass of the Z reconstructed from the dimuon invariant mass in different regions of the tracker before (black) and after (red) the corrections for the sample of simulated muons at  $\sqrt{s} = 8$  TeV.

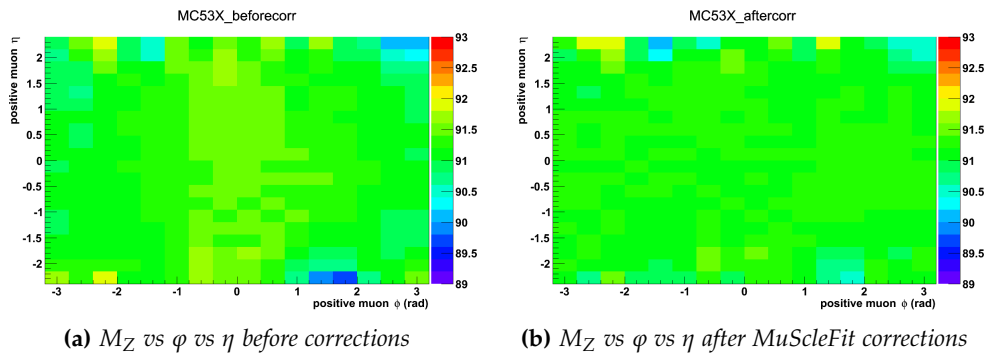


**Figure 4.12:** Mass of the Z reconstructed from the dimuon invariant mass in different regions of the tracker before and after the correction for the sample of simulated muons at  $\sqrt{s} = 8$  TeV.

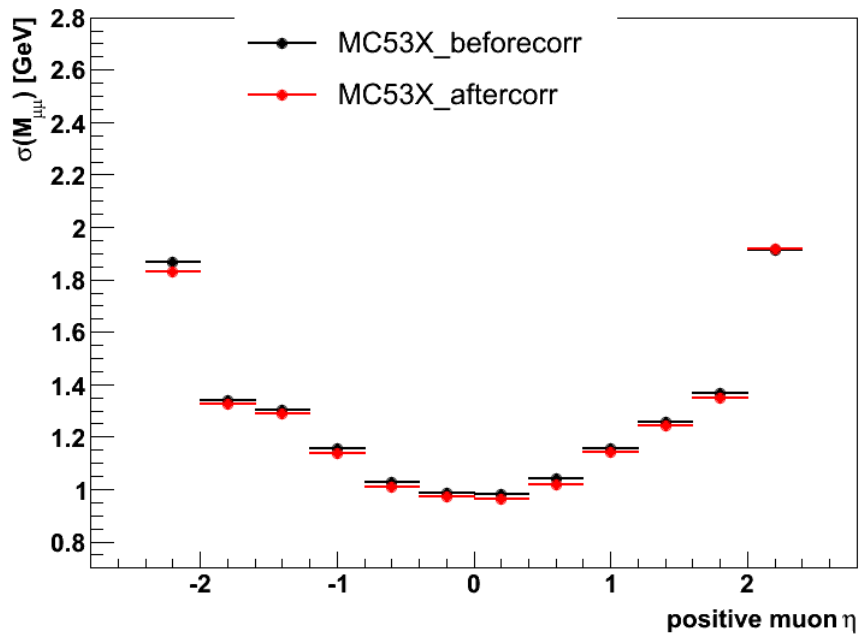


**Figure 4.13:** Resolution on the mass of the Z as a function of  $\eta_+$  for the sample of simulated muons at  $\sqrt{s} = 8$  TeV.



## 4.2 Extra smearing on simulated muons

In CMS most physics analyses make use of both real collision and simulated muons, with the collected data directly compared to a simulation. Hence it is clear that physics objects like muons need to have equal characteristics between data and simulation. Despite simulated muons are produced as similar as possible to the true muons, due to the complexity of the detector and the fact that the material map of CMS considered for the simulations has a limited granularity, not always the characteristics of the simulated muons match perfectly the characteristics of real muons. An example could be the resolution of the detector: by referring to Figure 4.4 and Figure 4.7 it is possible to appreciate a slight difference between the value of  $\sigma$  between data and MonteCarlo even after the correction. The resolution of the simulated events in every region of  $\eta_+$  is better than the resolution of the data events. After the momentum scale calibration, an extra step called *smearing* is performed on simulated muons. The extra smearing procedure consists in degrading the  $p_T$  of the tracks of the simulated muons until the resolution on the measurement of their momentum (or curvature) matches the resolution on the measurement of the momentum of real muons.

By denoting with  $k'$  the curvature of the muon after the extra smearing procedure and by identifying with  $j$  the bins in  $\eta$  of the positive muon, the relation between the new and the original curvature can be written as:

$$\kappa' = \kappa + |\kappa| \cdot g(\mu, \sigma_j) \quad (4.1)$$

Here  $g(\mu, \sigma_j)$  is a random gaussian number, with mean  $\mu$  and standard deviation  $\sigma_j$ . While it is always  $\mu = 0$ , the value of  $\sigma_j$  is different in each  $\eta$ -bin considered. The physical meaning of Equation 4.1 is that the value of the curvature of the muon is shaken randomly around its original value  $\kappa$  according to a gaussian distribution of standard deviation  $\sigma_j$  and mean 0. The recipe used to parametrize  $\sigma_j$  in each bin is:

$$\sigma_j = \gamma \frac{\sqrt{\sigma_{j;data}^2 - \sigma_{j;MC}^2}}{1/\kappa} \quad (4.2)$$

Here  $\sigma_{j;data}$  and  $\sigma_{j;MC}$  are the values of the fitted resolution of the muons in the  $\eta$ -bin  $j$ -th for data and MonteCarlo samples, and  $\gamma$  is an empirical factor that is possible to tune in order to optimize the matching between data and simulation. In this analysis the extent of  $\sigma_{j;data} - \sigma_{j;MC}$  will be between 0 GeV and 0.3 GeV, and  $\gamma$  between 0.80 and 1. In what follows the application of a smearing will be discussed for every pair of data and simulation samples processed with the same CMSSW release.

#### 4.2.1 Smearing on the sample at $\sqrt{s} = 7$ TeV

By taking into account the correction shown in Figure 4.4 and Figure 4.7 and applying the smearing process to the muons in the simulation sample, it is possible to see the effects of the smearing on the measured resolution of the Z. This is shown in Figure 4.14: in every  $\eta$ -bin the effect of the smearing is clear with the matching between data and simulation greatly improved. The value of the tuning parameter used here is  $\gamma = 0.80$ . While in the worst cases, i.e. the first and last bin, the difference between

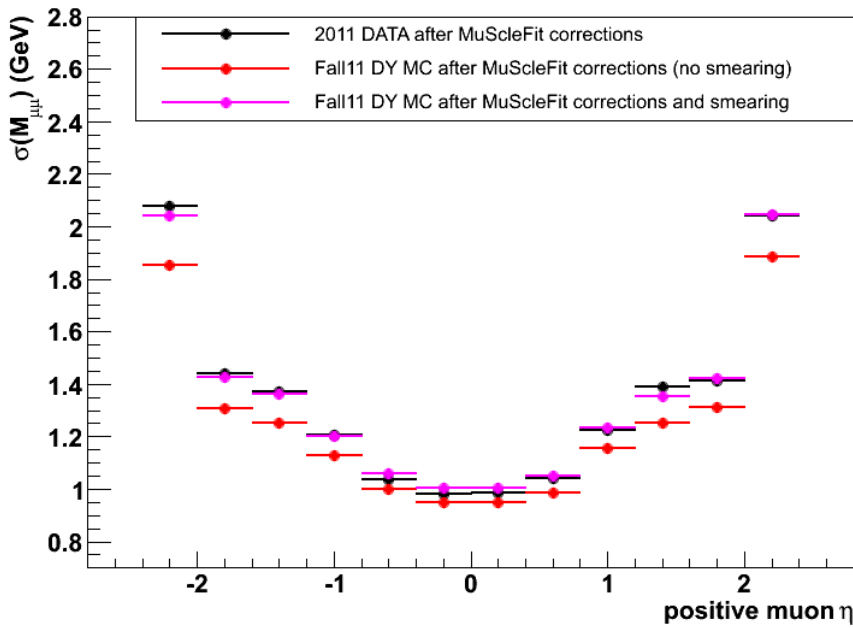


**Figure 4.14:** Resolution on the mass of the Z as a function of  $\eta_+$  for the corrected muons in the sample at  $\sqrt{s} = 7$  TeV before and after the extra-smearing process, and comparison with the corrected muons of sample in data at  $\sqrt{s} = 7$  TeV.

the fitted resolution on data and simulation before the correction is about 0.2 GeV, after the smearing that difference appears reduced to about 0.05 GeV.

#### 4.2.2 Smearing the sample at $\sqrt{s} = 8$ TeV

By proceeding in a similar way to the previous case the results of the resolution after the MuSclFit correction are taken into account for data at  $\sqrt{s} = 8$  TeV (Figure 4.10) and simulation at  $\sqrt{s} = 8$  TeV (Figure 4.13) samples. The effect of the extra-smearing process on the muons of the simulation sample is shown in Figure 4.15. The value of the tuning parameter

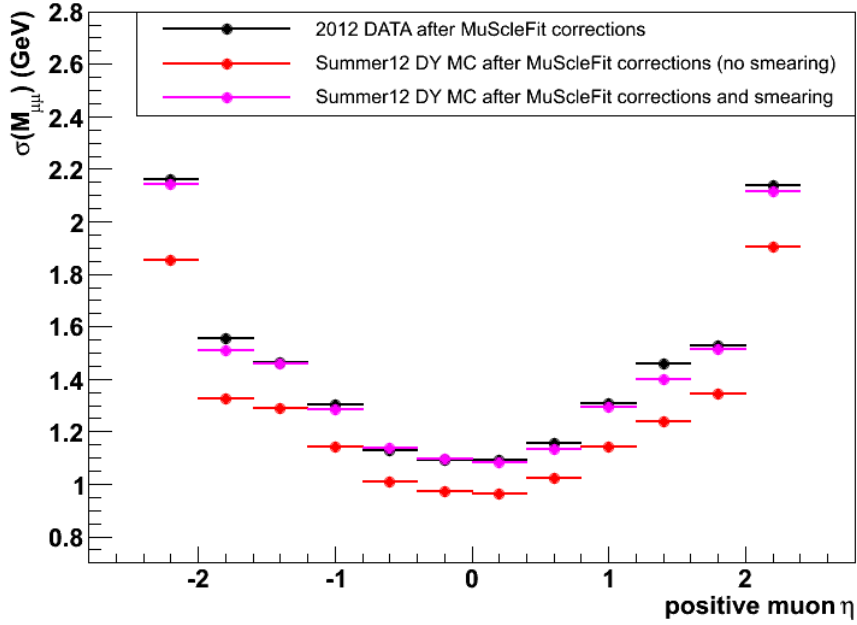


**Figure 4.15:** Resolution on the mass of the Z as a function of  $\eta_+$  for the corrected muons in sample at  $\sqrt{s} = 8$  TeV before and after the extra-smearing process, and comparison with the corrected muons of sample in data at  $\sqrt{s} = 8$  TeV.

used in this case is  $\gamma = 0.85$ . Here the situation is similar to the previous case: after the smearing the difference between the fitted resolution on data and simulation is lower than 0.05 GeV.

### 4.3 Global effects of the corrections

After applying the smearing on the simulated muons it is interesting to check the effects of the corrections on the whole collection of muons for each sample. While the calibration makes the response of the detector to a  $Z$  uniform in different kinematic regions, the goal of the smearing is to improve the matching of the resolution between data and the simulation. Therefore to check the effects of the correction and smearing on the reconstruction of  $Z$ , samples of data and simulation processed within the same CMSSW release are compared.

#### 4.3.1 Results at $\sqrt{s} = 7$ TeV

Referring to the samples at  $\sqrt{s} = 7$  TeV, it is possible to show the distribution of the dimuon invariant mass before having applied any correction. By performing a fit with the function described in Equation 2.3 it is possible to subtract the background. Since the fit statistical errors on the determination of  $f_{sig}$  and  $\lambda$  are negligible with respect to the values of the parameters they are not taken into account in the background subtraction procedure. Figure 4.16 shows the distribution of the invariant mass of the dimuon in the region  $[75, 105]$  GeV, where both distributions have been rescaled such as their integral in the range  $[75, 105]$  GeV is equal to 1. The ratio between distributions emphasizes the differences between the samples, as in the situation in which data and simulation match perfectly their ratio should be equal to unity everywhere within the stochastic fluctuations. In the case presented here neither the values of the peaks nor the widths match. To quantify these differences, in Table 4.4 are listed the results of the fit before and after the correction. The errors refer to the statistical errors of the fit. The difference between the fitted peak values

Global fit before the correction on muons for samples at $\sqrt{s} = 7$ TeV			
Sample	Status	Mass [GeV]	Sigma [GeV]
DATA 4_2_X	Before correction	$91.109 \pm 0.004$	$1.3779 \pm 0.005$
MC 4_2_X	Before correction	$91.240 \pm 0.002$	$1.3878 \pm 0.003$
DATA 4_2_X	After correction	$91.217 \pm 0.004$	$1.284 \pm 0.004$
MC 4_2_X	After correction	$91.224 \pm 0.003$	$1.270 \pm 0.003$

**Table 4.4:** Fit results for the whole muon collection of the samples at  $\sqrt{s} = 7$  TeV before and after the correction.

before the correction is 1% and the resolution on data is about 10 MeV better in the simulation. These values are the basis for a comparison with

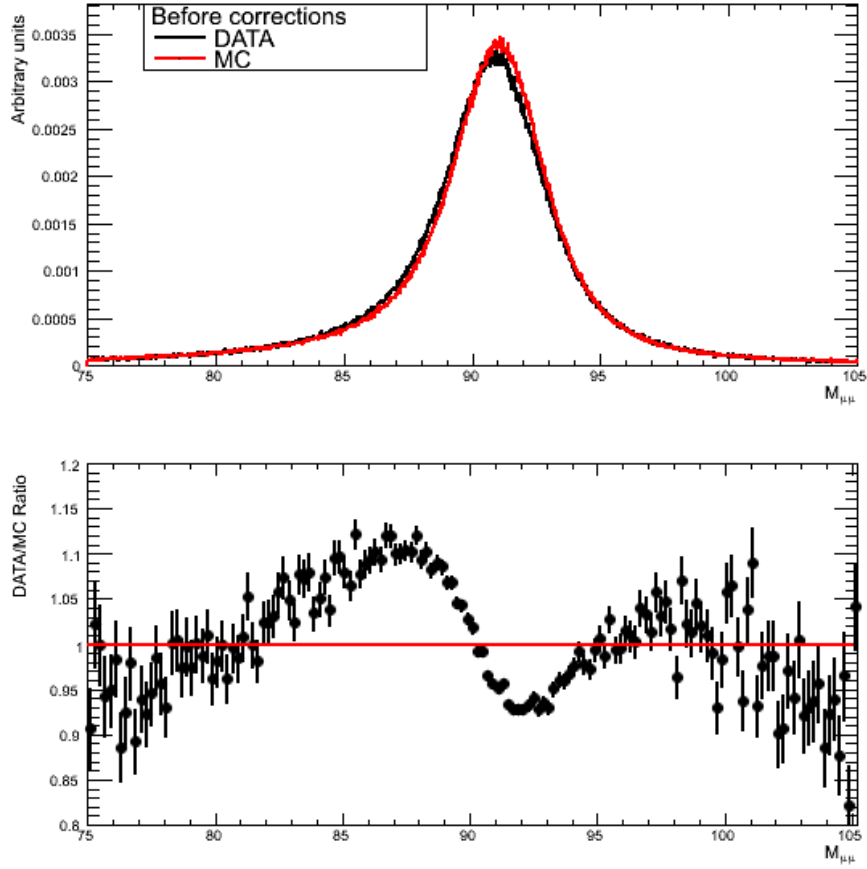


**Figure 4.16:** Top: dimuon invariant mass reconstructed in the region  $[75, 105]$  GeV for both data (black) and simulation (red) at  $\sqrt{s} = 7$  TeV before the correction, the error bars are proportional to the square root of number of events in each bin. Bottom: ratio between the plots of data and simulation, errors, from the plots at the top of the figure, are correctly propagated here.

the corrected muons. By referring to the reference samples, the comparison between data and simulation after the MuSclFit correction is shown in Figure 4.17. Here in both samples the background has been subtracted and the histograms normalized to 1 in the range  $[75, 105]$  GeV. It is clear that after the correction the differences between data and simulation are significantly reduced. Given that the difference between the fitted peak values is now  $10^{-4}$  and that the good matching between the resolutions is preserved, it is possible to say that the impact of the MuSclFit correction is beneficial.

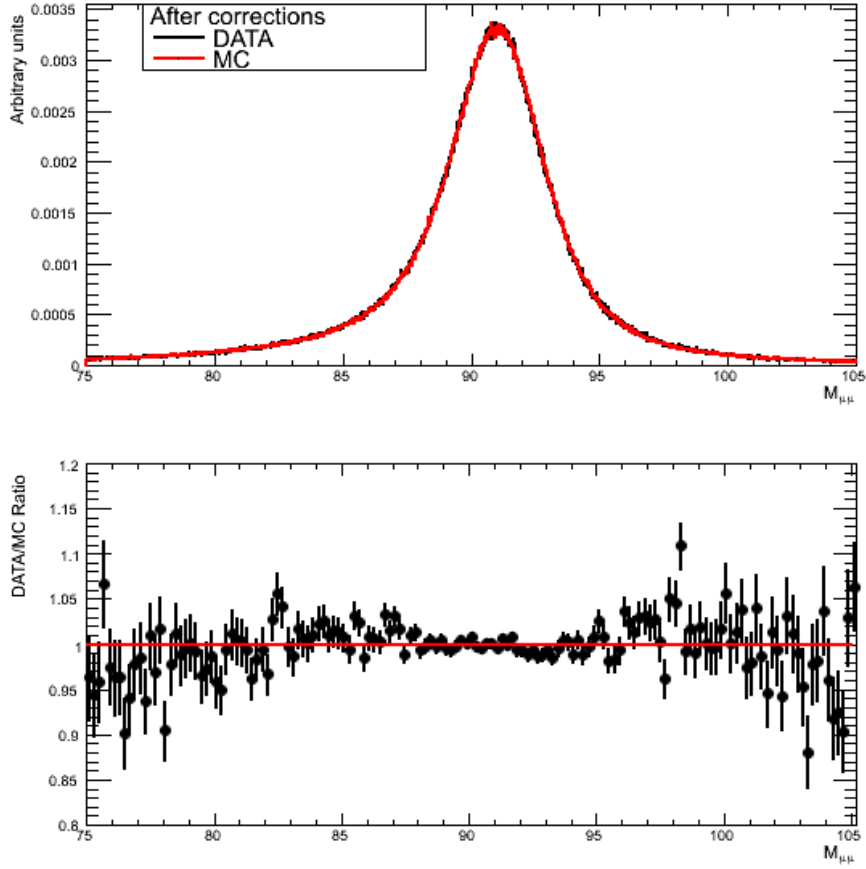


**Figure 4.17:** Top: dimuon invariant mass reconstructed in the region  $[75, 105]$  GeV for both data (black) and simulation (red) at  $\sqrt{s} = 7$  TeV after the correction, the error bars are proportional to the square root of number of events in each bin. Bottom: ratio between the plots of data and simulation, errors, from the plots at the top of the figure, are correctly propagated here.

#### 4.3.2 Results at $\sqrt{s} = 8$ TeV

Similarly to the global analysis on samples at  $\sqrt{s} = 7$  TeV also the samples at  $\sqrt{s} = 8$  TeV can be investigated. By taking into account the data and simulation samples for 2012 listed in Table 3.1 it is possible to plot their distribution of invariant mass normalized to 1 in the interval  $[75, 105]$  GeV and with subtracted background. Also here the fit statistical errors on the determination of  $f_{sig}$  and  $\lambda$  are negligible. The cases before and after the correction are plotted respectively in Figure 4.18 and in Figure 4.19. Here the situation before the correction is worse with respect to that one shown for the samples at  $\sqrt{s} = 7$  TeV, neither the peak value nor the resolution matches. A quantitative estimation on the differences

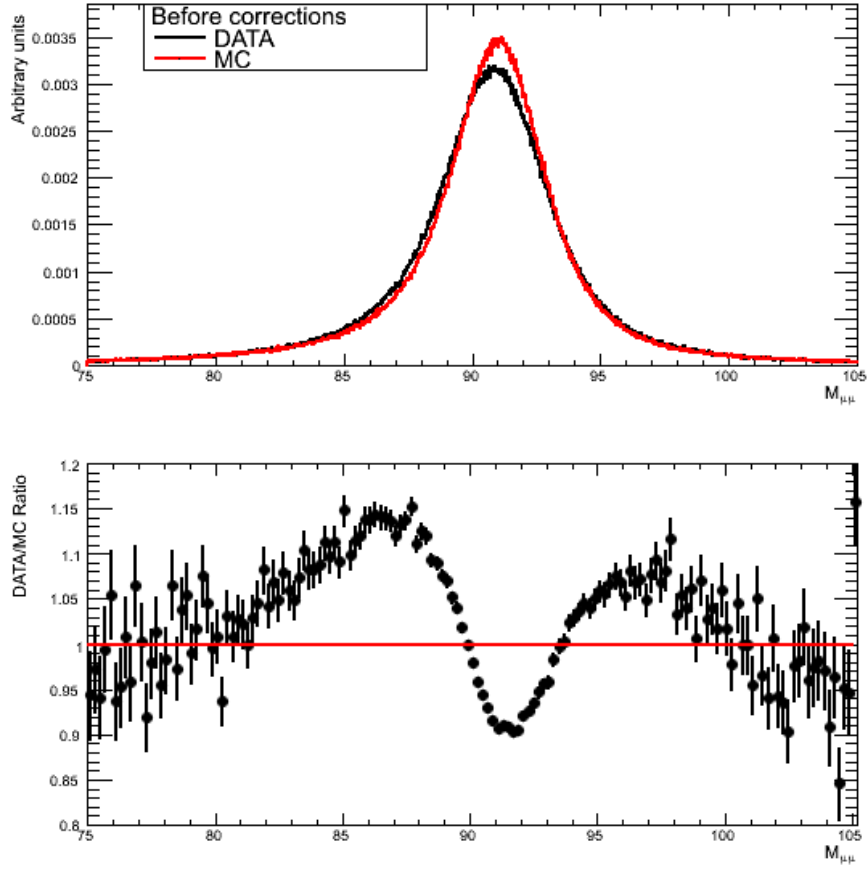


**Figure 4.18:** Top: dimuon invariant mass reconstructed in the region  $[75, 105]$  GeV for both data (black) and simulation (red) at  $\sqrt{s} = 8$  TeV after the correction, the error bars are proportional to the square root of number of events in each bin. Bottom: ratio between the plots of data and simulation, errors, from the plots at the top of the figure, are correctly propagated here.

between data and simulation before and after the correction comes from the fit and is plotted in Table 4.5. The fit function is the same used for the samples at  $\sqrt{s} = 7$  TeV. While before the corrections the matching between the fitted value of the peak in data and MC samples is about  $2\%m_0$ , after the MuSclFit corrections it is improved up to  $10^{-4}$ . An improvement is also seen within the resolution parametrization.

In order to have an overview on the effects of the MuSclFit correction on the global reconstruction of Z it is possible to gather all the fitted values of peak and resolution (Table 4.6. The errors refer to the statistical errors of the fit.

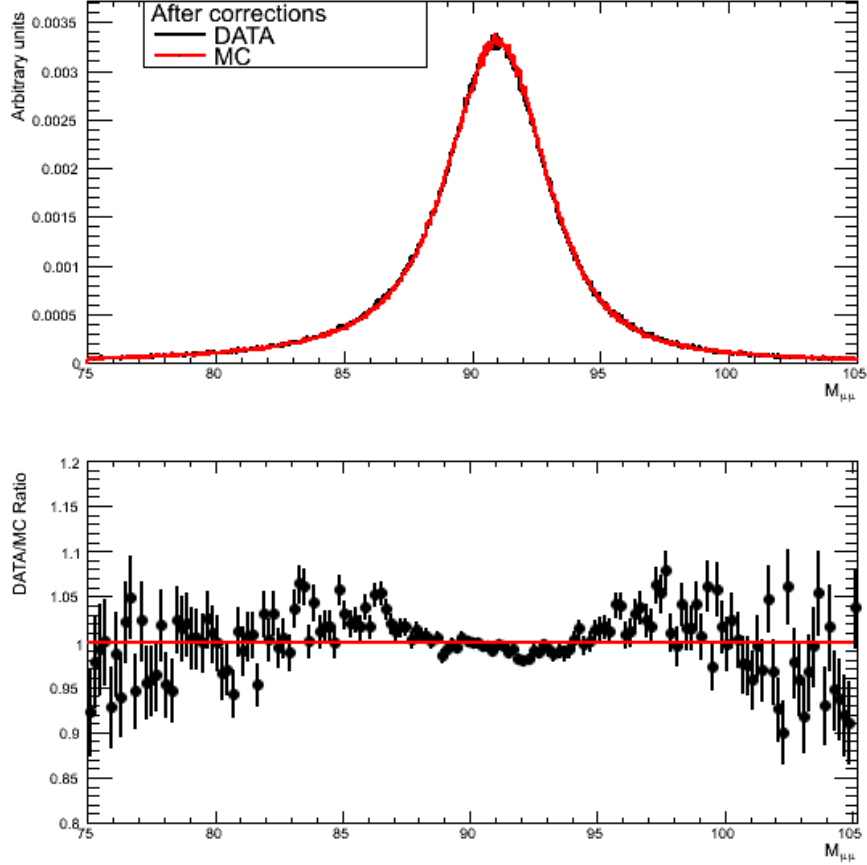


**Figure 4.19:** Top: dimuon invariant mass reconstructed in the region [75, 105] GeV for both data (black) and simulation (red) at  $\sqrt{s} = 8$  TeV after the correction, the error bars are proportional to the square root of number of events in each bin. Bottom: ratio between the plots of data and simulation, errors, from the plots at the top of the figure, are correctly propagated here.

---

**Global fit before the correction on muons for samples at  $\sqrt{s} = 8$  TeV**

---

Sample	Status	Mass [GeV]	Sigma [GeV]
DATA 5_3_X	Before correction	$91.078 \pm 0.002$	$1.454 \pm 0.002$
MC 5_3_X	Before correction	$91.226 \pm 0.003$	$1.191 \pm 0.003$
DATA 5_3_X	After correction	$91.184 \pm 0.003$	$1.300 \pm 0.003$
MC 5_3_X	After correction	$91.192 \pm 0.003$	$1.291 \pm 0.002$

---

**Table 4.5:** Fit results for the whole muon collection of the samples at  $\sqrt{s} = 8$  TeV before and after the corrections



<b>Improvements of the MuscleFit corrections on samples at <math>\sqrt{s} = 7</math> TeV and <math>\sqrt{s} = 8</math> TeV</b>		
Sample	Mass matching	Sigma improvement on data [MeV]
data vs simulation at $\sqrt{s} = 7$ TeV	1‰ $\rightarrow 10^{-4}$	$\approx 100$
data vs simulation at $\sqrt{s} = 8$ TeV	2‰ $\rightarrow 10^{-4}$	$\approx 150$

**Table 4.6:** Summary table with the global improvements in the data-simulation matching after the MuSclFit corrections and smearing.

## 4.4 Weak modes in the barrel

By considering how the mass is reconstructed as a function of  $\varphi_-$  or  $\varphi_+$ , it is possible to notice a sinusoidal modulation on the value of  $M_z$ . The origin of this modulation can be attributed to the presence of weak modes in the barrel region of the tracker. To investigate if a weak mode with a certain topology is able to produce such a modulation it is possible to set up a toy model of the reconstruction of a track in the barrel. The considered coordinate reference system of the simulation is the same defined in Chapter 1 for CMS. We consider a simplified layout with only two layers of the barrel which are built in the transverse plane (i.e. the plane  $x$ - $y$ ). The simulated tracks of the muons originate in  $(x = 0, y = 0)$  and are propagated through the layers where they leave a signal. The first layer has a radius of 50 cm, the second of 100 cm and, in the initial setup, are centered both in  $(0, 0)$   $\mu\text{m}$ . A magnetic field perpendicular to the transverse plane and with an intensity of 3.8 T is simulated too, but no multiple scattering or energy loss effects are considered.

It is possible to study the effect of translating progressively the center of the layers along the  $y$ -axis. This deformation of the geometry is called *sagitta* in the weak mode jargon. Figure 4.20 shows the situation: the introduced translation is linearly dependent on the radius of the layer, such that if the internal layer is translated by  $\epsilon$   $\mu\text{m}$ , the second is translated by  $2\epsilon$   $\mu\text{m}$ . A realistic choice would be introduce a translation of 50  $\mu\text{m}$  for the internal layer and of 100  $\mu\text{m}$  for the external layer. Then muons with  $p_T = 40$  GeV which is the most probable value for the muons from  $Z$ , and with starting directions from  $\varphi = 0$  to  $\varphi = 2\pi$  are generated. Since energy loss and multiple scattering of the muons are not taken into account the tracks are circles. A fit of the curvature is performed for each track by considering the two hits on the translated layers and the point where the track is originated, that is  $(0, 0)$ . By denoting with  $\kappa_{gen}$  the generated curvature of the muons ( $1/40$   $\text{GeV}^{-1}$ ) it is possible to compare it with  $\kappa_{reco}$  in case the translation of the layers is introduced. The difference  $\kappa_{gen} - \kappa_{reco}$  as a function of the generated  $\varphi$  of the track is shown in Figure 4.21. Here, keeping in mind that the translation on layers is always in the direction of  $\varphi = \pi/2$ , it is possible to see the effect of the translation on the reconstructed curvature for different  $\varphi$  of the tracks. The highest values for  $|\kappa_{gen} - \kappa_{reco}|$  are when the shift is perpendicular to the direction of the track. In what follows the highest value of  $|\kappa_{gen} - \kappa_{reco}|$ , that is in the considered example when  $\varphi = 0$  or  $\varphi = \pi$ , is denoted with  $\Delta_k$ . The plot in Figure 4.21 could be fitted with a sinusoidal function of  $\varphi$ , similarity to the parametrization of scale correction used in MuSclFit. The parameter  $a_{1,3}$  in Equation 3.8 represents the amplitude of an harmonic function of  $\varphi$  for the correction of the curvature of the muon. By taking into account every sample examined, both at  $\sqrt{s} = 7$  TeV and  $\sqrt{s} = 8$  TeV, it is possible

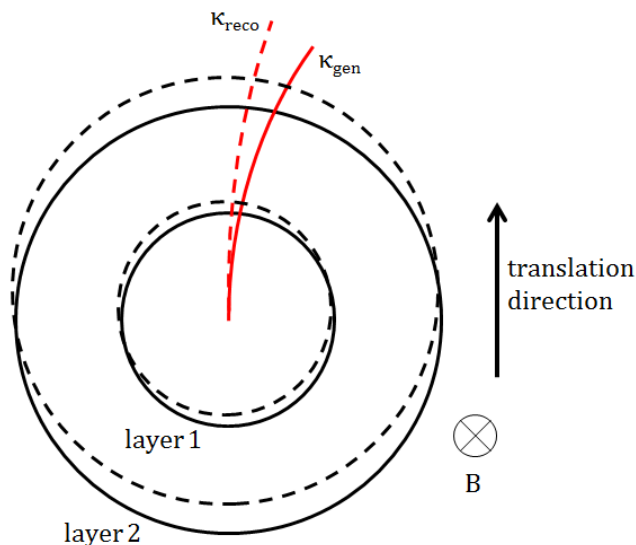


**Figure 4.20:** Starting setup of the detector: two circular layers both centered in  $(0, 0)$   $\mu\text{m}$  (solid black line) and the simulated track with generated curvature  $\kappa_{\text{gen}}$  (solid red line). Setup after the translation: layer 1 is centered in  $(0, 50 \mu\text{m})$ , layer 2 in  $(0, 100 \mu\text{m})$  (dashed black line) and the simulated track is reconstructed with curvature  $\kappa_{\text{reco}}$  (dashed red line).

to say that if the weak mode that originates the bias in the curvature of the muons has the same geometrical nature<sup>1</sup> as the one introduced in this simple simulation, then  $a_{1,3}$  and  $\Delta_k$  represent the same observable. Under this hypothesis it is possible to interpret the value of  $a_{1,3}$  in each sample in terms of a shift of the most external layer. In Figure 4.22 the value of  $\Delta_k$  in function of the shift of the external layer is shown. Here the estimated values of  $\Delta_k$  are obtained with muons with  $p_T = 40 \text{ GeV}$  but, since  $\Delta_k$  is strictly related to a geometrical deformation, in principle these values are independent from the  $p_T$  of the track. By comparing the values on the ordinate axis with those listed in Table 4.1 and Table 4.2 for  $a_{1,3}$  it is possible to extract the value of the shift for the layers of CMS that originates the weak mode in the aligned geometry. The layer with the radius  $r \approx 100 \text{ cm}$  is the fifth layer of the TOB, therefore the values of the shift found in Figure 4.22 should be similar to its shift in the aligned geometry. The shift that generates the weak mode is not only on the fifth layer of the TOB but

<sup>1</sup>Geometrical nature has to be intended in the following way: the weak mode in the aligned geometries is a shift in the same direction of some layers of the barrel and every layer is translated by a quantity proportional to its radius

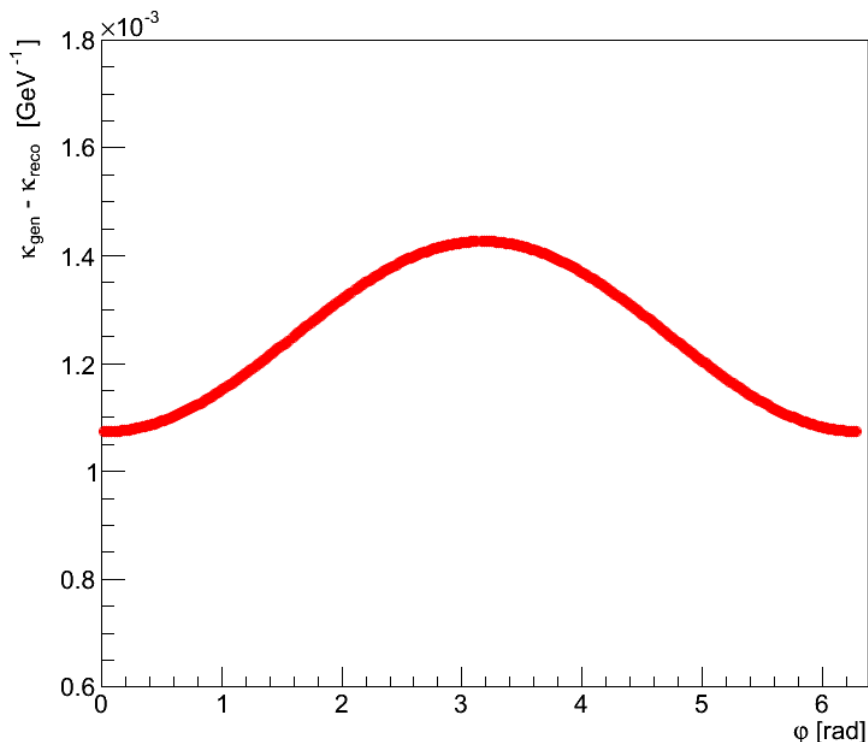


**Figure 4.21:** Difference between the generated and the reconstructed curvature as a function of the generated  $\varphi$  of the muon. Muons are generated with  $p_T = 40$  GeV. The shift on the outer layer ( $r=100$  cm) is  $100 \mu\text{m}$  in the  $\varphi = 0$  direction.

in every layer of the tracker<sup>ii</sup>, with a shift in every layer proportional to its radius. The resulting shifts for three layers in CMS are listed in Table 4.7. Due to the simplicity of the simulation built for this study the values has to be intended as indicative of the order of magnitude of the shift. It is important to notice that the resulting values of the shifts have the same order of magnitude of the uncertainties present in an aligned geometry affected by weak modes.

Every consideration made above applies to a muon with a negative curvature. The only difference with respect to a positive muon is that the sinusoidal plot in Figure 4.21 results with an opposite phase, but in presence of the same shifts on the layers the value of  $\Delta_k$  is the same as in the case of the muon with positive curvature.

A bias in the measurement of the mass of a reconstructed resonance, for

<sup>ii</sup>It represents a good approximation, because if a layer is not translated coherently with the others the alignment algorithm in order to minimize the  $\chi^2$  of the track correct its position until it is.

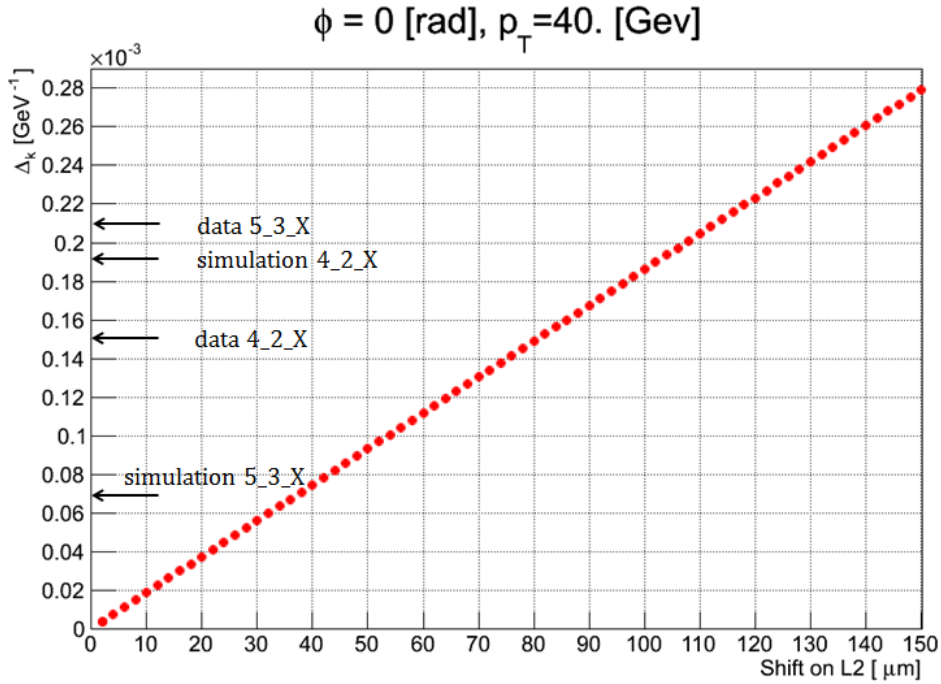


**Figure 4.22:** Values of  $\Delta_k$  as a function of the shift introduced on the external layer (L2). The shift is introduced also in the internal layer proportionally to its radius.

example  $Z$ , is directly related to the bias in the measurement of the curvature of the muons introduced by the deformations of the geometry. However there is an important additional detail, the bias on  $M_Z$  is strictly dependent on the topology of the event too, and in a sample of dimuons there are millions of events with different topologies. Therefore the modulations observed in the reconstructed  $M_Z$  in function of  $\varphi_-$  or  $\varphi_+$  (see for example Figures 4.1d and 4.1c) are related both to geometrical deformations of the aligned-geometry and to the topologies of the events in the considered sample.

---

<b>Indicative values of the shift on layers of the weak mode in the barrel</b>			
Sample	BPIX L3 shift [ $\mu\text{m}$ ]	TIB L4 [ $\mu\text{m}$ ]	TOB L6 [ $\mu\text{m}$ ]
data 4_2_X	10	40	80
simulation 4_2_X	10	50	100
data 5_3_X	10	60	110
simulation 5_3_X	$\approx 0$	15	30

---

**Table 4.7:** Shift on layers of CMS present in the aligned geometry extrapolated from the simple model described in the test.

## 4.5 Resolution on the curvature of the muons

A feature of the MuSclFit algorithm is that it provides an estimation of the resolution on the curvature of the muons. Moreover, thanks to the fit strategy used for the calibration process, two sets of parameters of the resolution are available, before and after the correction. A comparison between the resolution estimated by MuSclFit and the true resolution on the curvature can be performed for the samples of simulated muons. In this analysis the resolution of the detector is parameterized with a gaussian function. In order to extract the true resolution on the curvature of the tracks from a sample of simulated muons it is possible to plot the variable  $(\kappa_{reco} - \kappa_{gen})/\kappa_{gen}$  in bins of the relevant kinematic variable and perform a gaussian fit on its distribution. The standard deviation resulting from the fit represents the true resolution of the detector on the curvature of the muons<sup>iii</sup>. By referring to Equation 3.12 and to the parameters listed in Table 4.3 it is possible to compare the resolution estimated by MuSclFit before and after the correction with the true resolution of the detector. This is shown for the sample of simulated muons in 5\_3\_X in Figure 4.23. Here

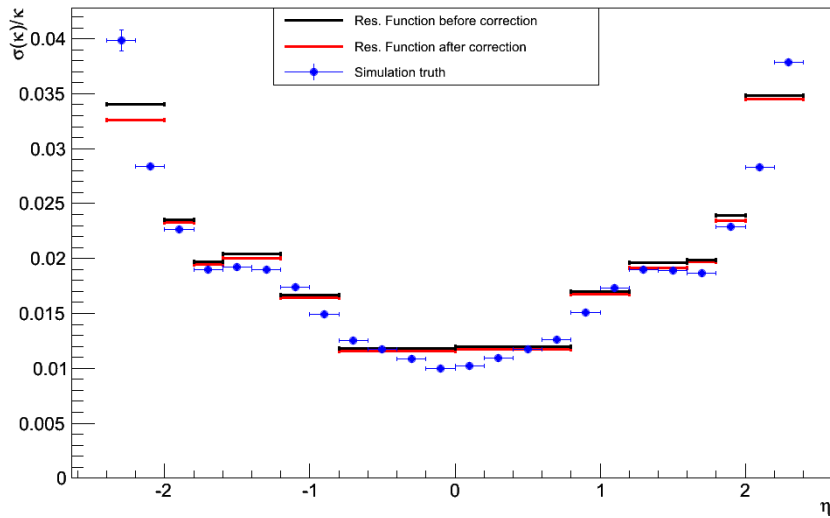


**Figure 4.23:** Comparison among the true resolution of the detector (blue dots), the resolution estimated before the correction (black line) and the resolution estimated after the correction (red line) for a sample of simulated muons at  $\sqrt{s} = 8$  TeV.

in some bins, for example in  $1.2 < |\eta| < 1.6$ , the fitted resolution before the correction appear slightly higher than the true resolution. The situa-

<sup>iii</sup>Actually is the relative resolution on the curvature i.e.  $\sigma(\kappa)/\kappa$ .

tion improves considering the resolution after the correction.



## 4.6 Detailed validation of the corrections

In this section the correction on the curvature is applied to the muons from the decay of three different resonances and an analysis on the effects of the correction for each resonance is performed in kinematical bins of the muons. The samples used are data and simulation at  $\sqrt{s} = 8$  TeV processed and the correction parameters have been calculated by performing the calibration on the  $Z$  resonance. The chosen resonances are  $J/\Psi$ ,  $Y(1S)$  and  $Z$ . A brief description of their properties is presented in Table 4.8 and Table 4.9.

$J/\Psi$	
Mass	$3096.916 \pm 0.011$ MeV
Width	$92.9 \pm 2.8$ KeV
$BR(\mu^+\mu^-)$	$5.93 \pm 0.06\%$

**Table 4.8:** Properties of  $J/\Psi$  from the Particle Data Group [3].

$Y(1S)$	
Mass	$9460.30 \pm 0.26$ MeV
Width	$54.02 \pm 1.25$ KeV
$BR(\mu^+\mu^-)$	$2.48 \pm 0.05\%$

**Table 4.9:** Properties of  $Y(1S)$  from the Particle Data Group [3]

In order to enhance the signal we impose kinematic cuts on the muons from the  $Y(1S)$  and  $J/\Psi$  decay. In both samples the cut on pseudorapidity of the muons is  $|\eta| < 2.4$ , and the cut on transverse momentum is  $p_T > 5$  GeV.

In what follows it is necessary to reconstruct  $J/\Psi$ ,  $Y(1S)$  and  $Z$  in different kinematical bins of the muons before and after the correction. A fitting strategy for the reconstruction of  $Z$  has already been defined in Chapter 2. The same fit strategy does not apply in the case of  $Y(1S)$  and  $J/\Psi$  because they are very narrow resonances. With a decay width of tens KeV a reasonable parametrization of the resonance is a Dirac delta function. On the other hand the reconstruction of these resonances is affected by the finite resolution of the detector, parametrizable with a gaussian function. For the  $J/\Psi$  the chosen fit strategy is to parametrize the distribution of the dimuon invariant mass in the region  $[2.9, 3.3]$  GeV both in the data and simulation samples with a Crystal Ball function added on a background

parametrized with a polynomial of degree 4. For the  $Y$  the simulated samples contain separately the  $Y(1S)$ ,  $Y(2S)$  and  $Y(3S)$ . For this reason the fit is performed in a limited invariant mass window [8.8, 9.8] GeV with a Crystal Ball function added to a polynomial of degree 4. Differently from the simulation the sample in data in the  $Y$  invariant mass region contains all the three resonances:  $Y(1S)$ ,  $Y(2S)$  and  $Y(3S)$ . The goal of the fit is to find the characteristics of  $Y(1S)$  in every kinematical bin. In order to properly take into account the contribution of the background, the fit is performed in an invariant mass region that contains all the three resonances: [8.7, 11.0] GeV. For this region the choice is to fit with three Crystal Ball functions added on a polynomial of degree 4. Examples of the fit in the  $J/\Psi$  and  $Y$  region of the dimuon invariant mass in the data sample are represented respectively in Figure 4.24a and Figure 4.24b. The figures refer both to a specific kinematical bin in which the positive muon has cuts both on his  $p_T$  and  $\eta$ , the same fitting strategy is applied in every kinematical bin considered. Here  $b_0, b_1, b_2, b_3$  and  $b_4$  denote the coefficients of the polynomial function of grade 4 that parametrizes the background; *mean*, *sigma*, *n* and *alpha* are the parameters of the Crystal Ball function and  $f_{sig}$  is the fraction of the signal with respect to the background. Since in Figure 4.24b the signals are three, they are represented by three Crystal Ball functions, here  $f_{CB1}$  and  $f_{CB2}$  represent respectively the the fraction of the events in the signal of  $Y(2S)$  and  $Y(3S)$  with respect to the events in the signal of  $Y(1S)$ .

The analysis is performed in bins of  $\eta$  and  $p_T$  for the positive muon and the notation used will be:

$$\begin{aligned}\Delta M &= \frac{M_{data} - M_{sim}}{M_{data}} \\ \Delta M_{data} &= \frac{M_{data} - m_0}{m_0} \\ \Delta M_{sim} &= \frac{M_{data} - m_0}{m_0}\end{aligned}$$

where  $M_{data}$  and  $M_{sim}$  represent respectively the fitted mass of the considered resonance in a data and in a simulation sample, and  $m_0$  is the nominal value of the resonance. Figures 4.25 and 4.26 show the improvement on the reconstruction of  $J/\Psi$ ,  $Y(1S)$  and  $Z$  after the correction on muons in kinematical bins of  $|\eta|$  and  $p_T$  of the positive muon. In every figure the left part represents the situation before the correction and the right part after the correction.

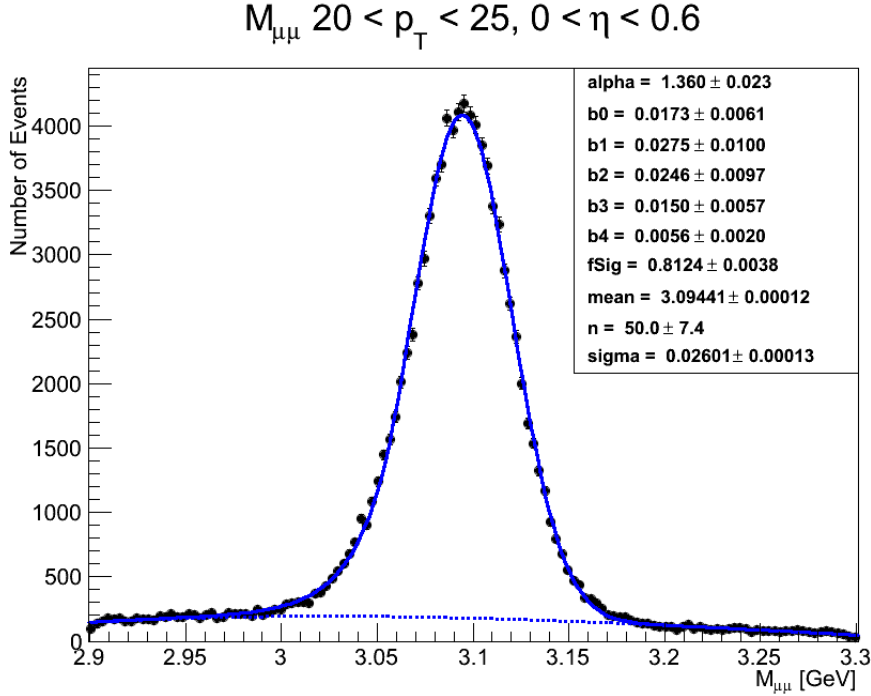
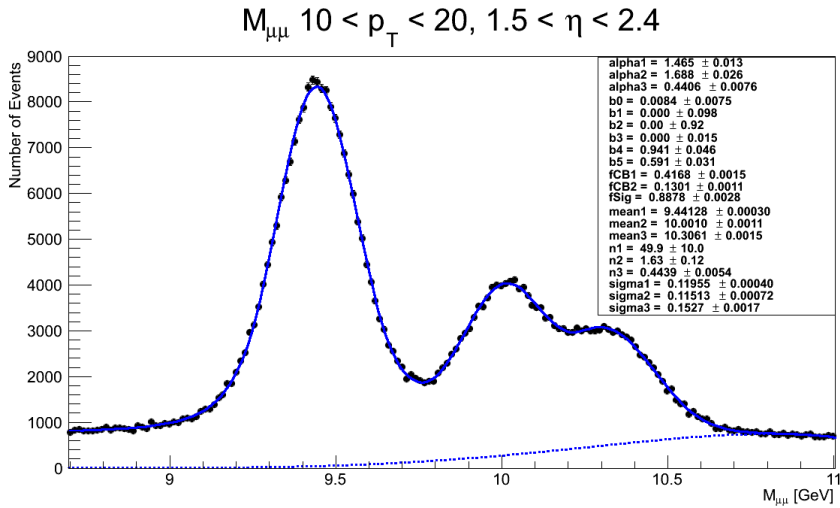
The improvement made by the correction is significant in most of the plots. Consider for example the Figures 4.25a and 4.25b, all the markers are shifted in the direction of  $\Delta M_{data}$ . On the other hand there are still cases in which the correction does not improve significantly the situation, as it is in Figures 4.25c and 4.25d, here the improvement is visible only

looking at the fit results that included all the muons in a sample. However in general, except for the values of  $Z$  when both muons have  $p_T > 45$  GeV and the positive muon have  $|\eta| > 2^{\text{iv}}$ ,  $\Delta M_{data}$  is about 2‰. To conclude in general the corrections found by a calibration that uses  $Z$  are beneficial, for every resonance considered, however there is still room for further improvements. Possible improvements that can be made to the calibration procedure are anticipated here but are not discussed in this thesis. They could be:

- modifications of the parametrization of the scale correction function, especially at higher values of  $|\eta|$ .
- different parametrization of the resolution function, for example the resolution could be parametrized with an higher number of bins in  $\eta$  of the muon.
- the use of parametrizations of the signal functions in different kinematic bins of the muons, see Appendix B.1.
- the use of more resonances together in the process of calibration, for example  $Y(1s)$  and  $Z$ , etc.

---

<sup>iv</sup>Here the fit is influenced by the limited number of events.

(a)  $M_{\mu\mu}$  in the interval  $[2.9, 3.3]$  GeV for a data sample at  $\sqrt{s} = 8$  TeV.(b)  $M_{\mu\mu}$  in the interval  $[8.7, 11.0]$  GeV for a data sample at  $\sqrt{s} = 8$  TeV.

**Figure 4.24:** Fit of the  $M_{\mu\mu}$  distribution in two regions, the solid blue line represents the fit of background plus signal, and the dotted blue line is the fit of the background contribution.

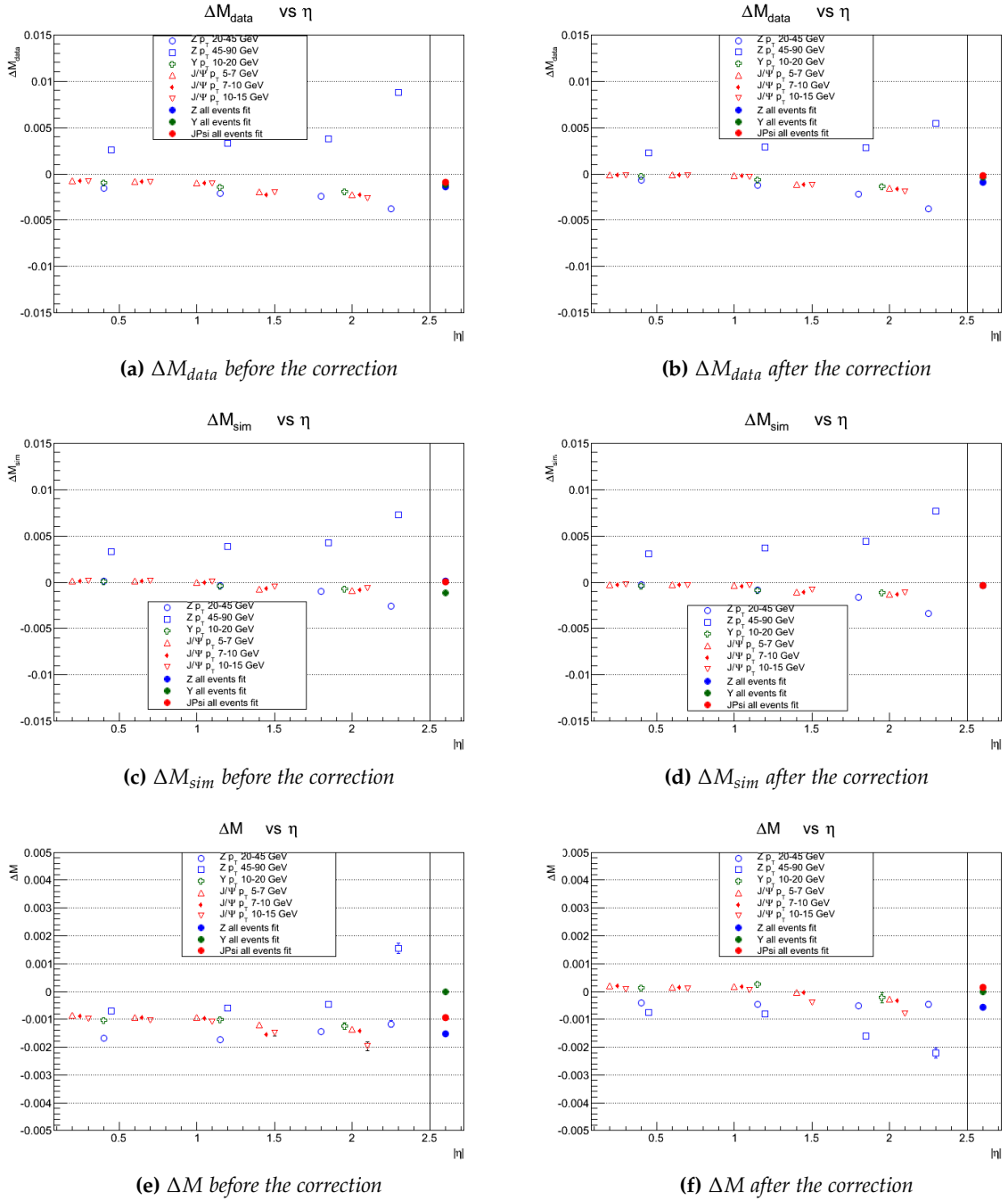


**Figure 4.25:** Comparison between the fitted value of the mass of  $J/\Psi$ ,  $\Upsilon(1S)$  and  $Z$  in data and simulation with its nominal value (Figures 4.25a, 4.25b, 4.25c, 4.25d) and comparison between data and simulation (Figures 4.25e, 4.25f). The kinematic intervals indicated in the legend refer to restrictions imposed on both muons. The markers of the  $J/\Psi$  resonance are three, their shapes are a red-filled triangle, and two empty triangles. The empty triangles are artificially translated along the x-axis in order to avoid visual superpositions, but their true value in x is the same of the red-filled triangle. The markers showed in the right part of the plot represent the results of fits performed without imposing kinematical cuts on the muons in every dataset.

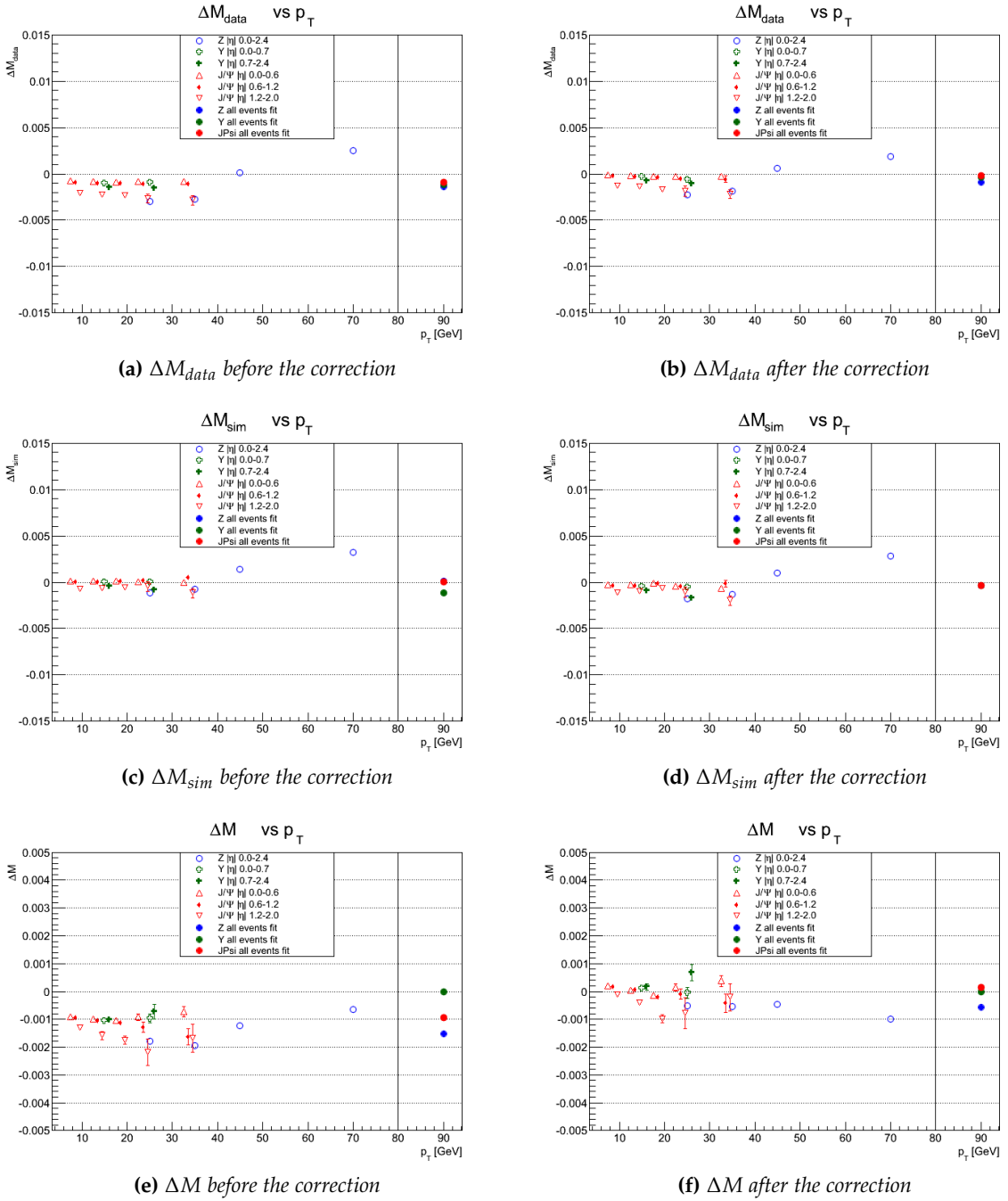


**Figure 4.26:** Comparison between the fitted value of the mass of  $J/\Psi$ ,  $\Upsilon(1S)$  and  $Z$  in data and simulation with its nominal value (Figures 4.26a, 4.26b, 4.26c, 4.26d) and comparison between data and simulation (Figures 4.26e, 4.26f). The kinematic intervals indicated in the legend refer to restrictions imposed on both muons. The consideration made in the caption of Figure 4.25 for the markers of the  $J/\Psi$  apply here too.

# Conclusions

The presence of weak modes in the aligned geometry of the Tracker leads to an incorrect determination of the momentum of the muons. Consequently muon decaying resonances are reconstructed with incorrect properties. The mass of the  $Z$  boson has been reconstructed starting from muons measured in an aligned geometry of the Tracker, and biases in the measured value of  $M_Z$  with respect to the nominal value have been found considering several kinematic intervals of the muons. This thesis has been devoted to the calibration of the momentum scale of the muons in the Tracker, in order to restore the bias present in the measurement of the mass of the  $Z$ . The calibration has been performed with the use of the MuSclFit algorithm, an algorithm developed within the Torino and Padova CMS groups in 2010. Muons with corrected momentum led to an improvement in the response of the Tracker to the reconstruction of  $Z$  in every kinematic interval of the muons considered. As well as the matching between the measured  $M_Z$  after the calibration and the nominal value of the mass  $m_0$  is significantly improved, also the matching between the reconstructed mass and resolution on  $Z$  in data and simulation samples processed in the same CMSSW release is enhanced. Moreover an estimation on the resolution on the momentum of the muons is provided before and after the correction. The result is that the MuSclFit correction improves also this observable. The calibration on the momentum scale of the muons has been performed for several samples in two CMSSW releases, both with simulated and real dimuons. The improvements on the reconstruction of  $Z$  have been observed for every sample considered.

# Appendix A

## Fit strategy

With the fit strategy described in Section 3.4 two sets of parameters for the scale corrections are given by the fit. With the goal of providing just one set of parameters, so that the final user can apply the correction on the muons once, the two sets of parameters are merged. Thanks to the trigonometric properties of Equation 3.9, and that  $p_0$  is fitted only once, it is possible to merge the corrections computed in two different iterations without changing its functional form. Let's denote with  $\kappa'$  the curvature corrected by the set of parameter found in the first fit of the scale function (here  $p_0$  is fixed to  $p_0 = 0$ ), according to Equation 3.9:

$$\kappa' = \left( \kappa - C_j'(\eta, \varphi) - \frac{\delta'}{2} \right)$$

and the curvature after the second scale function fit and the fit of  $p_0$  is  $\kappa''$  with:

$$\kappa'' = (1 + p_0) \left( \kappa' - C_j''(\eta, \varphi) - \frac{\delta''}{2} \right)$$

where the double-primed parameters refer to those fitted by the second fit of the scale function. In order to apply the correction of both fits on the initial curvature  $\kappa$  of the muon it is possible to write:

$$\kappa'' = (1 + p_0) \left( \kappa - \left( C_j''(\eta, \varphi) + C_j'(\eta, \varphi) \right) - \left( \frac{\delta''}{2} + \frac{\delta'}{2} \right) \right)$$

here the term  $(C_j''(\eta, \varphi) + C_j'(\eta, \varphi))$  have the same functional form. To improve this consider the Barrel term of  $C_j$  and  $C_j'$ :

$$\begin{aligned} C_3(\eta, \varphi) &= a_{1,3} \sin(\varphi + \varphi_{1,3}) + b_3(\eta - \eta_{0,3}) + b_{0,3} \\ C_3'(\eta, \varphi) &= a'_{1,3} \sin(\varphi' + \varphi'_{1,3}) + b'_3(\eta - \eta_{0,3}) + b'_{0,3} \end{aligned}$$



The trigonometric relation  $\sin(x + y) = \sin(x) \cos(y) + \sin(y) \cos(x)$  leads to:

$$C'_j(\eta, \varphi) + C_j(\eta, \varphi) = A_{1,3} \sin(\varphi + \Phi_{1,3}) + B_3(\eta - \eta_{0,3}) + B_{0,3}$$

where:

$$\begin{aligned} \Phi_{1,3} &= \text{Arctg} \left( \frac{a_{1,3} \sin(\varphi_{1,3}) + a'_{1,3} \sin(\varphi'_{1,3})}{a_{1,3} \cos(\varphi_{1,3}) + a'_{1,3} \cos(\varphi'_{1,3})} \right) \\ A_{1,3} &= \frac{a_{1,3} \cos(\varphi_{1,3}) + a'_{1,3} \cos(\varphi'_{1,3})}{\cos(\Phi_{1,3})} \\ B_3 &= b_3 + b'_3 \\ B_{0,3} &= b_{0,3} + b'_{0,3} \end{aligned}$$

Similar considerations apply to every  $\eta$ -bin of  $C_j$ . The output of MuSleFit is then a set of 47 parameters, 34 that hold the parameterization of the scale and the resolution after the scale correction, and 13 that represent the resolution before the scale correction.







## Appendix B

# Additional lineshapes

### B.1 Building of the signal function of $Z$ in kinematic intervals of the muons

The signal function introduced in Chapter 3 represents the theoretical distribution of the dimuon invariant mass  $m$  in the proximity of the mass of  $Z$  as it is predicted by the Standard Model. However the use of only one lineshape in MuSclFit represents an approximation as  $\sigma(m, m_0)$  was used for every muon with  $|\eta| < 2.4$  while the lineshape could be different in different kinematical regions of the muons. The goal of this section is to show a method to provide a parametrization of the theoretical lineshape of  $Z$  in various kinematic intervals for the muons. Since a theoretical calculation in different kinematic bins for the muons is not available, the strategy adopted here is to use simulated muons. Simulated muons are generated according to a distribution calculated within the Standard Model (see Reference [8]) that takes into account the partons interactions in the hard scattering process, and then are eventually propagated into the detector and reconstructed as tracks. In a simulation both the true parameters and the reconstructed parameters of the track of a muon are known. In order to find a parametrization for the dimuon invariant mass in different kinematical bins of the muons, it is possible to use the information on the true parameters of the particle which are not affected by reconstruction effects stored in the simulation sample. The sample used is the sample of simulated muons at  $\sqrt{s} = 7$  TeV and its characteristics are shown in Table 3.1. A comparison between the parametrizations of the dimuon invariant mass distribution at  $\sqrt{s} = 7$  TeV and  $\sqrt{s} = 8$  TeV calculated within the Standard Model has been performed in Chapter 3. No substantial difference was found between the two curves.

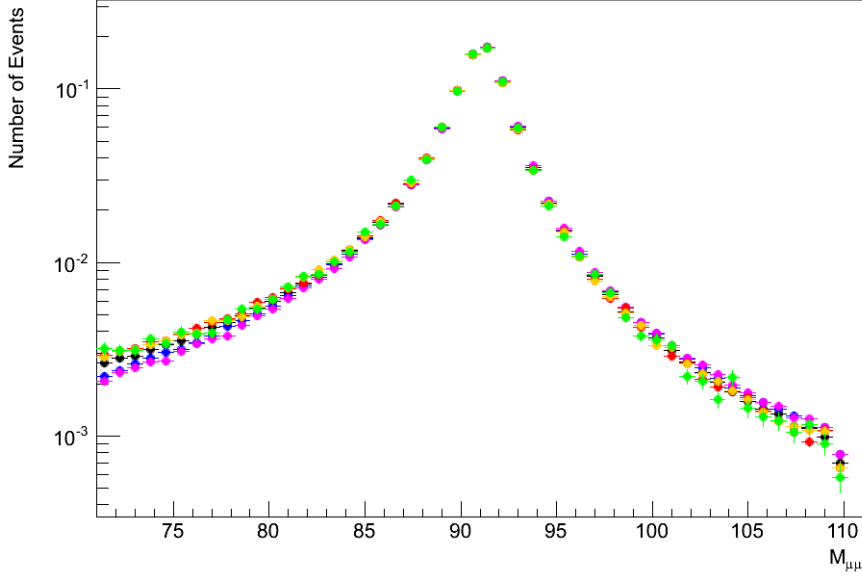
The kinematic bins in which the lineshape of  $Z$  will be reconstructed are listed in Table B.1. By using these kinematic bins for the muons it is possible to reconstruct the invariant mass distributions in the region  $[71, 111]$

<b>Kinematic regions of muons</b>	
$ \eta $ boundaries of $\mu_-$ and $\mu_+$	Color
$ \eta_-  \in [0, 1.5],  \eta_+  \in [0, 1.5]$	
$ \eta_-  \in [1.5, 2.1],  \eta_+  \in [0, 1.5]$ or $ \eta_-  \in [0, 1.5],  \eta_+  \in [1.5, 2.1]$	
$ \eta_-  \in [2.1, 2.4],  \eta_+  \in [0, 1.5]$ or $ \eta_-  \in [0, 1.5],  \eta_+  \in [2.1, 2.4]$	
$ \eta_-  \in [1.5, 2.1],  \eta_+  \in [1.5, 2.1]$	
$ \eta_-  \in [1.5, 2.1],  \eta_+  \in [2.1, 2.4]$ or $ \eta_-  \in [2.1, 2.4],  \eta_+  \in [1.5, 2.1]$	
$ \eta_-  \in [2.1, 2.4],  \eta_+  \in [2.1, 2.4]$	







**Table B.1:** Kinematical bins chosen for the muons and color convention used in this section.

GeV, see Figure B.1. Here each histogram has been normalized to unity in the interval  $[71, 111]$  GeV. The poissonian error of each bin has been properly rescaled after the normalization. Some differences among the distributions are present, especially far from the peak. In principle these distributions could be used instead of a single curve for every kinematical bin of the muons. However they suffer, especially in the tail of the distributions, from the limited statistics of the sample. In order to produce similar curves without statistical fluctuations it is possible to start from the curve  $\sigma(m, m_0)$  used in MuSclFit, and correct it according to the relation between each distribution in a kinematic region of the muons and the distribution of invariant mass obtained without imposing kinematic restrictions on the muons, i.e. both muons taken in the interval  $|\eta| < 2.4$ . The correction can be computed from a fit to the ratio of the distribution with and without the kinematic cuts, see Figure B.2. The ratio is performed for each distribution, the color convention defined in Table B.1 is respected here. The color of the ratio plot is the same of the distribution with certain restriction on the kinematic of the muons which is divided by the distribution in which the kinematic restrictions on the muons are not imposed. In order to extract a correction to apply to  $\sigma(m, m_0)$  it is possible to fit the ratios between the curves with a first order polynomial:  $a_0 + a_1 \cdot m$ . In Table B.2 are listed the fit results. Then for each kinematic restriction on muons considered, the parameters of the polynomial are used to rescale each bin of the lineshape  $\sigma(m, m_0)$ . Finally six curves are produced:  $\sigma(m, m_0)_i$  for  $i = 1, 2, 3, 4, 5, 6$ . They are shown in Figure B.3.

Preliminary results using these lineshapes indicate that no substantial improvement with respect to the base line choice, i.e. one lineshape for all the events, are found.



**Figure B.1:** Comparison among lineshapes in different kinematic regions of the muons.(From MC POWHEG).

Results of the fits at the ratios shown in Figure B.2		
Color associated to the dividend curve	$a_0$	$a_1$ [GeV <sup>1</sup> ]
	$1.18 \pm 0.01$	$-0.0020 \pm 0.0002$
	$0.67 \pm 0.02$	$0.0037 \pm 0.0002$
	$0.38 \pm 0.03$	$0.0069 \pm 0.0003$
	$1.52 \pm 0.04$	$-0.0058 \pm 0.0004$
	$1.49 \pm 0.02$	$-0.0054 \pm 0.0005$
	$1.53 \pm 0.08$	$-0.0061 \pm 0.0009$

**Table B.2:** Results of the fit at the ratio of the distribution with and without the kinematic cuts.

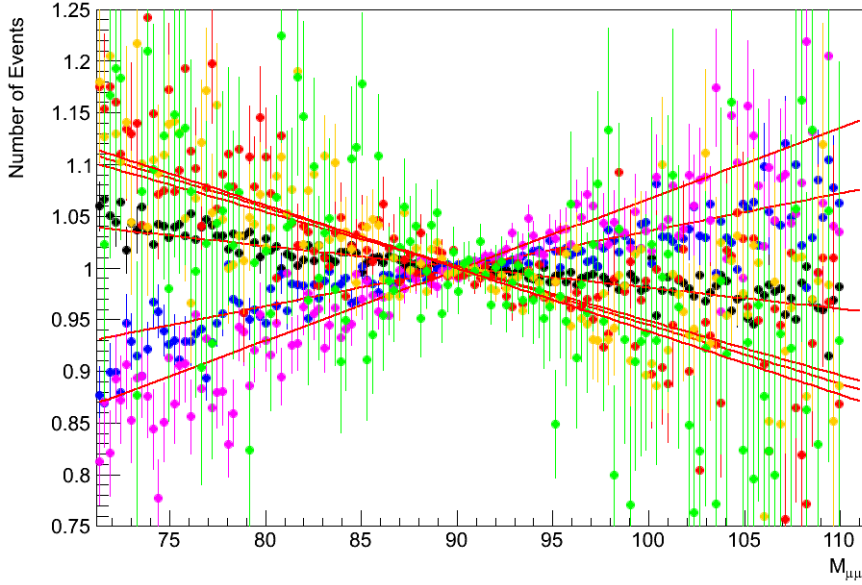


**Figure B.2:** Ratios between distributions in different kinematic regions of the muons, the errors are properly propagated here from the normalized histograms.(From MC POWHEG).

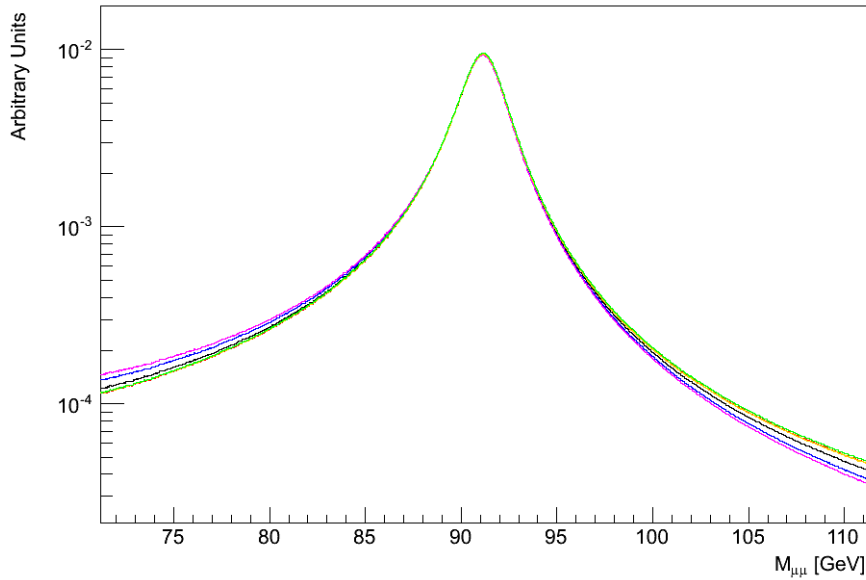


**Figure B.3:** Lineshapes in six kinematic bins of the muons produced starting from  $\sigma(m, m_0)$ . (Dittmaier + POWHEG)

## B.2 Building of the signal function for $J/\Psi$ and $Y(1S)$

One of the main characteristics of  $J/\Psi$  and  $Y(1S)$  is that they are very narrow resonances with respect to a GeV scale. Their widths are few tens of KeV and then in this analysis they were represented with Dirac delta functions. However, on the distribution of the invariant mass of the dimuon of those resonances there is a QED effect that influences the shape of the distribution up to the scale of GeVs: the final state emission of radiation (QED FSR) of the muons. This effect, in a typical distribution of invariant mass of the dimuons in proximity of the peak of a resonance, manifests itself as an enhancement of the number of dimuon events with invariant mass lower than the invariant mass of the peak. The purpose of this section is to show a method to create a model of signal function for  $J/\Psi$  and  $Y(1S)$  that takes into account the QED FSR of the muons. The strategy used here is to set up a simulation with the software PYTHIA that generates  $J/\Psi$  or  $Y(1S)$ , and make them decay into dimuons by taking into account the effect of the QED FSR on the momentum of the muons. The effect of the final state radiation is to reduce the momentum of the muons. However, in order to prevent the computation of divergent integrals, the software PYTHIA puts an infrared cut on the momentum of the emitted photon. By plotting in an histogram the invariant mass of the dimuon in proximity of the peak of the considered resonance it is possible to see the effect of this infrared cut: in the left tail of the distribution few bins do not have entries, they are the bins near the peak of the resonance. In order to create the models for the signal functions these bins have to be filled with the proper bin contents. To achieve this task, a fit on the left tail of the distribution is performed and the empty bins are then filled with the value of the fitted function in each bin. If with  $m$  is denoted the invariant mass of the dimuon, and with  $M$  the nominal value of the peak of the considered resonance, the function used for the fit is:

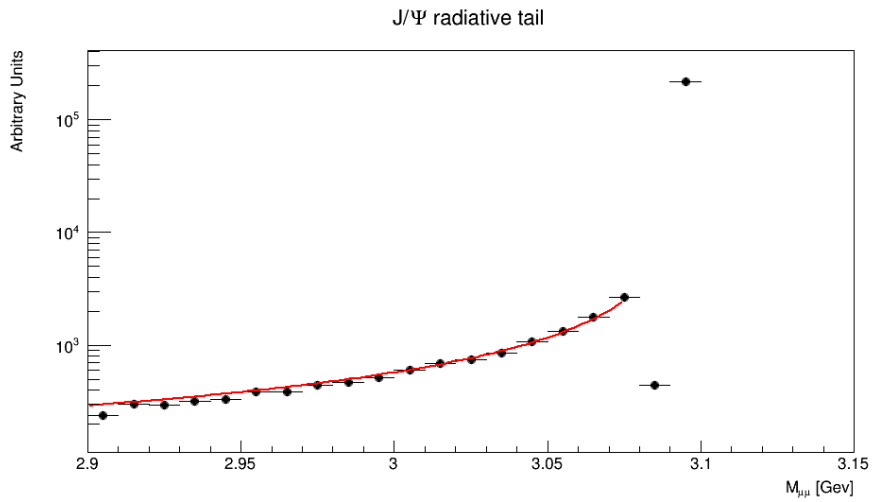
$$f(m) \propto \frac{1}{(M - m) \left[ 1 - \beta \cdot \left( \frac{M}{M - m} \right) \left( 1 - \frac{m^2}{M^2} \right) \right]} \quad (\text{B.1})$$

where

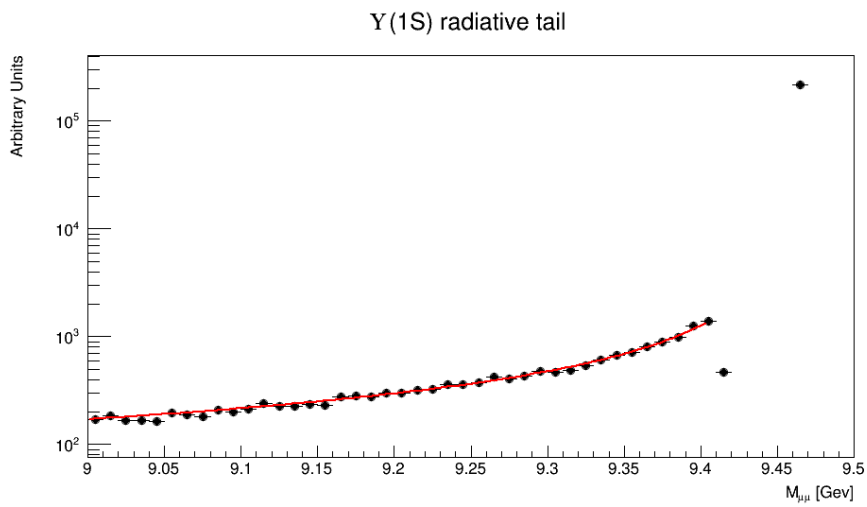
$$\beta = \sqrt{1 - \frac{4 m^2 M^2}{(m^2 + M^2)^2}} \quad (\text{B.2})$$

The fit is performed both for the distribution of invariant mass of the dimuon in proximity of the  $J/\Psi$  and  $Y(1S)$  peak values. For the tail of  $J/\Psi$  the fit is performed in the interval of the dimuon invariant mass  $[2.9, 3.075]$ , and for the tail of  $Y(1S)$  is chosen  $[9.0, 9.405]$ . Figure B.4 shows the situation for both resonances. Here the errors are poissonian and are smaller than the marker. In order to assign a value to the empty bins, the fitting function can be propagated until the peak value of the resonance.

However, given the fact that the histograms in output from PYTHIA have quite wide bins, it is convenient to create new histograms with the desired number of bins that follow the trend of the fitting function. In order to be coherent with the number of bins used for the signal function of the  $Z$  also here the number of bin chosen is 1001, both for  $J/\Psi$  and  $Y(1S)$ . The reason for building signal functions for  $J/\Psi$  and  $Y(1S)$  is that they can be used in MuSclFit to perform a calibration on the momentum of the muons, as well as it is done in this thesis. As explained in Chapter 3 the input for MuSclFit is a set of tabulated values of the convolution between the signal function and a gaussian function. The effect of this convolution is to modify the shape of the signal, it lowers the number of the events at the peak and raises the numer of the events in the tails of the distribution. The number of events at  $m > M$  is raised as well as the numer of events at  $m < M$ . For this reason the best choice for the boundaries of the histogram of a signal function is to put them at the same distance from the peak value. Hence the choice for the histogram of the signal function of  $J/\Psi$  is the following: 1001 bins of width 0.6 MeV ranging from  $m = 2.8$  GeV to  $m = 3.4006$  GeV. For  $Y(1S)$  the choice is 1001 bins of width 2.5 MeV ranging from  $m = 8.7$  GeV to  $m = 11.2025$  GeV. Figure B.5 shows the final results of the construction of the signal function for  $J/\Psi$  and  $Y(1S)$ . It is important to notice that these considerations could be applied to any narrow resonance decaying into two muons, such as  $\Psi'$ ,  $Y(2S)$ ,  $Y(3S)$  etc.



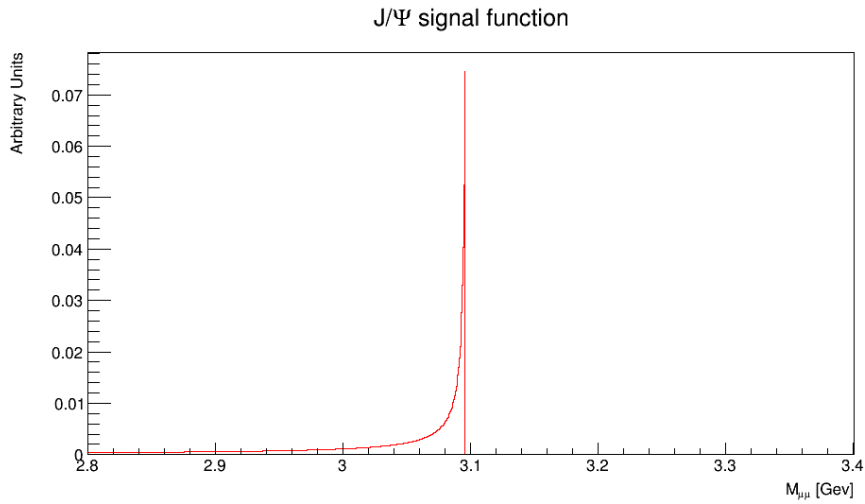
(a) Fit on radiative tail of J/ $\Psi$ .



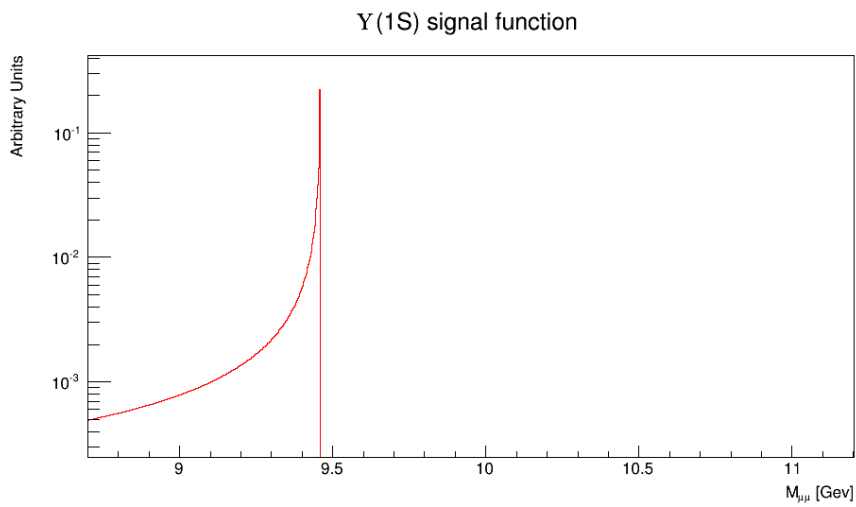
(b) Fit on radiative tail of  $\Upsilon(1S)$ .

**Figure B.4:** Fit on the radiative tail of the distribution of invariant mass of the dimuon in proximity of the J/ $\Psi$  and the  $\Upsilon(1S)$  peak value. The dimuons are generated by the PYTHIA software.





**(a)** Signal function for  $J/\Psi$ .



**(b)** Signal function for  $\Upsilon(1S)$ .

**Figure B.5:** Histograms of the signal functions for  $J/\Psi$  and  $\Upsilon(1S)$  that serve as inputs for *MuSclFit*.

# Bibliography

- [1] The CMS Collaboration, *CMS Detector performance and Software*, Physics Technical Design Report vol. 1, CERN/LHCC (2006), CMS TDR 8.1.
- [2] G. Flucke, P. Schleper, G. Steinbrücka and M. Stoyeb, *CMS silicon tracker alignment strategy with the Millepede II algorithm*, JINST, vol. 3, p. P09002, (2008).
- [3] J. Beringer et al. (Particle Data Group), *The Review of Particle Physics*, Phys. Rev. D86, 010001 (2012).
- [4] S. Dittmaier, M. Huber, *Radiative corrections to the neutral-current Drell–Yan process in the Standard Model and its minimal supersymmetric extension*, Journal of High Energy Physics, vol. 1 (2010).
- [5] The CMS Collaboration, *Performance of CMS muon reconstruction in pp collision events at  $\sqrt{s} = 7$  TeV*, JINST, CERN-PH-EP/2012-173, CMS-MUO-10-004
- [6] S. Bolognesi, M.A. Borgia, R. Castello, C. Mariotti, M. De Mattia, T. Dorigo, *Calibration of track momentum using dimuon resonances in CMS*, CMS Analysis Note, 2010/059, CERN
- [7] V. I. Klyukhin et al., *Measurement of the CMS Magnetic Field*, IEEE Transactions on applied superconductivity, vol. 18, n. 2, june 2008
- [8] <http://powhegbox.mib.infn.it/>
- [9] The CMS Collaboration, *Precise Mapping of the Magnetic Field in the CMS Barrel Yoke using Cosmic Rays*, JINST, Vol. 5, Issue 03, pp. T03021 (2010).
- [10] Asish Satpathy, *Overview and status of the CMS silicon strip tracker*, Journal of Physics: Conf. Ser. 110 092026 (2008)
- [11] The CMS collaboration, *Measurements of inclusive W and Z cross sections in pp collisions at  $\sqrt{s} = 7$  TeV*, Journal of High Energy Physics, Volume 2011, article id. 80 (2011)

- 
- [12] R. Fruhwirth, M. Regler *On the quantitative modelling of core and tails of multiple scattering by Gaussian mixtures*, Nuclear Instruments and Methods in Physics Research A 456 369-389 (2001)
- [13] The CMS collaboration, *Prompt and non-prompt  $J/\Psi$  production in pp collisions at  $\sqrt{s} = 7$  TeV*, European Physical Journal C, Volume 71, article id. 1575 (2011)
- [14] R. Luchsinger, C. Grab, *Vertex reconstruction by means of the method of Kalman filter*, Computer Physics Communications 76 263-280 (1993)
- [15] S. Bolognesi, *Calibration of the CMS Magnetic Field using Cosmic Muon Tracks*, CERN, Conf.Proc. C0908171 445-447 (2009)
- [16] The CMS Collaboration, *Performance of muon identification in pp collisions at  $\sqrt{s} = 7$  TeV*, CERN, CMS PAS MUO-10-002, (2010)
- [17] The CMS Collaboration, *Measurement of Momentum Scale and Resolution using Low-mass Resonances and Cosmic Ray Muons*, CERN, CMS PAS TRK-10-004, (2010)
- [18] The CMS Collaboration, *Measurement of inclusive W and Z boson cross sections in pp collisions at  $\sqrt{s} = 8$  TeV*, CERN, CMS PAS SMP-12-011, (2012)
- [19] The OPAL Collaboration, *Measurement of the  $Z^0$  Mass and Width with the OPAL detector at LEP*, Phys. Lett. B231 530, (1989)
- [20] E. Fermi, *Trends to a theory of Beta radiation*, Nuovo Cimento, vol. 11, pp. 1-19, 1934.
- [21] S. Dawson, *Introduction to electroweak symmetry breaking*, 1998. hep-ph/9901280.
- [22] *LHC Design Report*, CERN 2004-003, (2004).
- [23] R. Adolphi et al., *The CMS experiment at the CERN LHC*, JINST, vol. 3, p. S08004, 2008.
- [24] The Geant4 Collaboration, *GEANT Detector Description and Simulation Tool*, <http://geant4.web.cern.ch/geant4/>.
- [25] G. Cowan, *Statistical Data Analysis*, Clarendon Press, Oxford, (1998).
- [26] V. Verkerke, D. Kirby, *RooFit Users Manual*, v2.07, CERN, (2006).
- [27] R. Brun, F. Rademakers, *ROOT User's Guide*, CERN, (2007).

# Acknowledgements

Desidero ringraziare in modo particolare:

Ernesto perchè durante tutto il percorso di tesi mi ha seguito costantemente, insegnandomi molto.

Stefano Casasso per l'aiuto essenziale che mi ha fornito nello svolgere questo lavoro di tesi, e anche per le chiacchierate all'infuori di MuSclFit.

Silvia per la sua disponibilità e il suo aiuto.

Luca, Marco M., Giulio, Linda, Alessandro, per le chiacchierate di fisica e non degli ultimi mesi.

Voglio anche ringraziare in modo speciale tutte quelle persone che mi hanno accompagnato non solo nel percorso universitario, ma anche nella vita.

Ringrazio mio Papà, che è riuscito a trasmettermi la sua genuina passione per la scienza, e mia Mamma, che mai per un attimo ha smesso di incoraggiarmi e sostenermi in qualsiasi decisione abbia preso nella vita; è a voi che dedico questo lavoro di tesi.

Ringrazio i miei due nonni giovani e i miei due nonni che non ci sono più, Alex, gli zii e cuginetti.

Ringrazio gli amici di Chiavazza e di Lessona, e anche Aldo, Mina e Como, per i cinque anni passati insieme a Torino.

Grazie a Marco, Feel, Vale e Andre, per essere stati una parte essenziale del mio percorso fin dai primi mesi di università.

Un grazie enorme lo devo anche a Claudia, perchè da quattro anni porta solo felicità nella mia vita.

*... they also build telescopes and satellites and accelerators, and sit at their desks for endless hours working out the meaning of the data they gather.*

*The effort to understand the universe is one of the very few things that lifts human life a little above the level of farce, and gives it some of the grace of tragedy.*

— **Steven Weinberg**, *The First Three Minutes*